Marine Dual Fuel Engines Modelling and Optimisation Employing A Novel Combustion Characterisation Method

By

La Xiang

A thesis presented in fulfilment of the requirement for the degree of

Doctor of Philosophy

University of Strathclyde

Department of Naval Architecture, Ocean and Marine Engineering

Glasgow, the UK

August 2021

Declaration of Authenticity and Author’s rights

This thesis is the result of the author's original research. It has been composed by the author and has not been previously submitted for examination which has led to the award of a degree.

The copyright of this thesis belongs to the author under the terms of the United Kingdom Copyright Acts as qualified by University of Strathclyde Regulation 3.50. Due acknowledgement must always be made of the use of any material contained in, or derived from, this thesis.

Signed:

Review committee:

Date:

Abstract

Dual fuel (DF) engines have been an attractive alternative of traditional diesel engines for reducing both the environmental impact and operating cost. The major challenge of DF engine design is to deal with the performance-emissions trade-off via operating settings optimisation. Nevertheless, determining the optimal solution requires large amount of case studies, which could be both time-consuming and costly in cases where methods like engine test or Computational Fluid Dynamics (CFD) simulation are directly used to perform the optimisation.

This study aims at developing a novel combustion characterisation method for marine DF engines based on the combined use of three-dimensional (3D) simulation and zero-dimensional/one-dimensional (0D/1D) simulation methods. The 3D model is developed with the CONVERGE software and validated by employing the measured pressure and emissions. Subsequently, the validated 3D model is used to perform a parametric study to explore the engine operating settings that allow simultaneous reduction of the brake specific fuel consumption (BSFC) and NOx emissions at three engine operation conditions (1457 r/min, 1629 r/min and 1800 r/min). Furthermore, the derived heat release rate (HRR) is employed to calibrate the 0D Wiebe combustion model by using Response Surface Methodology (RSM). A linear response model for the Wiebe combustion function parameters is proposed by considering each Wiebe parameter as a function of the pilot injection timing, equivalence ratio and natural gas mass. The 0D/1D model is established in the GT-ISE software and used to optimise the performance-emissions trade-off of the reference engine by employing the Nondominated Sorting Genetic Algorithm II (NSGA II).

The obtained results provide a comprehensive insight on the impacts of the involved engine operating settings on in-cylinder combustion characteristics, engine performance and emissions of the investigated marine DF engine. By performing the settings optimisation at three engine operating points, settings that lead to reduced BSFC are identified, whilst the NOx emissions comply with the Tier III NOx emissions regulation. The proposed novel method is expected to support the combustion analysis and enhancement of marine DF engines during the design phase, whilst the derived optimal solution is expected to provide guidelines of DF engine management for reducing operating cost and environmental footprint.

Keywords: marine dual fuel engine; 3D simulation model; heat release rate; Wiebe combustion model; 0D/1D simulation model; operating settings optimisation; performance-emissions trade-off

Acknowledgement

Firstly, I would like to express my profound gratitude to my supervisor Prof Gerasimos Theotokatos for giving me the opportunity to conduct PhD research under his supervision and for his continuous support and guidance during my PhD period. His vast knowledge, motivation and patience are extremely important for the success of my PhD research.

Secondly, I would like to thank Prof Yu Ding from Harbin Engineering University, China, who has supervised me jointly with Prof Gerasimos Theotokatos and supported me to pursue my PhD study in the UK. His valuable feedback, comments and critical questions have helped clarify my research idea and guide me in the right direction.

Furthermore, thank my colleagues from the University of Strathclyde Maritime Research Safety Centre for their support to my research work. Thank all the friends I have met in the UK for making my life happy and colourful. Thank my flat mate for the comfortable living environment and delicious cooking.

Lastly, my deepest gratitude goes to my parents who have supported me through my life by constant concern. Thanks so much for their unconditional love and devotion.

Research output

L. Xiang, G. Theotokatos, H.N. Cui，K.D. Xu, H.K. Ben, Y. Ding. 2020. Parametric Knocking Performance Investigation of Spark Ignition Natural Gas Engines and Dual Fuel Engines; Journal of Marine Science and Engineering. 8(6), 459. https://doi.org/10.3390/jmse8060459

L. Xiang, G. Theotokatos, Y. Ding. 2019. Investigation on Gaseous Fuels Interchangeability with an Extended Zero-dimensional Engine Model; Energy conversion and management. 183 (1 March 2019), 500-514. https://doi.org/10.1016/j.enconman.2019.01.013

L. Xiang, E.Z. Song, Y. Ding. 2018. A Two-Zone Combustion Model for Knocking Prediction of Marine Natural Gas SI Engines; Energies. 11(3): 561. https://doi.org/10.3390/en11030561

Y. Ding, L. Xiang, H.N. Cui; 2018. Modelling of Thermodynamic Properties of Diesel Fuel and In-Cylinder Gas for Diesel Engine Combustion Investigation; Energy & Fuels. 32, 12, 12871–12883. https://doi.org/10.1021/acs.energyfuels.8b02570

Contents

Declaration of Authenticity and Author's rights I
Abstract III
Acknowledgement V
Research output VII
Contents IX
List of figures XIII
List of tables XVII
Abbreviations XIX
Nomenclature XXI
Chapter 1. Introduction 1
  1.1 Chapter Outline 1
  1.2 Background 1
    1.2.1 Marine emission regulations and solutions 1
    1.2.2 Liquified Natural Gas (LNG) Fuelled Engines 2
    1.2.3 Dual-fuel Engine Challenges 4
  1.3 Motivation of the present study 5
  1.4 Aim and Objectives 6
  1.5 Research framework 7
  1.6 Thesis layout 8
  1.7 Chapter summary 10
Chapter 2. Critical review 11
  2.1 Chapter Outline 11
  2.2 Engine optimisation 11
    2.2.1 Classification of optimisation algorithms 11
    2.2.2 Genetic algorithms 12
    2.2.3 Fitness evaluating functions for engine optimisation 13
  2.3 Engine modelling 14
    2.3.1 Physical engine models 14
    2.3.2 DF engine combustion characterisation 16
    2.3.3 Wiebe combustion model calibration 17
  2.4 Key findings and research gaps 18

2.5 Chapter summary 20
Chapter 3. Modelling Methodologies 21
3.1 Chapter outline 21
3.2 Research approach 21
3.3 Modelling methodology of 0D/1D simulation model 22
3.3.1 Calculation principles for modelling cylinders 23
3.3.2 Calculation principles for modelling other engine components 31
3.3.3 Calculation flowchart 37
3.4 Modelling methodology of 3D simulation model 39
3.4.1 Calculation principles 39
3.4.2 Calculation flowchart 44
3.5 Combustion model calibration 45
3.5.1 Heat release calculation 46
3.5.2 Wiebe combustion parameters determining and fitting 47
3.6 Multi objective optimisation 50
3.6.1 Multi objective optimisation and PARETO optimal solution 50
3.6.2 Nondominated sorting genetic algorithm-II 52
3.7 Chapter summary 53
Chapter 4. Experiment setup and case studies 55
4.1 Chapter outline 55
4.2 Engine characteristics and experiment setup 55
4.2.1 Engine characteristics 55
4.2.2 Experiment setup 58
4.3 Case studies 60
4.3.1 Parametric investigation using 3D simulation model 60
4.3.2 Wiebe combustion model calibration 63
4.3.3 Engine operating settings optimisation 64
4.4 Chapter summary 66
Chapter 5. Models setup and validation 67
5.1 Chapter outline 67
5.2 0D/1D Model setup and validation 67
5.2.1 Model layout and setup 67
5.2.2 Combustion model calibration based on measured in-cylinder pressure 69
5.2.3 Model validation 73

5.3 3D Model setup and validation 76

5.3.1 Model setup 76

5.3.2 Computation mesh study 78

5.3.3 Knocking detection 79

5.3.4 Model validation 81

5.4 Chapter summary 84

Chapter 6. Results and discussion 85

6.1 Chapter outline 85

6.2 Parametric investigation using the 3D model 85

6.2.1 Individual effect investigation at 100% operation load 85

6.2.2 Parametric investigation at different operation loads 96

6.3 Wiebe combustion model calibration 106

6.3.1 Wiebe combustion parameters determining 106

6.3.2 Wiebe combustion parameters fitting 108

6.4 Engine operating settings optimisation 114

6.4.1 Case studies analysis 114

6.4.2 Sensitivity study 116

6.5 Chapter summary 118

Chapter 7. Conclusions and recommendations 119

7.1 Chapter outline 119

7.2 Main findings and conclusions 119

7.3 Innovation 121

7.4 Contribution 122

7.5 Limitations and future research recommendations 123

7.6 Review of research objectives 124

7.7 Chapter summary 126

References 127

APPENDIX 137

APPENDIX A – Bilcan’s schematic algorithm 137

List of figures

Figure 1.1 Research framework and thesis layout 9

Figure 3.1 Research approach flow....21

Figure 3.2 Calculation flowchart of the turbocharger sub-model 35

Figure 3.3 Calculation flowchart of the in-cylinder two-zone 0D model 38

Figure 3.4 Calculation flowchart of the investigated 0D/1D simulation model....39

Figure 3.5 Calculation flowchart of the developed 3D simulation model in CONVERGE....45

Figure 3.6 Calculation flowchart of the heat release calculation for dual fuel engines 47

Figure 3.7 Calculation flowchart of NSGA II 53

Figure 4.1 YC6K DF engine testbed....55

Figure 4.2 The original maps of the employed compressor and turbine....56

Figure 4.3 Turbine mass flow validation by using the Griddata and Gridfit functions....57

Figure 4.4 The fitted turbocharger characteristic surface....57

Figure 4.5 Sensor layout of YC6K DF engine test bed....59

Figure 4.6 Optimisation flowchart 65

Figure 5.1 The 0D/1D model of the investigated DF engine developed with GT-ISE....67

Figure 5.2 HRR analysis at different operating conditions under propeller characteristics....69

Figure 5.3 Wiebe parameter variation with normalised load 72

Figure 5.4 Calculated HRR and fitted HRR surface under working conditions of propeller characteristics curve 73

Figure 5.5 In-cylinder pressure comparison at different operation loads....74

Figure 5.6 Simulation results and comparison with available experiment data 75

Figure 5.7 Computational domain of complete and one-eighth of the combustion chamber at TDC 76

Figure 5.8 In-cylinder pressure comparison with 4 base grid sizes 79

Figure 5.9 Location of the monitoring points 80

Figure 5.10 Pressure analysis at the baseline case 80

Figure 5.11 Simulated and measured in-cylinder pressure and heat release rate of the investigated engine at different operation loads: (a) 100%; (b) 74%; (c) 53%; (d) 32%..................81

Figure 5.12 Simulated and measured emissions of the investigated engine at different operation conditions 83

Figure 6.1 2D simulation result with different pilot injection timings...87

Figure 6.2 In-cylinder temperature distribution with different pilot injection timing.....................88

Figure 6.3 In-cylinder CH_2O distribution with different pilot injection timing 89

Figure 6.4 2D result with different equivalence ratio variations...91

Figure 6.5 In-cylinder temperature distribution with different equivalence ratio variations...........92

Figure 6.6 In-cylinder CH_2O distribution with different equivalence ratio variations....................92

Figure 6.7 2D result with different NG mass variations 94

Figure 6.8 In-cylinder temperature distribution with different NG mass variations 95

Figure 6.9 In-cylinder CH_2O distribution with different NG mass variations 95

Figure 6.10 NOx emissions versus BSFC with different operating settings at three operation conditions: 1800 r/min, 1629 r/min and 1457 r/min...97

Figure 6.11 Parametric study results showing potential for NOx emission and BSFC reduction at three operation conditions: 1800 r/min, 1629 r/min and 1457 r/min............................99

Figure 6.12 CA50 and combustion duration with different pilot injection timings 104

Figure 6.13 CA50 and combustion duration with different equivalence ratio variations 105

Figure 6.14 CA50 and combustion duration with different NG mass variations 106

Figure 6.15 HRR and pressure comparison by using Double Wiebe functions and Triple Wiebe functions at three operation conditions: 1800 r/min, 1629 r/min and 1457 r/min......108

Figure 6.16 Predicted vs. actual Wiebe parameters at 1800 r/min operation condition 110

Figure 6.17 HRR and pressure comparison by using the Linear response model and CFD simulation at three operation conditions: 1800 r/min, 1629 r/min and 1457 r/min......................113

Figure 6.18 Optimisation result at three operation conditions: 1800 r/min, 1629 r/min and 1457 r/min 114

Figure 6.19 BSFC and NOx emissions comparison between the optimal solution and baseline cases 116

Figure 6.20 Sensitivity analysis at three operation conditions: 1800 r/min, 1629 r/min and 1457 r/min 117

Figure A.1 Schematic algorithm for determining the Wiebe parameters 138

List of tables

Table 3.1 Modelling theories employed for developing the 0D/1D simulation model 23

Table 3.2 Employed mathematical models and chemical mechanisms in the 3D simulation model 40

Table 3.3 Wiebe parameters determining method of a Triple-Wiebe function...............................48

Table 4.1 Main characteristics of YC6K DF engine 56

Table 4.2 Employed sensors specifications...58

Table 4.3 Compositions of the employed natural gas 59

Table 4.4 Operating parameters under 6 working conditions of the propulsion characteristic curve 59

Table 4.5 Operating settings of the effect investigation..61

Table 4.6 Equivalence ratio variation settings for the effect investigation.....................................62

Table 4.7 Natural gas mass variation settings for the effect investigation 62

Table 4.8 Genetic algorithm settings...64

Table 4.9 Optimisation process parameters...66

Table 5.1 Input parameters of the developed 0D/1D simulation model...68

Table 5.2 Variation range of the Wiebe combustion parameters at 100% operation load 70

Table 5.3 Wiebe combustion parameters under working conditions of propeller characteristics curve 71

Table 5.4 Wiebe parameters correlations under working conditions of propeller characteristics curve 72

Table 5.5 Quantitative Comparison between the simulated and measured in-cylinder pressure 74

Table 5.6 Input parameters of the developed 3D simulation model..77

Table 5.7 Mesh control strategy 79

Table 5.8 Comparison between the simulated and the measured emissions. 83

Table 6.1 Level settings of parametric run at three operation conditions.......................................98

Table 6.2 Optimal points obtained from the parametric run at 1800 r/min operation condition ...100

Table 6.3 Optimal points obtained from the parametric run at 1629 r/min operation condition ...101

Table 6.4 Optimal points obtained from the parametric run at 1457 r/min operation condition ... 101

Table 6.5 Combustion characteristic of the parametric run at 1800 r/min ... 102

Table 6.6 Combustion characteristic of the parametric run at 1629 r/min ... 103

Table 6.7 Combustion characteristic of the parametric run at 1457 r/min ... 103

Table 6.8 Wiebe parameters fitted by using double Wiebe and triple Wiebe functions ... 107

Table 6.9 Relative errors between the predicted and measured p_{max} and IMEP ... 107

Table 6.10 Linear response model for Wiebe combustion parameters at 1800 r/min ... 109

Table 6.11 Quadratic response model for Wiebe combustion parameters at 1800 r/min ... 109

Table 6.12 Wiebe combustion parameters fitted by using linear response model at three operation conditions: 1800 r/min, 1629 r/min and 1457 r/min ... 111

Table 6.13 Relative errors between the predicted and measured values by using linear response model ... 112

Table 6.14 Optimisation results summary (case studies 1-3) ... 115

Table A.1 Five determining points in a HRR curve ... 139

Abbreviations

0D	Zero-dimensional
1D	One-dimensional
3D	Three-dimensional
ABS	Air bypass system
ACA	Ant colony algorithm
ANN	Artificial neural network
BSFC	Brake specific fuel consumption
BTE	Brake thermal efficiency
CFD	Computational Fluid Dynamics
CI	Compression ignition
CN	Cetane number
DF	Dual Fuel
DFT	Density functional theory
DOE	Design of experiment
ECA	Emission Control Areas
EEDI	Energy Efficiency Design Index
EGR	Exhaust gas recirculation
EGCS	Exhaust gas cleaning systems
EOC	End of combustion
GA	Genetic algorithm
GHG	Greenhouse Gas
HCA	Hill climbing algorithm
HRR	Heat release rate
ICE	Internal Combustion Engine
IMO	International Maritime Organization
IVC	Inlet valve close
LHV	Lower heating value

LNG	Liquified natural gas
LPG	Liquefied petroleum gas
LSFO	Low-sulfur fuel oil
MARPOL	The International Convention for the Prevention of Pollution from Ships
MEPC	Marine Environmental Protection Committee
MOGA	Multi-objective algorithm
NAGA-II	Non-dominated sorting genetic algorithm II
PM	Particulate matter
PSA	Particle swarm algorithms
RSM	Response surface methodology
SAG	Simulated annealing algorithm
SCR	Selective catalytic reduction
SEEMP	Ship Energy Efficiency Management Plan
SI	Spark ignition
SOC	Start of combustion
SVW	Support vector machine
TDC	Top dead centre
UHC	Unburnt hydrocarbon
VOC	Volatile Organic Compounds

Nomenclature

$AFR_{NG,0}$	Stoichiometric air-fuel ratio of natural gas	-
$AFR_{d,0}$	Stoichiometric air-fuel ratio of diesel	-
A_{wall}	Heat transfer surface area	m^2
$A_{v,ex}$	Flowing area of exhaust valve	m^2
$A_{v,s}$	Flowing area of inlet valve	m^2
a	Combustion efficiency coefficient in Wiebe function	-
a_k	Fitting coefficient of specific heat at constant pressure	-
$BSFC$	Brake specific fuel consumption	g/kW/h
b_i	Weight factor of each Wiebe function	-
C_1	Airflow velocity coefficient in Woschni heat transfer formula	-
C_2	Combustion chamber coefficient in Woschni heat transfer formula	-
C_f	Coefficient for correcting the polytropic index	-
CH_4	Methane	-
C_2H_6	Ethane	-
C_3H_8	Propane	-
CO	Carbon oxide	-
CO_2	Carbon dioxide	-
C_r	Compression ratio	-
c_m	Average piston speed	m/s
c_p	Specific heat at constant pressure	J/kg/K
c_v	Specific heat at constant volume	J/kg/K
D	Cylinder bore	m
E	Activation energy for ignition	J
EOC	End of combustion in Wiebe function	°CA
$\dot{E}_f$	Energy absorption rate caused by pilot diesel	J/°CA

	evaporation	
HC	Hydrocarbon	-
h	Specific enthalpy	J/kg
$IMEP$	Indicated mean effective pressure	bar
I_{TC}	Turbocharger rotational inertia	kg·m^2
Kp	Proportionality constant in PI control	-
K_I	Integral constant in PI control	-
k	Adiabatic exponent	-
k_C	Adiabatic exponent of the compressor inlet gas	-
k_T	Adiabatic exponent of the turbine inlet gas	-
k_b	Backward reaction rate coefficient in Zeldovich Mechanism	cm^3/mol/s
k_f	Forward reaction rate coefficient in Zeldovich Mechanism	cm^3/mol/s
M	Molecular mass	g/mol
M_e	Engine torque	N·m
$m_{NG,0}$	Initial natural gas injection mass per cycle	kg/cyc
$m_{NG,100}$	Natural gas injection mass per cycle at 100% operating load	kg/cyc
m_1	Burnt zone mass	kg
m_2	Unburnt zone mass	kg
m_{flx}	Mass flow at grid boundary	kg/s
m_v	Shape factor in Wiebe function	-
$\dot{m}_C$	Compressor mass flow	kg/s
$\dot{m}_T$	Turbine mass flow	kg/s
N	Cylinder number	-
NOx	Nitrogen oxides	-
n	Engine rotational speed	rpm
n_d	Polytropic index	-

n_{TC}	Turbocharger rotational speed	rpm
$n_{TC,0}$	Initial turbocharger rotational speed	rpm
O_C	Oxygen concentration ratio	-
OH	Hydroxide	-
P_i	Indicated power	kW
P_b	Brake power	kW
P_e	Actual horsepower received by the crankshaft	kW
P_m	Power consumed by losses	kW
p	In-cylinder pressure	Pa
p_0	In-cylinder pressure at motoring condition	Pa
$p_{C,in}$	Compressor inlet pressure	Pa
$p_{C,out}$	Compressor outlet pressure	Pa
p_{EO}	In-cylinder pressure at exhaust valve open	bar
$p_{T,in}$	Turbine inlet pressure	Pa
$p_{T,out}$	Turbine outlet pressure	Pa
p_a	In-cylinder pressure at inlet valve close	Pa
p_{com}	Compression pressure	bar
p_{cooler}	Intercooler outlet pressure	Pa
p_{ex}	Exhaust pressure	Pa
p_m	Manifold pressure	bar
p_{max}	Maximum in-cylinder pressure	Pa
p_s	Inlet pressure	Pa
Q_T	Accumulated heat release	J
$\dot{Q}_{comb}$	Energy release rate caused by the fuel combustion	J/°CA
$\dot{Q}_{loss}$	Heat loss from in-cylinder gas to cylinder walls	J/°CA
$R_{g,C,in}$	Gas constant of the compressor inlet air	J/(kg·K)
R_u	Universal gas constant	J/(mol·K)
S	Engine stroke	m

SOC	Start of combustion in Wiebe function	°CA
SOx	Sulfur oxides	-
T	In-cylinder temperature	K
T_a	In-cylinder temperature at inlet valve close	K
$T_{C,in}$	Compressor inlet temperature	K
$T_{C,out}$	Compressor outlet temperature	K
T_{cooler}	Intercooler outlet temperature	K
T_m	Manifold temperature	K
T_{norm}	Reference temperature for specific heat calculation	K
T_{shift}	Shift temperature for specific heat calculation	K
T_{wall}	Average cylinder wall temperature	K
$T_{w,in}$	Inlet temperature of cooling water	K
T_s	Inlet temperature	K
u	Specific internal energy	J/kg
u_1	Specific internal energy in burnt zone	J/kg
u_2	Specific internal energy in unburnt zone	J/kg
V_1	Burnt zone volume	m^3
V_2	Unburnt zone volume	m^3
V_a	In-cylinder volume at inlet valve close	m^3
V_s	Cylinder displacement	m^3
x	In-cylinder air mass fraction	%
x_b	Burnt fuel fraction	%

Greek letters

α_1	Crank angle corresponding to maximum pressure	°CA
$\alpha_{g\rightarrow w}$	Instantaneous heat transfer coefficient	$J/(K \cdot m^2)$
$\Delta\varphi_i$	Duration of each combustion stage in multi-Wiebe function	°CA
η_C	Compressor efficiency	%

η_T	Turbine efficiency	%
η_{cooler}	Intercooler effectiveness	%
θ	Normalised temperature	-
λ_t	Total air-fuel equivalence ratio in dual fuel engines	-
μ_e	Flow coefficient of exhaust valve	-
μ_s	Flow coefficient of inlet valve	-
ξ	Combustion rate	J/°CA
π_C	Compression ratio	-
π_T	Expansion ratio	-
ρ	Density	kg/m^3
σ	Stoichiometric air-fuel ratio	-
τ_v	Normalized combustion time in Wiebe function	-
φ_i	Start of each combustion stage in multi-Wiebe function	°CA

Chapter 1. Introduction

1.1 Chapter Outline

This chapter provides a brief background of the maritime environmental impacts and current solutions, as well as the aim and objectives of this thesis. Subsequently, the thesis layout and overview, innovation and contribution are discussed, whilst concluding with the chapter summary.

1.2 Background

1.2.1 Marine emission regulations and solutions

As one of the most important transportation modes, cargo shipping accounts for about 80% of the global logistics market share and consequently plays a dominant role in global air pollution. The majority of the existing ships and more than 90% of the ordered ships are fuelled by one or more grades of oil refined from crude oil, which has the disadvantages of high NOx, SOx and Greenhouse Gas (GHG) emissions [1]. To control the marine emissions, the Marine Environmental Protection Committee (MEPC) of the International Maritime Organisation (IMO) approved the revised MARPOL Annex VI [2] in 2008. The Tier NOx emission limits apply to all the marine diesel engines with a power output higher than 130 kW. The Tier II limit enforced since 2011 is reduced by about 18% compared to the Tier I limit, whilst the Tier III implemented since 2016 is around 25% of the Tier II limit. Tier I and Tier II limits are global while the Tier III standard only applies in Emission Control Areas (ECAs), including the Baltic Sea, the North Sea, the North American and the US Caribbean ECAs. The SOx emissions of marine diesel engines are controlled by limiting the fuel sulphur content, which are specified as 0.1% in SOx ECA and 0.5% in global areas after 2020 [3], respectively. In addition, MARPOL Annex VI introduced two mandatory mechanisms – the Energy Efficiency Design Index (EEDI) and the Ship Energy Efficiency Management Plan (SEEMP) - to deal with the ship energy efficiency standard and GHG emissions problem [4]. An Initial Strategy on GHG emissions adopted by the IMO in 2018 is to reduce at least 50% of the total annual GHG emission by 2050 compared to 2008 [5]. Thus, coping with the increasingly stringent marine emissions regulations becomes an unavoidable issue for ship owners and engine manufactures.

To reduce the marine diesel engine emissions, various solutions have been proposed in terms of the targeted emission type. For NOx emissions reduction, a primary choice is combustion process optimisation on engine design and operating parameters including compression ratio [6], fuel injection strategies [7], valve timings [8], etc. Dedicated NOx emissions control technologies, such as exhaust gas recirculation (EGR) [9], selective catalytic reduction (SCR) [10] and water induction [11] are also studied and applied. The basic measure for the SOx emissions reduction is to use low-sulphur fuel oils (LSFO) or zero-sulphur fuels like Liquified Natural Gas (LNG) [12]. Exhaust gas cleaning systems (EGCS) [13] such as scrubbers [14] are also used as alternative measures to reduce sulphur emissions (as SOx). To meet the EEDI requirements and reduce GHG emissions, a number of measures have been applied, such as using alternative low-carbon or zero carbon fuels [15], CH_4 and Volatile Organic Compounds (VOC) after-treatment [16] and slow steaming [17].

As inferred from the above discussion, after-treatment auxiliaries are effective in reducing emissions but also increase the cost and complexity of the exhaust system. Using alternative fuels replacing traditional petroleum-based fuels is an attractive option to meet the increasingly stringent requirements of IMO emissions regulations. Liquified Natural Gas (LNG), which is recognised as a zero-sulphur and low-carbon fuel, have an apparent positive effect on reducing NOx, SOx and GHG emissions [18]. In addition, due to its higher octane number (120 in comparison with 87 for gasoline), natural gas exhibits a better antiknock performance, which allows the NG fuelled engines to employ a greater compression ratio for improving their thermal efficiency [19]. Thus, LNG has gradually been applied to marine internal combustion engines (ICE) replacing diesel and petrol for emissions reduction and efficiency improvement.

1.2.2 Liquified Natural Gas (LNG) Fuelled Engines

The NG fuelled engines are classified to the following three basic types: (a) spark ignition (SI) NG engines; (b) SI bi-fuel engines running on either gasoline or NG fuel (usually converted SI gasoline engines), and; (c) compression ignition (CI) dual fuel (DF) engines running on diesel and NG fuels (usually converted diesel engines) [20]. The latter can be further classified to premixed combustion DF engines and high-pressure direct gas injection DF engines (or gas diesel engines) according to the NG admission methods [21]. As the gasoline and NG fuels cannot be mixed and burnt simultaneously in the gasoline/NG bi-fuel engines [22], the thermal efficiency of these engines is constrained by the antiknock requirements of the gasoline fuel. This means that the NG advantages cannot be fully exploited in the bi-fuel engines. On the contrary, the SI natural gas engines [23] and diesel/NG DF engines [24] are designed with higher compression ratio to take advantage of the NG antiknock characteristics.

For the majority of the SI natural gas engines, the NG is injected in the intake manifold, where it mixes with the inflowing air forming a fuel-air mixture, which enters into the engine cylinders. At the end of the compression process, the NG-air mixture is ignited by a spark plug, thus generating a flame front, which travels within the combustion chamber with an almost constant velocity [25]. The compression ratio of the SI natural gas engines is typically kept in the range from 8:1 to 13:1 due to the higher NG octane number [26]. Although a higher power output is expected for the SI NG engines (in comparison to the gasoline engines with similar dimensions), there are two main factors limiting these engines power. The first is the reduced engine volumetric efficiency due to the lower density of the injected NG at the inlet conditions (the natural gas occupies a part of the air-gas fuel mixture trapped within the engine cylinders) [27]. The second is the advanced spark timing, which can be up to 10°CA earlier compared to gasoline engines, due to the slower flame front propagation speed. This results in increased pressure at the latest part of the compression phase, thus reducing the engine power output [28]. In order to compensate the power loss caused by the reduced volumetric efficiency, forced induction by employing supercharging or turbocharging is usually applied to increase the trapped air-NG mixture amount [29, 30]. Alternatively, NG direct injection into the engine combustion chamber can also be employed [31], however this is not a widely applied method due to the characteristics of the high-pressure gaseous fuel injection system. A measure that assists in increasing the flame propagation speed is the usage of a small amount of another fuel with higher flame speed (for example hydrogen) [32]. In this case, a retarded spark timing can be employed resulting in the engine power output increase.

For CI dual fuel engines, a small amount of diesel fuel is usually injected into the combustion chamber to initiate the NG ignition as the NG has a lower cetane number and can hardly be ignited by compression [33, 34]. This pilot injection provides a high energy source to ensure reliable and powerful ignition of the mixture, which is needed when running with a high specific cylinder output and lean NG air mixture [35]. In most premixed combustion DF engines, the NG-air mixture formation takes place outside the cylinder by inducting the NG into the manifold prior to the inlet valves closure [36]. This reduces the engine volumetric efficiency by 1-4% compared to the normal CI engines [34]. Direct gas injection technologies, including low-pressure gas injection and high-pressure gas injection, are applied to compensate the reduced volumetric efficiency by injecting the gaseous fuel directly into the cylinders. The low pressure gas injection takes place during the compression phase, whilst the high pressure gas injection initiates close to the Top Dead Centre (TDC) [21]. For the premixed combustion DF engines, the NG-air mixture is exposed to the compression process and hence to increasing pressure and temperature levels. This may lead to severe knocking and thus constrains the compression ratio of the premixed combustion DF engines, resulting in lower thermal efficiency compared to their diesel alternatives [37]. High pressure direct injection makes the gaseous fuel follow a diesel combustion process [21], which renders the engine practically insensitive to the fuel knocking properties and achieves similar thermal efficiency with that of diesel engines. However, due to the complexity and associated cost of the fuel feeding system, direct gas injection engines are typically used for high power output ranges. The investigated DF engine herein refers to a premixed combustion DF engine with inlet port/manifold NG injection.

1.2.3 Dual-fuel Engine Challenges

Diesel-LNG DF engines show remarkable advantages of reducing NOx, SOx, particulate matter (PM) and CO_2 emissions, but usually are accompanied with increased brake specific fuel consumption (BSFC), unburnt hydrocarbon (UHC) and CO emissions [38], which is also called the performance-emissions trade-off. The reduction of SOx and CO_2 can be simply explained by LNG’s zero-sulphur and low-carbon characteristics, whilst the NOx emission reduction is mainly caused by the lower in-cylinder temperature due to the higher specific heat capacity of lean air-NG mixture [39]. On the other hand, the lower in-cylinder temperature results in lower brake thermal efficiency (BTE) and consequently higher BSFC. The NOx-BSFC trade-off of DF engines are apparent at low operating loads, whilst simultaneous reduction of NOx emissions and BSFC seems possible at high operating loads [40]. DF engines emit less PM emissions as the major employed fuels are gaseous fuels and usually well premixed with air before the ignition starts, which generates less solid particles for PM formation during the combustion process [41]. The main reason for the increased UHC and CO emissions is the incomplete combustion due to the lean air-NG mixture conditions, wall flame quenching or crevices effects [42]. In cases where the DF engines are designed with valve overlap, the NG fuel escape during the scavenging process may also contribute to the total UHC emissions [43].

Another challenge faced by the premixed combustion DF engines is the combustion instabilities, namely, the misfiring and knocking phenomena. Misfiring is an abnormal engine operating condition with incomplete or no combustion for one or more engine cylinders and/or cycles. As the NG-air mixture exhibits a low flame front velocity [44], the flame in NG-fuelled engines propagates slowly, which causes combustion instability with high cyclic variation [45]. When the flame front propagation ceases, misfiring and incomplete combustion may occur in the end-gas zone, which results in low efficiency and high unburnt hydrocarbon (HC) emissions [46]. Knocking is associated with the auto-ignition of the unburnt fuel-air mixture ahead of the flame front [47]. It is a common instability in the premixed combustion engines [48], which may cause severe damages to the engine structure [49]. For avoiding these combustion instabilities, the NG-fuelled engines must operate at a relatively narrower air-fuel ratio range compared to diesel engines with similar dimensions. It is important to achieve the desired combustion behaviour whilst limiting the knocking occurrence. Since the knocking probability increases with higher in-cylinder temperature and pressure, the engine compression ratio must be kept below a maximum threshold for ensuring the engine knock-free operation. This, however, limits the engine efficiency.

As concluded from the above discussion, DF engines face several challenges in terms of their combustion instabilities and performance-emissions trade-off. Therefore, it is meaningful to study on DF engines' combustion characteristics and subsequently, use the obtained knowledge to optimise the engine design/operating settings for achieving better performance and less emissions.

1.3 Motivation of the present study

To meet the increasingly stringent requirements of the IMO emissions regulations, alternative fuels like LNG have been gradually applied to marine internal combustion engines replacing traditional petroleum-based fuels. The investigated engine is a premixed combustion DF engine, which is mainly fuelled by LNG and ignited by injecting a small amount of pilot diesel fuel. Although marine DF engines exhibit significant advantages of reducing NOx, SOx, particulate matter (PM) and CO_2 emissions, there still remain some challenges that must be effectively addressed, including the performance-emissions trade-off and combustion instabilities.

To this end, a novel combustion characterisation method is proposed to explore the dual fuel combustion characteristics and the possibility of simultaneous reduction of NOx emissions and BSFC. To address the constraints of the considerable experimental costs and extended timelines, the present study is undertaken by employing simulation techniques and limited experimental data. A 3D simulation model was developed in the CONVERGE software to investigate the in-cylinder combustion characteristics of the investigated DF engine and perform the parametric study of the operating settings effects. In order to reduce the computational cost, a 0D/1D simulation model is proposed for the optimisation, which employs a multi-objective genetic algorithm. A response model based on the Wiebe combustion function is calibrated by using the derived HRR by the 3D simulation. This study presents a comprehensive investigation of the combustion characteristics and performance-emissions trade-off for the investigated DF engines.

1.4 Aim and Objectives

The aim of this research is to investigate the in-cylinder combustion details and to optimise the performance-emissions trade-off of marine dual fuel engines by proposing a novel combustion characterisation method. The specific objectives related to the above aim are provided as follow:

1. To investigate the existing challenges faced by DF engines and identifying the research gaps by carrying out critical review, as well as propose a novel research framework for solving the research gaps (Addressed in Chapter 1 and Chapter 2).

2. To propose the research approach and introduce modelling methodologies of the employed simulation models (Addressed in Chapter 3).

3. To set up engine experiment for model validation and design the case studies (Addressed in Chapter 4).

4. To develop the proposed 3D and 0D/1D simulation models and validate the accuracy by using experimental data measured from the investigated DF engine (Addressed in Chapter 5)
5. To explore the detailed combustion and emissions characteristics of DF engines under different operating loads by using the developed 3D simulation model. (Addressed in Chapter 6).
6. To propose a novel combustion characterisation method for DF engines. (Addressed in Chapter 6).
7. To optimise the performance-emission trade-off of DF engines by using multi-objective genetic algorithm. (Addressed in Chapter 6).

1.5 Research framework

The research framework of this thesis is presented in Figure 1.1, which illustrates all the methodological steps for achieving the thesis aim and objectives, addressing the research gaps identified in the critical literature review. A 0D/1D simulation model is proposed to perform the engine settings optimisation, whilst a 3D simulation model is employed to calibrate the 0D combustion model and investigate the combustion details. The 0D/1D simulation model consists of a two-zone 0D combustion model and a 1D gas exchange model, which are implemented and coupled in the GT-ISE software. The DF engine combustion is characterised by employing Wiebe combustion model, which can be calibrated by using heat release rate (HRR) obtained from engine experiment or CFD simulation. The 3D simulation model is developed in the CONVERGE software by considering the coupling of computational fluid dynamic and chemical reaction. An experiment is conducted on the reference DF engine to obtain operating parameters for validating the two proposed simulation models. The prediction accuracy of the 0D/1D model is validated by a quantitative comparison between the simulated and measured in-cylinder pressures as well as performance parameters, whilst 3D simulation model is validated by using HRR, in-cylinder pressure and emissions. Subsequently, the validated simulation models will be used to perform the following case studies: (1) individual effect study and parametric investigation on the combustion process and emissions by using 3D simulation model; (2) HRR obtained from 3D simulation are used to calibrate the 0D Wiebe combustion model by using Response Surface Methodology (RSM); (3) the calibrated Wiebe combustion model is applied to the proposed 0D/1D simulation model, which is further employed to perform the engine settings optimisation. Finally, the novel output of this thesis will be summarised.

1.6 Thesis layout

The present thesis includes seven chapters, as illustrated in Figure 1.1. A brief introduction to each chapter summarising the research tasks, main contents and key achievements follows.

Chapter 1. Introduction

The first chapter introduces the major challenges faced by marine DF engines and highlight the research motivation, as well as the aim and objectives of the present study. Subsequently, the research framework and thesis layout are presented.

Chapter 2. Critical review

Methods of engine optimisation, engine modelling and combustion characterisation are critically reviewed, and the research gaps are identified. It is inferred that a combined use of 0D/1D simulation model and 3D simulation model accompanied with MOGA algorithm could be an effective solution to these research gaps.

Chapter 3. Research approach and modelling methodologies

The research approach flow for conducting this study and the modelling methodologies for the proposed 0D/1D and 3D simulation models are presented.

Chapter 4. Experiment setup and case studies design

The reference engine and engine test facilities for model validation are introduced firstly. Then, three case studies are designed for addressing the research gaps by employing the proposed simulation models. The three case studies are presented as follow:

Case study 1: parametric investigation by using 3D simulation model

The calibrated 3D simulation model is used to study the combustion characteristics and performance-emissions trade-off of the investigated DF engine at three operation conditions covering medium and high operation loads. A parametric investigation is performed to explore the potential simultaneous reduction of NOx emissions and BSFC.

Case study 2: Wiebe combustion model calibration

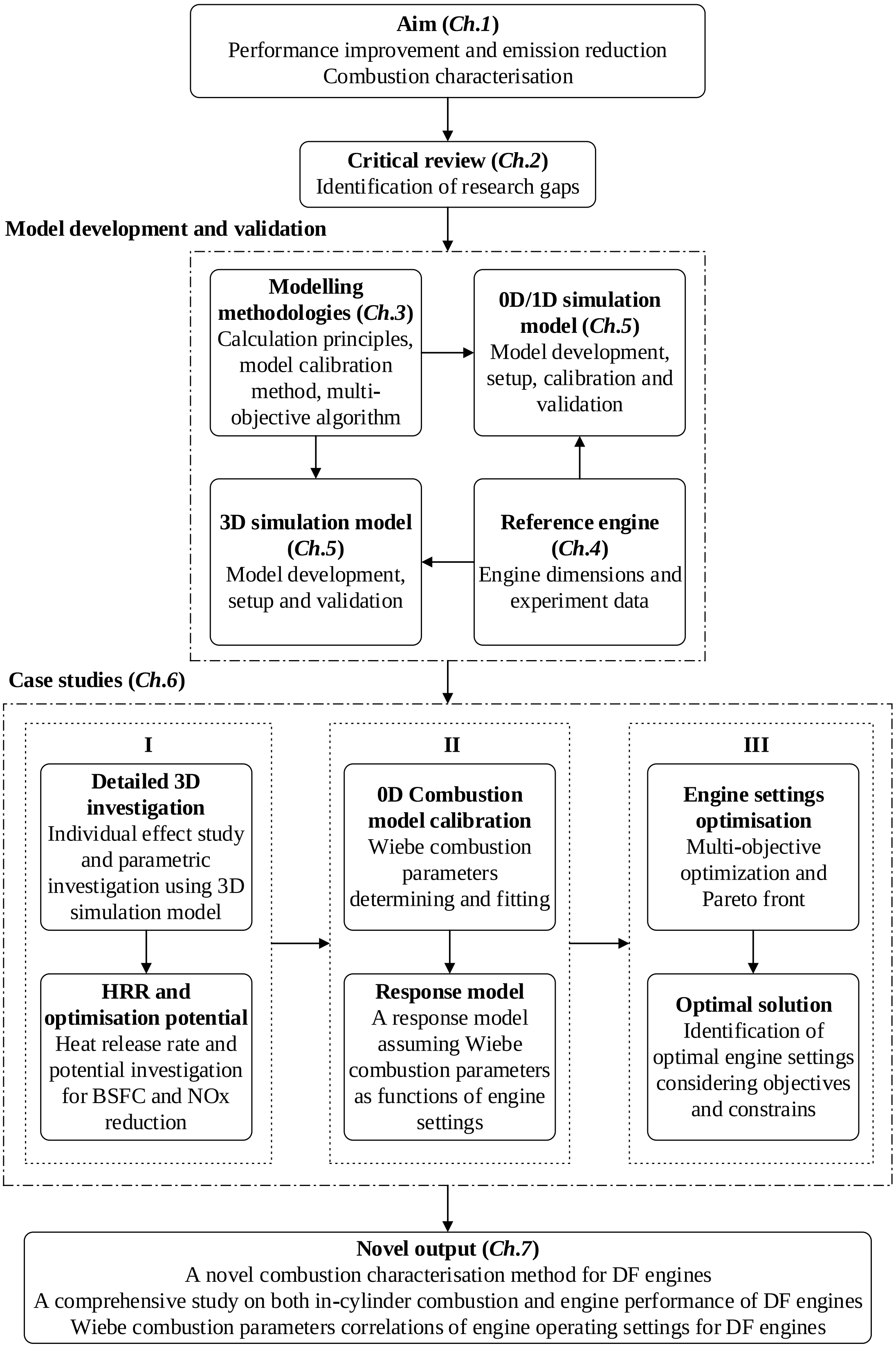

Figure 1.1 Research framework and thesis layout

A double-Wiebe and a triple-Wiebe functions will be compared and selected in terms of the accuracy and complexity for determining the Wiebe combustion parameters from the 3D simulated HRR. Then, a response model will be proposed by assuming that the Wiebe combustion parameters are functions of pilot injection timing, equivalence ratio and natural gas mass.

Case study 3: engine operating setting optimisation

The calibrated Wiebe combustion model will be applied to the proposed 0D/1D simulation model, which is further combined with a multi-objective evolutionary algorithm to optimise the NOx emissions-BSFC trade-off.

Chapter 5. Model development and validation

The modelling methodologies and engine dimensions are used to develop the proposed 0D/1D and 3D simulation models, which are subsequently validated by using the measured pressure and emissions.

Chapter 6. Results and discussions

The derived results of 3D parametric investigation, Wiebe combustion model calibration and engine operating setting optimisation are presented and discussed.

Chapter 7. Conclusions and recommendations

The main conclusions, study limitations and recommendations are summarised whilst the future research directions are discussed.

1.7 Chapter summary

The increasingly stringent IMO emissions regulations prompt the wide application of dual fuel engines due to their positive effect on reducing emissions. Nevertheless, marine DF engines are challenged by the performance-emissions trade-off and combustion instabilities, which motivates the research work presented in this study. Furthermore, the aim and objectives as well as the layout of this study are illustrated.

Chapter 2. Critical review

2.1 Chapter Outline

This chapter firstly presents the critical review of engine optimisation including the classification of optimisation algorithms and optimisation methods. Subsequently, physical engine models such as mean value models, zero-dimensional (0-D) or one-dimensional (1-D) models, and three-dimensional (3-D) models are compared in terms of computation speed and prediction accuracy for optimisation use. Engine combustion characterisation methods based on Wiebe functions are also critically reviewed to investigate the prediction accuracy and applicability for DF engines optimisation. Finally, the key findings and existing research gaps are identified.

2.2 Engine optimisation

2.2.1 Classification of optimisation algorithms

The commonly-used engine optimisation methods can be classified into three types: direct optimisation [50, 51], traditional non-evolutionary algorithms [52-54], and intelligent algorithms [55-60] based on evolutionary strategy. The direct optimisation method [50, 51] is to investigate the effects of single or multiple parameters on the engine performance/emissions, and subsequently select the optimal solution by comparing the derived results. The first optimisation method is the simplest and with the lowest robustness because the derived solution is constrained by the pre-set input groups. Besides, the exponentially increased computational cost with more input parameters makes the direct optimisation method only suitable for cases where only a few parameters need be optimised. The traditional non-evolutionary algorithms, such as the conjugate gradient method [52], the adaptive gradient method [53] and the sequential quadratic programming [54], are more efficient than the direct optimal selection in multi-objective optimisation. However, the performance of the second optimisation methods highly depends on the searching gradient of the input parameters space. Intelligent optimisation algorithms [55-60] imitate natural phenomena or swarm behaviours with population-based iterations, determining the optimal result from the whole searching scope by continuously selecting the optimal individuals in each generation. Based on the imitation objectives, intelligent optimisation algorithms can be further categorised to genetic algorithms (GA), simulated annealing algorithms (SAG), particle swarm algorithms (PSA), ant colony algorithms (ACA), hill climbing algorithms (HCA), etc. [61]. The randomised iterative characteristics render intelligent algorithms the capability of solving complex continuous or NP-hard discrete problems, as well as finding feasible suboptimal solutions for complex problems [62].

2.2.2 Genetic algorithms

Genetic algorithms, which are inspired by natural selection process using biologically operators such as mutation, crossover and selection, are prominent for their high-quality solutions to optimisation and searching problems [63]. For internal combustion engine optimisation, genetic algorithms have been used in different ways, including the basic versions [58, 64], refined versions [55, 65-67] and joint use with other intelligent algorithms [58, 60]. Millo et al [64] developed a specifically conceived GA-based optimiser aiming at a simultaneous reduction of NOx emissions and BSFC while maintaining other emissions of an automotive diesel engine. Hiroyasu [55] employed the neighbourhood cultivation genetic algorithm (NCGA) to reduce the NOx emissions, soot emissions and the specific fuel consumption of a heavy-duty diesel engine by optimising the operating settings, including boost pressure, EGR rate, injection timing, injection duration and swirl ratio. Kim et al. [65] used the micro-genetic algorithms (MGA) and a KIVA-3V based 3D simulation model to optimise the injection strategies of a heavy-duty diesel engine. Jaliliantabar et al. [66] established a mathematical model of a small biodiesel engine equipped with EGR and employed the non-dominated sorting genetic algorithm II (NSGA II) to optimise the engine settings for a simultaneous reduction of the CO, HC, and NOx emissions, smoke and BSFC, while retaining the engine power. Stoumpos & Theotokatos [67] optimised the operating settings of a marine four-stroke dual fuel engine equipped with exhaust gas recirculation and air bypass systems (ABS) by employing the NSGA III to render the diesel mode compliant with Tier III requirements. Bertram & Kong [60] proposed a novel particle swarm and genetic algorithm hybrid method (PSO-GA), which was verified in Zhang et al. [58] by performing a comparative study against the basic GA.

Among all the aforementioned genetic algorithms [55, 58, 60, 64-67], the NSGA series (NSGA, NSGA II and NSGA III) is one of the most advanced GAs because of its prominent searching ability, fast convergence and high robustness dealing with multi-objective optimisation. The Pareto dominance is employed in NSGA [68] for sorting the population into a hierarchy of sub-groups in each generation, whilst the similarity between members of each sub-group is evaluated on the Pareto front, resulting in a diverse front of non-dominated solutions. NSGA II [69] employs the Pareto ranking method for selecting individuals in each generation and uses the crowding distance (the distance from an individual to its nearest neighbour) as the following selection criterion to guarantee the even distribution of Pareto solutions. In the further upgraded version NSGA III [70], the selection criterion is changed from crowding distance to reference points, which makes NSGA III more appliable when three or more objective functions are involved [71]. In this study, NSGA II is sufficient for conducting the engine setting optimisation which includes two objective functions - minimise BSFC and minimise NOx emissions.

2.2.3 Fitness evaluating functions for engine optimisation

Prior to conducting an engine optimisation, the fitness evaluating functions of intelligent optimisation must be obtained first, i.e., determining the relationship between the targeted objectives (performance, emissions) and the input parameters (engine settings). The fitness evaluating functions can be developed by using black-box response models like Response surface methodology (RSM) [72], artificial neural network (ANN) [56]， support vector machine (SVM) [73]. No matter which method is used, the training data is a key factor affecting the accuracy of the fitness evaluating functions and subsequently the optimisation performance.

Measured engine responses [56, 66, 74] or simulation results of physical engine models [67, 75] are usually employed as training data for developing the fitness evaluating functions. With regard to measured engine responses, Jaliliantabar et al. [66] used RSM for developing mathematical models correlating five engine performance parameters (NOx, HC, CO, smoke and BSFC) to four factors (engine load, engine speed, EGR rate and biodiesel percent) for optimising a compression ignition engine using biodiesel fuel and EGR. Lotfan [56] employed artificial neural networks (ANN) and NSGA II for modelling and optimising a direct injection dual fuel engine, aiming at a simultaneous reduction of CO and NOx emissions. Experiment data was used for developing the proposed ANN model, which considered the engine speed, power, intake temperature, diesel mass flow and gaseous fuel mass flow as controllable inputs. d’Ambrosio [74] experimentally optimised the double pilot injection strategies to reduce the emissions, combustion noise and BSFC of a Euro 5 diesel engine at low, medium and high operating loads by using a Design of Experiments (DOE) method. With regard to physical engine model, Ge et al. [75] optimised a car diesel engine by using a multi-objective genetic algorithm coupled with the 3D KIVA3V code, which was conducted using high-throughout computing with the CONDOR system. Stoumpos & Theotokatos [67] developed a 0D/1D simulation model of a marine four-stroke dual fuel engine equipped with exhaust gas recirculation and air bypass systems and optimised the operating settings by employing the multi-objective genetic algorithm NSGA III to render the diesel mode compliant with the 'Tier III' requirements.

The prominent advantage of the experiment-based method is to provide a direct and accurate fitness evaluating function, saving the effort of developing physical engine models. Nevertheless, it could be costly to conduct such an engine test because both RSM and black-box models require a large amount of training data. In addition, experiment-based response models cannot support comprehensive investigation on detailed process of engine operation. On the other hand, the model-based method is more cost-effective whilst the optimization performance would be significantly affected by the accuracy of the employed physical engine model. Thus, the combined use of an intelligent algorithm and a well-calibrated 0D/1D simulation model could be a compensating way between optimisation performance and computational cost, as well as providing a comprehensive understanding of the engine behaviour and subsystems interactions.

2.3 Engine modelling

2.3.1 Physical engine models

Engine modelling and simulation contribute towards obtaining a better understanding of the engine components characteristics during the engine design phase; therefore, they can be employed for performing the engine settings optimisation. In general, simulation models for internal combustion engines can be classified as follows (from simpler to more complicated): mean value models, zero-dimensional (0-D) or one-dimensional (1-D) models, and three-dimensional (3-D) models [76].

The mean value models are usually set up and calibrated by using a large amount of engine test data and are not capable of predicting the in-cylinder parameters variations

[77]. The 0-D models employ the assumption of uniform variations of the working media state and concentration within the engine components, and are quite effective for engine performance prediction [78]. For predicting knocking occurrence or NOx emissions of internal combustion engines, the in-cylinder needs to be divided into at least two zones (the burnt zone and the unburnt zone), in order to characterise the flame propagation and end-gas auto-ignition [79, 80]. Thus, the 0-D combustion models for knocking prediction are commonly associated with the cylinder volume division similarly to the two-zone models [81, 82] and multi-zone models [83-85]. Xiang et al. [81] proposed a two-zone model for predicting knocking performance and NOx emissions of a SI natural gas engine by assuming that the burnt and unburnt zones have a cylindrical shape. Javaheri et al. [85] studied the influence of the natural gas composition on the knocking combustion in SI gas engines with a three-zone approach, which characterised the reactions in the burnt zone by chemical equilibrium calculations. The 3-D Computational Fluid Dynamics (CFD) models are capable of providing the most detailed analysis of the engine in-cylinder combustion processes when knocking occurs, adequately predicting the pre-flame reaction [86], the heat release rate [87] and emissions formation [88]; therefore, they are appropriate for obtaining better insight of the involved thermo-physical-chemical processes. However, 3-D models have disadvantages of high complexity and massive computational effort [89], which may limit their application in performance prediction. In order to improve the prediction accuracy, 1-D models for modelling the manifolds are occasionally used coupling with 0-D combustion models, as the combustion process is significantly affected by the air–fuel ratio obtained during the gas-exchange process [90]. Noda et al. [91] proposed a transient knocking prediction technique for SI engines by coupling a 0-D knocking model with chemical kinetics and a 1-D gas exchange model.

As concluded from the discussed literature [81-85], a two-zone 0-D model could be an effective tool for analysing knocking behaviour and NOx emissions in NG engines as it is capable of characterising the burnt zone and unburnt zone temperatures with the simplest combustion zone division. In addition, a 1-D model [90, 91] could be employed for simulating the gas exchange process in order to improve the simulation accuracy of the entire engine cycle. Thus, a two-zone 0-D combustion model coupled with a 1-D gas exchange model could effectively be employed for predicting the engine performance, knocking and NOx emissions compromising between the model complexity and the required computational cost.

2.3.2 DF engine combustion characterisation

For characterising the DF engine combustion in a 0D simulation model, semi-empirical formulas are usually employed to simulate the combustion Heat Release Rate (HRR). Typically, the HRR determining methods include the Triangular Exothermic function, the Polygon-hyperbola function and the Wiebe function [92], among which the Wiebe function is most widely used. Mikulski [93] modelled the natural gas combustion with first order oxidation macro-reactions for the main combustible mixture components: CH_4, C_2H_6 and C_3H_8, whilst characterising the diesel combustion with a Wiebe function. Aklouche et al. [94] proposed a single-zone predictive model of a diesel engine operating in dual fuel mode by using a double-Wiebe function to predict the HRR. Alla [95] and Pirouzpanah [96] investigated the combustion characteristics of a dual-fuel (diesel-natural gas) with detailed chemical kinetics for the NG combustion and two Wiebe functions for the premixed combustion and diffusion combustion of the pilot diesel fuel, respectively. Bilcan [97] developed a DF engine combustion model by employing three Wiebe functions for three combustion phases –the premixed combustion of diesel fuel, the premixed combustion of gaseous fuel and the diffusion combustion. Liu and Karim [98] developed a thermodynamic multi-zone model incorporating detailed kinetic schemes for the prediction of the combustion processes in dual-fuel engines, which employed two Wiebe functions for the pilot diesel combustion and another two Wiebe functions for the natural gas combustion. Xiang [99] parametrically investigated the knocking performance of DF engines by employing a two-zone 0D combustion model based on double-Wiebe function, which was validated against experimentally measured parameters.

As concluded from the preceding discussion, Wiebe combustion functions can be used individually or coupling with detailed chemical kinetics for characterising the combustion of dual fuel engines. When individually used, at least two Wiebe functions are needed for an accurate representation of the HRR because the investigated DF engine herein refers to a premixed combustion DF engine, thus exhibiting the characteristics of both premixed combustion and diffusion combustion.

2.3.3 Wiebe combustion model calibration

Although Wiebe combustion model has been widely used for predicting HRR due to its cost-effective characteristics, its main disadvantage is the data required for its calibration process. The engine performance can be adequately predicted only when all the involved Wiebe combustion parameters have been calibrated in advance, which limits the application of Wiebe combustion model to combustion analysis and engine development.

For traditional diesel engines and gasoline engines, there have been plenty of studies dealing with the calibration of Wiebe combustion parameters, using empirical correlations [100], downhill gradient search method [101], least square regression [102], partial least square regression [103] and artificial neural network [104]. Miyamoto [100] conducted a series of experiments on a direct injection diesel engine and an indirect injection diesel engine to derive the correlations of Wiebe combustion parameters and engine operating parameters. It was concluded that three of the six determining parameters in a double-Wiebe function are constant, whilst the other three are considered as linear functions of injection delay and the injection mass during ignition delay. Witt [101] used the 'downhill gradient search method' to determine the variables of a double-Wiebe function for characterising a diesel engine combustion, which proved to be effective if weighting factors and initial filtering are chosen carefully. Tolou et al. [102] obtained the first five parameters (b_1, m_1, m_2, $\Delta\theta_1$ and $\Delta\theta_2$) of a two-Wiebe functions by using a nonlinear least-squares optimisation based on MATLAB Curve Fitting Toolbox and determined the *SOC* by employing the criterion proposed in Katrašnik et al. [105]. Then, the Wiebe parameters correlations were further developed to a predictive combustion model for gasoline direct-injection (GDI) engines. Sunet al. [103] related the double Wiebe parameters of a sequential turbocharging diesel engine to the operating conditions by using partial least square regression, which was found to be more accurate than using least square regression in solving multiple correlations among operating conditions. Torregrosa [104] pointed out that the least square regression can be only used for determining Wiebe function parameters at a given load/speed condition and thus proposed an ANN model based on experiment data to estimate the Wiebe function parameters of a SI engine for different operating conditions.

On the contrary, the studies for determining the Wiebe function parameters of dual fuel engines are quite few. Liu [106], Alla [95] and Pirouzpanah [96] used Miyamoto's correlations [100] for characterising the premixed and diffusion combustion of the pilot fuel whilst employing detailed chemical kinetics for simulating the combustion in diesel-NG DF engines. Bilcan [97] proposed a schematic algorithm for determining the three sets of Wiebe parameters (φ_i, $\Delta\varphi_\mathrm{i}$, b_i and m_i) from measured in-cylinder pressure for characterising the combustion of a diesel-LPG dual fuel engine. Aklouche et al. [94] determined the six parameters of a double-Wiebe function by using the least squares method based on the experimental HRRs obtained from a dual fuel engine. Stoumpos et al. [107] employed a triple-Wiebe function for representing the combustion process of dual fuel engines and stored the calibrated Wiebe combustion parameters at steady operating conditions in a database, which could be used to determine the Wiebe combustion parameters at transient operation conditions by using quadratic interpolation.

As concluded from the above investigations, Wiebe parameters determining methods for diesel engines and gasoline engines have been extensively studied, whilst some of the proposed correlations were proved to be of high accuracy. However, the Wiebe parameters determining methods for DF engines are quite limited to the tentative use of diesel correlations, experiment-based calibration or interpolation. There is no ready-to-use and predictive correlations for the Wiebe function parameters in the frame of DF engines. Therefore, it is necessary to develop the correlations of Wiebe combustion parameters for DF engines, the characteristics of which greatly vary from conventional diesel and gasoline engines due to the coupling combustion of pilot diesel and natural gas.

2.4 Key findings and research gaps

The following key findings were concluded from the preceding literature review:

1. Intelligent algorithms have been widely used for engine optimisation due to their capability of solving complex continuous or NP-hard discrete problems. Among all the mentioned intelligent algorithms [36, 39, 41, 48-51], NSGA II is one of the most advanced GAs and proves to be a reliable tool for multi-objective engine optimisation.

2. Engine optimisation methods which employ experiment or physical engine models for developing fitness evaluating functions can achieve high robustness and provide detailed information of engine operation. But it could be also costly when engine test or complex physical model (like 3D simulation model) are used because intelligent optimisation usually requires a large amount of training data. Thus, the combined use of intelligent algorithms and 0D/1D simulation models could be a compensating way between optimisation performance and computational cost, as well as providing a comprehensive understanding of the engine operation.
3. As concluded from the engine modelling review, a two-zone 0D model could be an effective tool for predicting the performance and NOx emissions of DF engines as it is capable of characterising the end-gas zone temperature with the simplest combustion zone division. In addition, an 1D model could be employed for simulating the gas exchange process in order to improve the simulation accuracy of the entire engine cycle. Thus, a two-zone 0D combustion model coupled with a 1D gas exchange model could effectively be employed for predicting both the engine performance as well as NOx emissions between the model complexity and the required computational cost.
4. Pertinent studies focused on the in-cylinder thermodynamic parameters of specific liquid or gaseous fuels and cannot be used directly for the DF engines modelling, which requires approaches with great flexibility in the fuel types and compositions.
5. The heat release rate of DF engine combustion can be represented with high accuracy by employing two or more Wiebe functions if appropriate methods are applied to calibrate the Wiebe function parameters.
6. Wiebe parameters determining methods for diesel engines and gasoline engines have been extensively studied, whilst some of the proposed correlations proved to be predictable with high accuracy. The Wiebe parameters determining methods for DF engines are quite limited to the tentative use of diesel correlations, experiment-based calibration or interpolation. There is no ready-to-use and predictive correlations for the Wiebe function parameters in the frame of DF engines.

This study aims to address the following research gaps:

1. A lack of comprehensive studies on the combustion characteristics, engine performance and emissions of marine four-stroke dual fuel engines from the aspects of both 3D and 0D/1D levels.
2. A lack of time-saving and cost-effective methodologies for calibrating Wiebe function parameters of marine DF engines by using experiment-based 3D simulation model rather than conducting large amount of experiment.
3. A lack of correlations for predicting Wiebe function parameter with the operating settings of DF engines, whose characteristics differ greatly from conventional diesel and gasoline engines due to the complexity of the employed fuels.

2.5 Chapter summary

This chapter critically reviewed the engine optimisation, engine modelling and combustion characterisation, which are followed by the derived key findings and research gaps. It is concluded that a combined use of 0D/1D simulation model and intelligent algorithm NSGA II could be an effective tool for the DF engines optimisation, whilst an experiment-validated 3D simulation model could be used for calibrating the Wiebe combustion model of the employed 0D/1D simulation model.

Chapter 3. Modelling Methodologies

3.1 Chapter outline

This chapter presents the modelling methodologies of the 3D simulation model and 0D/1D simulation model, which are followed by the Wiebe combustion model calibration and multi-objective optimisation method.

3.2 Research approach

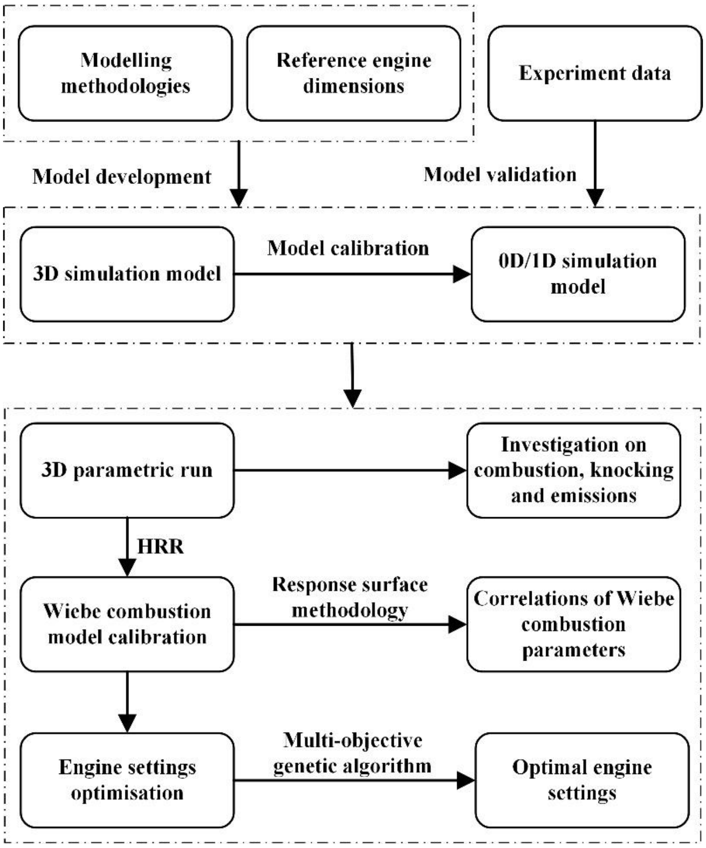

Figure 3.1 Research approach flow

Figure 3.1 presents the research approach flow of this thesis. It is illustrated that the modelling methodologies and reference engine dimensions are used to develop the 0D/1D and 3D simulation models, accuracy of which are validated by using experiment data including measured in-cylinder pressure, performance parameters and emissions. The 0D/1D simulation model is proposed for the coupling use with multi-objective genetic algorithm compromising between the model complexity and the required computational cost, whilst the 3D simulation model is used to produce HRR over a large operation range for calibrating the 0D/1D simulation model due to the limited experiment data. It is crucial to validate the accuracy of the 3D model which acts as a 'virtual' engine in the following study. Thus, the calibration of spray model and mesh size independence are justified before conducting the 3D simulation run, while the 3D simulated pressure, HRR and emissions (NOx, CO and HC) are compared to the experiment data. In addition, the heat losses of CFD model and HRR calculation model need be checked if they match because the simulated HRR is a direct product of the actual fuel consumption rate, whilst the experimentally obtained HRR is calculated from the measure in-cylinder pressure with heat loss estimation. Completing these procedures, the developed 3D simulation model can be considered as accurate and can be used for the following study. Subsequently, the validated 3D simulation model is used to perform a parametric run to investigate combustion details and produces HRR under various combination of engine operating settings. The 3D simulation HRR are subsequently analysed and processed for calibrating the 0D Wiebe combustion model, which renders the proposed 0D/1D simulation model the capability of predicting engine performance and NOx emission with sufficient accuracy. To reduce the complexity of Wiebe combustion model, a comparison of Double-Wiebe/Triple-Wiebe and linear/non-linear response models are conducted considering the prediction accuracy of engine performance. Finally, the calibrated 0D/1D simulation model will be jointly used with multi-objective genetic algorithm NSGA II to conduct an engine settings optimization dealing with the BSFC-NOx emissions trade-off.

3.3 Modelling methodology of 0D/1D simulation model

As concluded in Section 2.3.1, a two-zone 0D combustion model coupled with a 1D gas exchange model could be an effective tool for predicting engine performance and NOx emissions of dual fuel engines. The modelling of the investigated DF engine must consider all the engine components including cylinders, inlet/exhaust system, turbocharger, intercooler and speed governor. Table 3.1 presents the detailed information of the employed modelling theories for each engine component. For characterising the in-cylinder process, a two-zone 0D simulation model is used, whilst a single-zone 0D simulation model is employed for the gas-exchange process. The modelling approaches for heat transfer and gas properties can be used during both in-cylinder and gas-exchange process with corresponding coefficients adjustment or composition calculation. The inlet and exhaust mass flow rates during the gas exchange process are calculated based on the pressure difference by considering the occurrence of sonic flow and subsonic conditions. The 1D simulation theory is used for modelling the inlet and exhaust systems by assuming that the inlet/exhaust system consist of a series of connections and one-dimensional pipes. The turbocharger system is modelled by using measured MAP and rotational equilibrium. The output temperature of the intercooler is calculated by employing an estimated cooler effectiveness. For modelling the speed governor, a PI controller and an injection map are used for describing the natural gas injection and pilot diesel injection, respectively.

Table 3.1 Modelling theories employed for developing the 0D/1D simulation model

Sub-models			Modelling theory	
Cylinders	In-cylinder		Two-zone 0D model	
	Gas-exchange		Single-zone 0D model	
		Basic equations		Ideal gas equation, Mass and energy conservation
		Heat transfer		Woschni formula
		Heat release		Wiebe functions
		Gas properties		Fitting formula (Ideal but non-prefect gas)
		Inlet/exhaust flow		Calculation formula based on pressure difference
Inlet/Exhaust system			1D model	
Turbo-charger	Compressor		Compressor map	
	Turbine		Turbine map	
	Rotational equilibrium		Newton's second law	
Intercooler			Estimated cooling coefficient	
Speed governor			PI Control for natural gas injection, MAP for pilot diesel injection	

3.3.1 Calculation principles for modelling cylinders

This section describes the cylinder modelling principles employed for characterising in-cylinder and gas-exchange process of DF engines. A number of sub-models are introduced for calculating ignition delay, combustion heat release, heat transfer, in-cylinder gas properties, inlet/exhaust mass flow, volume balance of two-zone 0D model and NOx emissions. The specific assumptions for developing the simulation model are outlined as follows.

1. The working medium inside each zone is uniformly distributed, which indicates that its pressure, temperature and concentration are the same inside each zone.
2. The in-cylinder gas is considered to be ideal but non-perfect. Thus, its thermodynamic properties can be calculated as functions of its temperature and composition.
3. Blowby and valves leakage in the engine cylinder are not considered.

(1) Ignition delay

The ignition delay period in any compression ignition engine is well acknowledged to be very important and has a profound and controlling effect on almost all features of the subsequent combustion processes as well as engine performance and output [108]. The ignition delay period is usually defined as the time interval from start of liquid fuel injection to start of combustion [47]; the ignition delay can also be defined on the basis of mass fraction burnt curve, as the angle between the time of injection and the time at which 1% of the mass fraction is burned [109]. This delay period consists of a physical delay wherein atomisation, vaporisation and mixing of air and fuel occur as well as a chemical delay attributed to pre-combustion reactions.

In the case of dual fuel engines, the ignition delay was found to be longer compared to diesel engines [110]. This can be attributed to several interacting effects including: reduced oxygen partial pressure due to air displacement by gaseous fuel; reduced temperature and pressure during the initiation of the ignition as methane has a higher heat capacity than air; pre-ignition reaction activities between methane and air may affect those between diesel and air; increased residuals concentration at high loads. There are clear indications that existing diesel ignition delay correlations cannot be used directly for dual-fuel situations [111]. Liu and Karim [112] suggested that the ignition delay in dual fuel engine operation, in principle can be correlated in terms of the type of gaseous fuel employed, its concentration and other operating conditions. Piętak [113] recommended for modelling ignition delay in a dual-fuel engine to use Assanis formula [114] in cases where the diesel fuel energy accounts for more than 20% of the total fuel energy, whereas the non-autonomic method of Prakash [115] was recommended in smaller diesel energy percentages. The pilot diesel amount of the targeted engine is around 10%, thus the Prakash correlation is used in this study.

Prakash [115] modified the Hardenberg & Hase correlation [116], which calculates the diesel fuel ignition delay, for DF engines combustion by considering the temperature changes at the end of compression stage and the charge oxygen concentration. As the variation in the manifold temperature with load (BMEP) is negligibly small, the effect of load was included in the modified correlation by replacing the manifold temperature T_m to the charge temperature at BDC, T_{BDC}. The experimental data for calibration was obtained from a four-stroke dual-fuel engine of a single-cylinder with power of 12.5 kW. This correlation can be used if the relevant parameters corresponding to the diesel operating mode and the properties of the gaseous fuel along with its concentration in the intake charge are known. The derived correlation is described by Eq (3.1) to (3.6).

$$\mathrm{ID} = \mathrm{A} \cdot C_f \cdot O_C^k \exp\left(E \cdot P + Q^{0.63}\right) \tag{3.1}$$

$$\mathrm{A} = \left(0.36 + 0.22 c_m\right) \tag{3.2}$$

$$O_c = \frac{p_{O_2}}{0.21 \cdot p} \tag{3.3}$$

$$E = \frac{618840}{CN + 25} \tag{3.4}$$

$$P = \frac{1}{R_u \cdot T_m \cdot C_r^{n_d - 1}} - \frac{1}{17190} \tag{3.5}$$

$$Q = \frac{21.2}{p_m \cdot c_r^{n_d} - 12.4} \tag{3.6}$$

Where, c_m is the mean piston speed in m/s; C_f is a coefficient used for correcting the difference of polytropic index suggested by Hardenberg & Hase [116] and the measured data; O_C is the oxygen concentration ratio, which can be calculated from the oxygen concentration, $0.5 \le O_C \le 1.0$; the value of the constant k was obtained by using least squares regression comparing the predicted and measured ignition delay; E is the activation energy given as a function of the cetane number 'CN' as suggested by Hardenberg & Hase [116]; R_u is the universal gas constant, 8.3145 J/(mol·K); T_m is the manifold temperature in K; C_r is the compression ratio; n_d is polytropic index; p_m represents the manifold pressure in bar.

(2) Combustion heat release

The burnt fuel fraction represented by a single Wiebe function [117] can be calculated by the following equation:

$$x_b = 1 - e^{-a\cdot\tau_v{}^{m_v+1}} \tag{3.7}$$

where, x_b is the burnt fuel fraction; a is the coefficient related to the combustion efficiency, which is usually set at 6.9078 to maintain a combustion efficiency of 99.9%; τ_v is the normalized combustion time; and m_v is the shape factor.

The heat release rate of internal combustion engines can be represented by employing several Wiebe combustion functions. Generally, two Wiebe functions can sufficiently represent the combustion process of a direct injection diesel engine, which consists of a premixed combustion stage and a diffusion combustion stage. One Wiebe function is capable of characterising the combustion process of a premixed gas engine because it shows the main characteristics of premixed combustion. For modelling the combustion of a premixed DF engine, at least two Wiebe functions are needed for an accurate representation of the HRR because premixed DF engines exhibit the characteristics of both premixed combustion and diffusion combustion. The reaction fraction and Heat Release Rate (*HRR*) of dual fuel engines can be calculated by using Eq (3.8) and Eq (3.9).

$$X = \sum_{i=1}^{M} b_i \cdot \left(1 - e^{-a\cdot\tau_{v,i}{}^{m_{v,i}+1}}\right) \tag{3.8}$$

$$HHR = \sum_{i=1}^{M} \dot{X} \cdot Q_T \tag{3.9}$$

where, M is the number of the employed Wiebe functions; b_i is the weigh factor of each Wiebe function, $\sum_{i=1}^{M} b_i = 1$; $\tau_{v,i}$ and $m_{v,i}$ are the normalized combustion time and shape factor of each Wiebe function, respectively; Q_T is the accumulated heat release.

(3) Heat Transfer

The cylinder walls include three parts: the surface of the cylinder head and valves, the surface of the cylinder liner and the top surface of the piston. The temperature of each part of the heat transfer surface is considered to be constant as its variation is small enough to be neglected compared to the in-cylinder gas temperature. The Woschni model [118] is considered for calculating the instantaneous heat transfer coefficient

$\alpha_{g\rightarrow w}$ from the in-cylinder gas to walls. The heat transfer between the working medium and the cylinder walls is calculated according to the following equation:

$$\dot{Q}_{\text{loss}} = \sum_{1}^{3}\left[\alpha_{g\rightarrow w}\cdot(T - T_{wall,i})\cdot A_{wall,i}\right] \tag{3.10}$$

where, $\alpha_{g\rightarrow w}$ is the instantaneous heat transfer coefficient from the in-cylinder gas to the walls; $T_{wall,i}$ is the average wall temperature of each surface. i=1, 2, 3, which represents the cylinder head and valves, the cylinder liner and the cylinder piston respectively; and $A_{wall,i}$ is the heat transfer surface area.

The heat transfer coefficient $\alpha_{g\rightarrow w}$ can be calculated by using Eq (3.11).

$$\alpha_{g\rightarrow w} = 3.01426\cdot p^{0.8}\cdot T^{-0.5}\cdot D^{-0.2}\left[C_1\cdot c_m + C_2\frac{T_a\cdot V_s}{p_a V_a}(p - p_0)\right]^{0.8} \tag{3.11}$$

where, p is the in-cylinder pressure (bar); T is the in-cylinder temperature (K); D is the cylinder bore (m); p_a, T_a and V_a are the pressure (bar), temperature (K) and volume (m^3) at the inlet valve closure, respectively; V_s is the cylinder displacement (m^3); p_0 is the in-cylinder pressure at motoring conditions (bar); c_m is the average piston speed (m/s); C_1 is the coefficient depending on the airflow velocity; C_2 is the coefficient related to combustion chamber.

(4) In-cylinder gas properties

Assuming that the in-cylinder gas behaves as an ideal but non-prefect gas, the thermodynamic parameters of each species only depend on the in-cylinder temperature and can be obtained by the power series equation that varies with the normalized temperature according to Eq (3.12). Yaws [119] and Borman [120] obtained the fitting coefficients of various types of gases by using experimental methods.

$$c_{p,j} = \sum_{k=1}^{l} a_{k,j}\,\theta^{k-1} \tag{3.12}$$

where, a_k is the fitting coefficient of specific heat at constant pressure; θ is normalized temperature, $\theta = (T - T_{shift}) / T_{norm}$; T_{shift} is the shift temperature, T_{shift}=0 K; T_{norm} is the reference temperature, T_{norm}=1000 K.

The specific heat at constant volume of each species can be calculated by using the gas constant and the molar mass, according to the following equation.

$$c_{v,j} = c_{p,j} - R_j / M_j \tag{3.13}$$

The specific enthalpy and internal energy of each species can be calculated by Eq (3.14) and Eq (3.15), respectively.

$$h_j = \int c_p dT + h_j^{ref} = \sum_{k=1}^{l} \frac{a_{k,j}}{k} \cdot T_{norm} \cdot \theta^k - \sum_{k=1}^{l} \frac{a_{k,j}}{k} \cdot T_{norm} \cdot \theta_{ref}^k + h_j^{ref} \tag{3.14}$$

$$u_j = \int c_v dT + u_j^{ref} = h_j - R_j \cdot T \tag{3.15}$$

where, h_j^{ref} and u_j^{ref} are specific enthalpy and internal energy at standard conditions; θ_{ref} is normalized reference temperature.

Since each species in air, gaseous fuel and stoichiometric gas are considered ideal but non-prefect gases, the mixtures behave as ideal but non-prefect as well. Thus, the specific heat, enthalpy and internal energy of the considered mixtures are functions of the average temperature and their composition. A power series of the normalized temperature is used to fit these property data for all the species and the properties of the mixtures can be obtained considering ideal mixtures.

The in-cylinder working gas properties, i.e., the specific heat, specific enthalpy and specific internal energy, can be calculated by species property data and composition fractions according to the following equation:

$$f(x,T) = \sum_{l}^{L} x_l \left(\sum_{j=1}^{J} x_j \; f_j(T) \right) \tag{3.16}$$

where, T is the average in-cylinder temperature; $f_j(T)$ is the property data (c_v, h and u) for each basic species; x_j is the mass fraction of the considered mixture constituents; x_l is the mass fraction of air, gaseous fuel and stoichiometric gas.

(5) Inlet and exhaust mass flow

As the cylinders keep exchanging mass and energy with the ambient environment during the gas-exchange process, the mass flowing into and out the cylinders need to be calculated in order to solve the mass and energy conservation equations. At the initial exhaust period, the large pressure difference between the cylinder and exhaust pipes may cause supercritical flow through the exhaust valves, which would turn to subcritical flow with the pressure difference decrease. The outlet mass flow through the exhaust valve can be calculated by Eq (3.17) and Eq (3.18) by using the ratio of the exhaust pressure and in-cylinder pressure determining the flow condition.

When $\frac{p_{ex}}{p} \leq \left(\frac{2}{k+1}\right)^{\frac{k}{k-1}}$, the gas flow is identified as sonic, the exhaust mass flow can be calculated by the following equation:

$$\frac{dm_e}{dt} = \mu_e \cdot A_{\mathrm{v,ex}} \frac{p}{\sqrt{R_g T}} (\frac{2}{k+1})^{\frac{1}{k-1}} \cdot \sqrt{\frac{2k}{k+1}} \tag{3.17}$$

When $\frac{p_{ex}}{p} > \left(\frac{2}{k+1}\right)^{\frac{k}{k-1}}$, the gas flow is identified as subsonic the exhaust mass flow can be calculated by the following equation:

$$\frac{dm_e}{dt} = \mu_e \cdot A_{v,,ex} \frac{p}{\sqrt{R_g \cdot T}} \cdot \sqrt{\frac{2k}{k-1}[(\frac{p_{ex}}{p})^{\frac{2}{k}} - (\frac{p_{ex}}{p})^{\frac{k+1}{k}}]} \tag{3.18}$$

Where, p_{ex} is the exhaust pressure, Pa; p is the in-cylinder pressure, Pa; k is the instantaneous adiabatic exponent of in-cylinder gas; μ_e is the flow coefficient of the exhaust valves; $A_{v,ex}$ is the flowing area of exhaust valves, m^2; R_g is the gas constant of the in-cylinder mixture, J/(kg·K); T is the in-cylinder temperature, K.

The mass flow through the inlet valves is normally identified as subcritical flow because of the small pressure difference between the inlet pipes and the cylinder. The inlet mass flow through the inlet valve can be calculated by Eq (3.19).

$$\frac{dm_s}{dt} = \mu_s \cdot A_{\mathrm{v,in}} \frac{p_s}{\sqrt{R_s \cdot T_S}} \cdot \sqrt{\frac{2k_s}{k_s-1}[(\frac{p}{p_s})^{\frac{2}{k_s}} - (\frac{p}{p_s})^{\frac{k_s+1}{k_s}}]} \tag{3.19}$$

Where, μ_S is the flow coefficient of the inlet valves; $A_{v,in}$ is the flowing area of inlet valves, m^2; p_s is the inlet pressure, Pa; R_s is the gas constant of the inlet mixture, J/(kg·K); T_S is the inlet temperature, K; k_S is the instantaneous adiabatic exponent of the inlet mixture.

(6) Two-zone combustion methodology

For physical combustion process of dual fuel engines, the in-cylinder space is separated as a high-temperature zone and a low-temperature zone by the flame front. In GT-POWER, the two-zone combustion model is characterised based on the flowing assumptions:

1. At the start of combustion, the in-cylinder space is discretized in two zones – burnt zone and unburnt zone, whilst the pressure at any time is uniform throughout the cylinder. The in-cylinder temperature is separated as burnt

temperature and unburnt temperature, which is uniform in their own zone. There is no heat transfer between the two zones.

2. At each simulation step, a mixture of fuel and air is transferred from the unburnt zone to burnt zone. The amount of fuel-air mixture is determined by burnt rate, which can be calculated by employing Wiebe combustion functions.
3. A chemical equilibrium calculation is carried out in the burnt zone considering all the atoms of each species (C, H, O, N) for obtaining the equilibrium concentrations of combustion products (N_2, O_2, H_2O, CO_2, CO, H_2, N, O, H, NO and OH).
4. Once the new composition in burnt zone is obtained, the thermodynamic parameters (internal energy, enthalpy, specific heat) of each species are calculated. Applying the energy conservation equation and ideal gas state equation, the temperatures of burnt zone and unburnt zone can be calculated.

According to the assumptions, sub-models for each zone are zero-dimensional. The subscript 1 and 2 will be respectively used to describe parameters related to burnt zone and unburnt zone. Eq (3.20) is the basic equation of the simulation model for burnt zone, which is derived from the First Law of Thermodynamics by separating temperature terms.

$$\frac{d\left(m_1 u_1\right)}{dt} = -p\frac{dV_1}{dt} - Q_{loss,1} - \left(\frac{dm_f}{dt}h_f + \frac{dm_a}{dt}h_a\right) \tag{3.20}$$

Energy conservation in unburnt zone is presented as Equation (3.21):

$$\frac{d\left(m_2 u_2\right)}{dt} = -p\frac{dV_2}{dt} - Q_{loss,2} + \left(\frac{dm_f}{dt}h_f + \frac{dm_a}{dt}h_a\right) + \frac{dm_{f,i}}{dt}h_{f,i} \tag{3.21}$$

Where, m_1 and m_2 are separately the gas mass in burnt zone and unburnt zone; u_1 and u_2 are the specific internal energy of burnt zone and unburnt zone, respectively; p is in-cylinder gas pressure; V_1 and V_2 are the burnt zone volume and unburnt zone volume, respectively; $Q_{loss,1}$ and $Q_{loss,2}$ are heat loss flow from in-cylinder gas to cylinder wall in burnt zone and unburnt zone, respectively; m_f, $m_{f,i}$ and m_a are the mass of natural gas, injected diesel and air, respectively; h_f, $h_{f,i}$ and h_a are the enthalpy of natural gas, injected diesel and air, respectively.

(7) NOx emissions prediction

NOx sub-model is developed in this two-zone model to describe the NOx formation and consumption. While nitric oxide (NO) and nitrogen dioxide (NO_2) are usually grouped together as NOx emissions, nitric oxide is the predominant oxide of nitrogen produced inside the cylinder. The NO formation has been modelled using a well-known extended Zeldovich oxidation mechanism [47] with three reactions in Eq (3.22). The equilibrium approach is used, which assumes that the residence time in the flame is short enough to be neglected, thus the NO formation only takes place in the burnt zone.

$$\begin{aligned} &\mathrm{O+N_2} \underset{k_{b1}}{\overset{k_{f1}}{\rightleftarrows}} \mathrm{NO+N} \\ &\mathrm{N+O_2} \underset{k_{b2}}{\overset{k_{f2}}{\rightleftarrows}} \mathrm{NO+O} \\ &\mathrm{N+OH} \underset{k_{b3}}{\overset{k_{f3}}{\rightleftarrows}} \mathrm{NO+H} \end{aligned} \tag{3.22}$$

According to Eq (3.23), NO concentration can be calculated with temperature assuming that main in-cylinder species reach to equilibrium in a negligible time:

$$\begin{aligned} \frac{d(\mathrm{NO})}{dt} = {} & k_{f1}(\mathrm{O})(\mathrm{N_2}) - k_{b1}(\mathrm{NO})(\mathrm{N}) + k_{f2}(\mathrm{N})(\mathrm{O_2}) - k_{b2}(\mathrm{NO})(\mathrm{O}) \\ & + k_{f3}(\mathrm{N})(\mathrm{OH}) - k_{b3}(\mathrm{NO})(\mathrm{H}) \end{aligned} \tag{3.23}$$

Where, ( ) represent the concentrations of different species (mol/cm^3), k_{f1}, k_{b1}, k_{f2}, k_{b2}, k_{f3}, k_{b3} are temperature related reaction rate coefficients (cm^3/mol/s).

3.3.2 Calculation principles for modelling other engine components

(1) Inlet and exhaust system

When GT-ISE is used for modelling the inlet and exhaust systems, connections and pipes are discretized into a series of 1D grids based on the Gas Flowing Dynamics, which assumes the inside gas is uniform flow. Thus, the thermodynamic properties of inlet and exhaust systems can be obtained by using the mass continuity equation, momentum and energy conservation equation, as presented in Eq (3.24), Eq (3.25) and Eq (3.26). The enthalpy of the flowing gas can be calculated by Eq (3.27). The flowing state is characterised by using scales including density, internal energy, pressure, temperature, enthalpy and component concentration, and vectors like mass flow, speed. Vectors are calculated at the boundary between grids, whilst scales located at the grid centre are considered as constant.

$$\frac{dm}{dt} = \Sigma m_{flx} \tag{3.24}$$

$$\frac{d(m_{flx})}{dt} = \frac{dpA + \Sigma(m_{flx} \cdot v) - 4C_f \frac{\rho v^2}{2} \frac{dxA}{D} - C_P \left(\frac{1}{2} \rho v^2 \right) A}{dx} \tag{3.25}$$

$$\frac{d(me)}{dt} = \Sigma(m_{flx} \cdot h) + p \frac{dV}{dt} - h_g A \left(T_{gas} - T_{wall} \right) \tag{3.26}$$

$$\frac{d(\rho hV)}{dt} = \Sigma\left(\rho v A_{eff} h \right) + V \frac{dp}{dt} - h_g A \left(T_{gas} - T_{wall} \right) \tag{3.27}$$

Where, m_{flx} represents the mass flow at grid boundary, kg/s; p, V and m are the pressure, volume and mass in each grid, respectively; ρ *is* the density in kg/m^3; A is the flowing area, m^2; e is the total internal energy, which equals the sum of internal energy and kinetic energy, J; h is enthalpy in J/kg; h_g is the heat transfer coefficient from gas to pipe wall, J/K/m^2; v is the flowing speed at grid boundary, m/s; D is the pipe diameter, m; C_f and C_p are coefficients for surface friction and pressure loss; dx represents the flowing distance between grids in m, whilst dp is the pressure loss within dx in Pa.

(2) Turbocharger

A turbocharger system usually consists of a turbine and a compressor which are connected by a rigid shaft. When a turbocharger system operates at steady conditions, there would be three equilibrium relationships: the torque equilibrium, the rotational speed equilibrium and the mass flow equilibrium between the compressor and the turbine. The detailed calculation principles are presented as follow.

(a) Compressor

The compressor torque can be calculated by

$$M_C = \frac{30}{\pi} \cdot R_{g,C,in} \cdot T_{C,in} \frac{\dot{m}_C}{\eta_C \cdot n_{TC}} \left[\left(\frac{p_{C,out}}{p_{C,in}} \right)^{\frac{k_C - 1}{k_C}} - 1 \right] \tag{3.28}$$

where, $R_{g,C,in}$ is the gas constant of the compressor inlet air, J/(kg·K); $T_{C,in}$ is the compressor inlet temperature, K; $\dot{m}_C$ is the compressor mass flow, kg/s; η_C is the compressor efficiency; n_{TC} is the turbocharger rotational speed, rpm; $p_{C,out}$ is the compressor outlet pressure, Pa; $p_{C,in}$ is the compressor inlet pressure, Pa; k_C is the adiabatic exponent of the compressor inlet gas.

According to Eq (3.28), apart from inlet/outlet pressure and temperature which can be obtained from the intercooler and inlet system models, the compression pressure ratio

π_C, the compressor efficiency η_C, the compressor mass flow $\dot{m}_C$ and the turbocharger rotational speed n_{TC} need to be determined by the measured MAP data before calculating the compressor torque. In the compressor MAP of the investigated engine is, the compressor mass flow $\dot{m}_C$ and the turbocharger rotational speed n_{TC} are converted into the equivalent mass flow $\dot{m}_{C,e}$ and equivalent rotational speed $n_{TC,e}$ at standard conditions. Any two of the mentioned parameters can be used to determine the rest two parameters. The equations of the compression pressure ratio π_C, the equivalent mass flow $\dot{m}_{C,e}$ and equivalent rotational speed $n_{TC,e}$ are presented as follow:

$$\pi_C = \frac{p_{C,out}}{p_{C,in}} \tag{3.29}$$

$$\dot{m}_{C,e} = \frac{\dot{m}_C \sqrt{T_{C,in}}}{p_{C,in} \cdot 10^{-6}} \tag{3.30}$$

$$n_{TC,e} = \frac{n_{TC}}{60\sqrt{T_{C,in}}} \tag{3.31}$$

According to the compressor MAP and Eq (3.29 - 3.31), the compressor mass flow $\dot{m}_C$ and the compressor efficiency η_C can be fitted as the function of the compressor inlet pressure $p_{C,in}$, the compressor outlet pressure $p_{C,out}$, the turbocharger rotational speed n_{TC} and the compressor inlet temperature $T_{C,in}$, as presented in Eq (3.32) and Eq (3.33).

$$\dot{m}_C = f_1\left(\pi_C, n_{TC}, T_{C,in}, p_{C,in}\right) = f_1\left(p_{C,in}, p_{C,out}, n_{TC}, T_{C,in}\right) \tag{3.32}$$

$$\eta_C = f_2\left(\pi_C, n_{TC}, T_{C,in}\right) = f_2\left(p_{C,in}, p_{C,out}, n_{TC}, T_{C,in}\right) \tag{3.33}$$

The compressor outlet temperature can be calculated by

$$T_{C,\text{ out}} = T_{C,\text{ in}} \left[1 + \frac{1}{\eta_C}\left(\pi_C^{\frac{k_c - 1}{k_C}} - 1\right)\right] \tag{3.34}$$

(b) Turbine

The turbine torque can be calculated by Eq (3.35) taking the exhaust system pressure and temperature as the input parameters of the turbine inlet gas.

$$M_T = \frac{30}{\pi} \cdot R_{g,B} \cdot T_B \frac{\dot{m}_T \cdot \eta_T}{n_{TC}} \left[1 - \left(\frac{p_{T,out}}{p_{T,in}}\right)^{\frac{k_T - 1}{k_T}}\right] \tag{3.35}$$

where, $R_{g,B}$ is the gas constant of the exhaust gas, J/(kg·K); T_B is the gas constant in the exhaust system, K; $\dot{m}_T$ is the turbine mass flow, kg/s; η_T is the turbine efficiency; n_{TC}

is the turbocharger rotational speed, rpm; $p_{T,out}$ is the turbine outlet pressure, Pa; $p_{T,in}$ is the turbine inlet pressure, Pa; k_T is the adiabatic exponent of the exhaust gas.

Similar with the compressor characteristics, the turbine efficiency η_T and turbine mass flow $\dot{m}_T$ can be determined by the expansion pressure ratio π_T and the turbine rotational speed n_{TC}. The expansion pressure ratio π_T, equivalent turbine mass flow $\dot{m}_{T,e}$ and equivalent turbine rotational speed $n_{TC,e}$ are calculated by Eq (3.36), Eq (3.37) and Eq (3.38), respectively.

$$\pi_T = \frac{p_{T,in}}{p_{T,out}} \tag{3.36}$$

$$\dot{m}_{T,e} = \frac{\dot{m}_T \sqrt{T_B}}{p_{T,in} \cdot 10^{-6}} \tag{3.37}$$

$$n_{TC,e} = \frac{n_{TC}}{60\sqrt{T_B}} \tag{3.38}$$

(c) Rotational equilibrium

According to Newton's Second Law, the rotational equilibrium of the turbocharger system can be described by Eq (3.39).

$$\frac{\pi \cdot I_{TC}}{30} \cdot n_{TC} = M_T - M_C \tag{3.39}$$

where, I_{TC} is the turbocharger rotational inertia, kg·m^2.

The instantaneous rotational speed of the turbocharger can be calculated by the following equation:

$$n_{TC} = \int \frac{30}{\pi \cdot I_{TC}} \left(M_T - M_C\right) \mathrm{d}t + n_{TC,0} \tag{3.40}$$

where, $n_{TC,0}$ is the initial rotational speed of the turbocharger.

The calculation flowchart of turbocharger sub-model is presented in Figure 3.2. The turbocharger model is developed based on the torque equilibrium and the rotational speed equilibrium, while using the mass flow equilibrium for model validation. In addition, the measured MAPs will be used to determine the mass flow and efficiency of the compressor and the turbine, respectively.

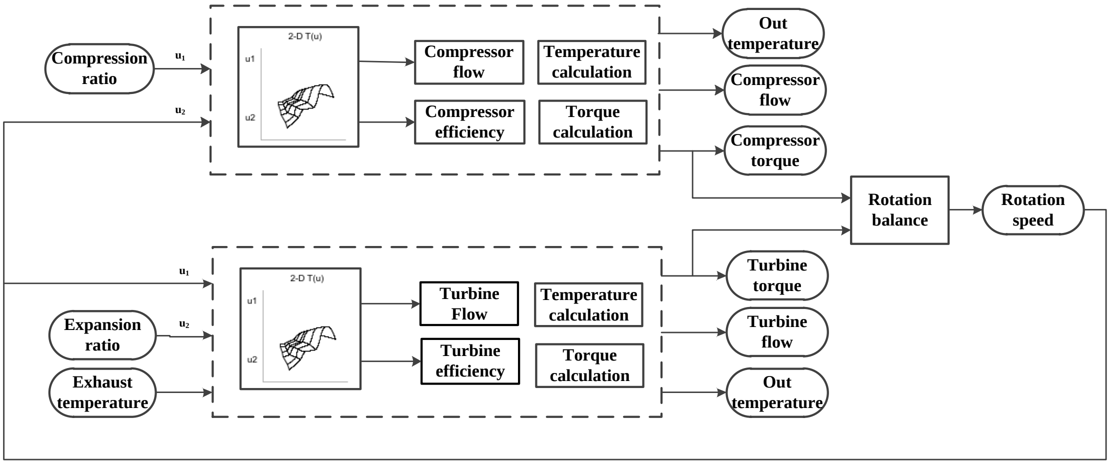

Figure 3.2 Calculation flowchart of the turbocharger sub-model

(3) Intercooler

The intercooler is used to cool down the high-temperature air flowing out the compressor for indrawing more fresh air into the cylinders, thus improving the cylinder charge coefficient. As the intercooler is located right after the compressor, the inlet pressure and temperature of the intercooler model are considered to be the same with the outlet pressure and temperature of the compressor model. The primary outputs of the intercooler model are the outlet temperature and pressure after the cooling down process, which will be used as input parameters of the inlet system model. The outlet temperature of the intercooler can be calculated by the following equation.

$$T_{cooler} = T_{C,out} - \eta_{cooler}\left(T_{C,out} - T_{w,in}\right) \tag{3.41}$$

where, T_{cooler} is the intercooler outlet temperature, K; $T_{C,out}$ is the compressor outlet temperature, K; $T_{w,in}$ is the inlet temperature of cooling water, K; η_{cooler} is the cooler effectiveness, $\eta_{cooler} = 0.7 \sim 0.9$.

The pressure loss and outlet pressure of the intercooler can be calculated by the following equations:

$$\Delta p = \Delta p_0 \cdot \left(\frac{\dot{m}_s}{\dot{m}_{s0}}\right)^2 \tag{3.42}$$

$$p_{cooler} = p_{C,out} - \Delta p \tag{3.43}$$

Where, Δp is the intercooler pressure loss, Pa; Δp_0 is the intercooler pressure loss at the design condition, which is usually between 300 and 500 Pa; $\dot{m}_s$ is the intercooler mass flow, kg/s; $\dot{m}_{s,0}$ is the intercooler mass flow at design condition, kg/s; p_{cooler} is the intercooler outlet pressure, Pa; $p_{C,out}$ is the compressor outlet pressure, Pa.

(4) Speed governor

For governing the rotational speed of the investigated dual fuel engine, the natural gas injection mass is controlled by an electronic control unit (ECU), whilst the pilot diesel injection mass is interpolated by a pre-set injection map. The ECU receives the instantaneous rotational speed transferred from the speed transducer and gives feedback of the instantaneous injection mass calculated by a PI controller. The rack position signal of natural gas injection mass $u(t)$ can be calculated by Eq (3.44).

$$u(t) = K_P \cdot \Delta n + \frac{1}{K_I}\int \Delta n \cdot dt \tag{3.44}$$

where, Kp is the proportionality constant; K_I is the integral constant; Δn *is* the difference between the instantaneous rotational speed and the targeted rotational speed, rpm.

The instantaneous injection mass of natural gas m_{NG} can be calculated by

$$m_{NG} = \left(u(t) + \frac{m_{NG,0}}{m_{NG,100}} \right) \cdot m_{NG,100} \tag{3.45}$$

where, $m_{NG,0}$ is the initial natural gas injection mass per cycle, kg/cyc; $m_{NG,100}$ is the natural gas injection mass per cycle at 100% operating load, kg/cyc.

(5) Engine torque

The indicated power, which is calculated by Eq (3.46), is partially consumed in overcoming the friction forces within the engine and setting the auxiliary mechanisms in motion.

$$P_i = \frac{n}{60000 \cdot K} \cdot N \oint p \cdot \mathrm{d}V \tag{3.46}$$

where, P_i is the indicated power, kW; n is the rotational speed, rpm; K is the stroke coefficient, K = 2 rev/cycle for four-stroke engines, K = 1 rev/cycle for two-stroke engines; N is the cylinder number; p is the instantaneous in-cylinder pressure, Pa; V is the instantaneous volume, m^3.

The indicated power can be defined as the sum of the power received by the crankshaft (actual horsepower) and the power consumed by losses (friction horsepower), as shown by Eq (3.47). Eq (3.48) presents the mechanical efficiency, which is defined as the ratio of the actual horsepower received by the crankshaft and indicated power produced by the cylinders.

$$P_{\mathrm{i}} = P_{\mathrm{e}} + P_{\mathrm{m}} \tag{3.47}$$

$$\eta_{\mathrm{m}} = \frac{P_{\mathrm{e}}}{P_{\mathrm{i}}} = \frac{P_{\mathrm{i}} - P_{\mathrm{m}}}{P_{\mathrm{i}}} = 1 - \frac{P_{\mathrm{m}}}{P_{\mathrm{i}}} \tag{3.48}$$

Where, P_e is the actual horsepower received by the crankshaft, kW; P_m is the power consumed by losses, including the friction loss, auxiliary equipment power loss and pumping loss.

In order to obtain the power consumed by the losses, the empirical formula proposed by Chen & Flynn [121] is used to estimate the mean mechanical loss pressure p_m in Eq (3.49). Then, the power consumed by losses can be calculated by Eq (3.50).

$$p_m = 13700 + 0.005 p_{\max} + 16200 c_m \tag{3.49}$$

$$P_{\mathrm{m}} = p_{\mathrm{m}} \cdot \frac{\pi \cdot D^2}{4} \cdot S \cdot \frac{n \cdot K}{60000} \cdot N \tag{3.50}$$

where, p_m is the mean mechanical loss pressure, Pa; p_{max} is the maximum in-cylinder pressure, Pa; c_m is the mean piston speed, m/s; D is the cylinder bore, m; S is the stroke, m; n is the engine rotational speed, rpm.

Combining Eq (3.46) to Eq (3.50), the engine torque M_e can be calculated by the following equation:

$$M_e = \frac{9550 P_e}{n} \tag{3.51}$$

3.3.3 Calculation flowchart

Figure 3.3 shows the calculation flowchart of the in-cylinder two-zone 0D model. A zero-dimensional model initially developed for diesel engines is extended with the consideration of the thermodynamic properties of gaseous fuels (NG, H_2) and is subsequently embedded into a two-zone NOx prediction model proposed in previous work [81], which enables the prediction of the engine performance and the NOx prediction. In the extended zero-dimensional model, the Wiebe model is used to calculate the combustion rate, which is then employed for the determination of the mass balance and instantaneous composition fraction. The properties library is built on the assumption that the thermodynamic properties of the in-cylinder gas are functions of the composition and the temperature, which provides the combustion heat, the internal energy, the enthalpy and the specific heat. The heat release rate is obtained by multiplying the combustion heat with fuel burning rate. The heat transfer coefficient in

Heat Loss sub-model is estimated by using the Woschni formula. The in-cylinder temperature is calculated by employing the First Law of Thermodynamics.

The overall model consists of a two-zone module for representing the combustion phase and a single-zone module for modelling the compression and expansion phases. Both modules are developed based on the extended single-zone zero-dimensional model. The combustion sub-model uses the multi-Wiebe function to estimate the heat release rate. The in-cylinder parameters, including the air fraction, as well as the pressure and temperature of the burnt zone are used to as input to calculate the NOx formation rate.

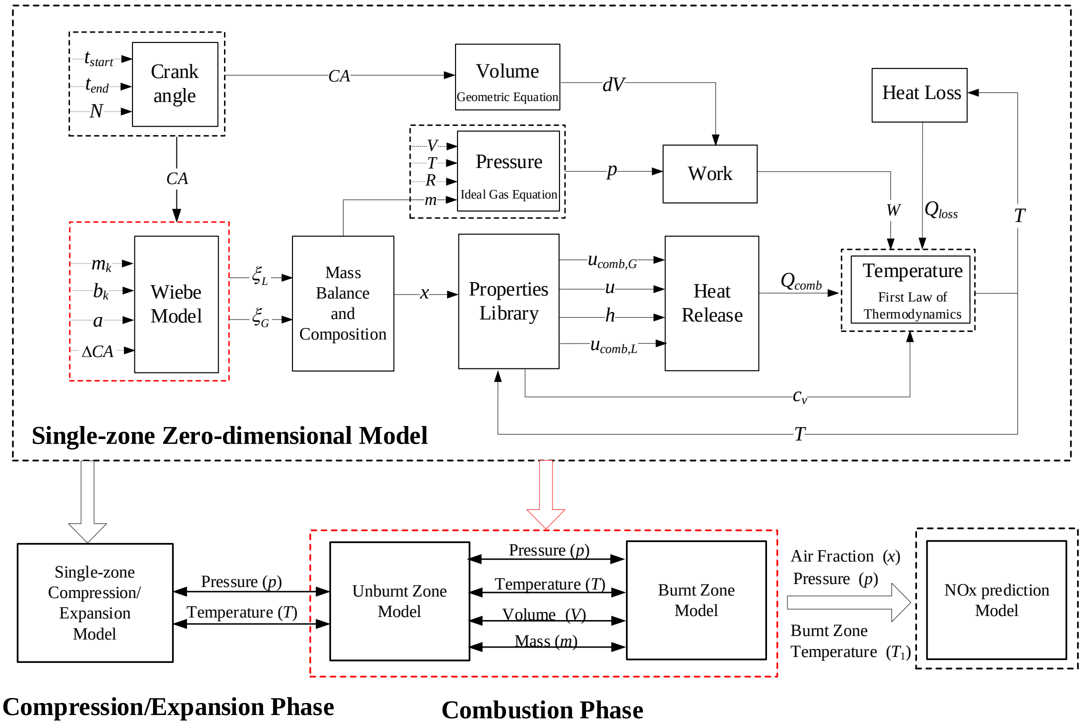

Figure 3.3 Calculation flowchart of the in-cylinder two-zone 0D model

The calculation flowchart of the investigated 0D/1D simulation model is shown in Figure 3.4. Starting from the inlet side, the working condition of the compressor is determined by the air flow, rotation speed, inlet pressure and inlet temperature. The outlet pressure, temperature and mass flow of the compressor are used as the input parameters of the intercooler to calculate the input pressure and temperature of the inlet system. In this study, both the intake and exhaust pipes are assumed to be one-dimensional (1D) systems. The mass flow through the intake valves and exhaust valves is calculated by considering the pressure difference in the gas exchange model. The pressure and temperature of the intake system serve as the boundary condition of the cylinder model, whilst the in-cylinder pressure and temperature are transferred to the exhaust system. To obtain the exhaust system parameters, it is necessary to calculate the mass flow out of the exhaust pipe, which is determined by the turbine model. In addition, the mean effective torque and instantaneous rotational speed of the engine are calculated according to the dynamics. Similar method is used for the calculation of the turbine torque and rotational speed. The injection rate of natural gas and pilot diesel are controlled by the governor according to the difference between the instantaneous rotational speed and pre-set rotational speed. As the natural gas is injected into the manifold and premixed with the inlet air in the investigated dual-fuel engine, the inlet system model needs to calculate the mass flow of inlet air and natural gas and makes sure that the entrapped fuel mass per cycle meet the requirement of the combustion. Due to the valve overlap, a portion of the entrapped natural gas flows into the exhaust pipes during the scavenging process. Thus, the exhaust gas is composed of combustion products, air and unburned natural gas.

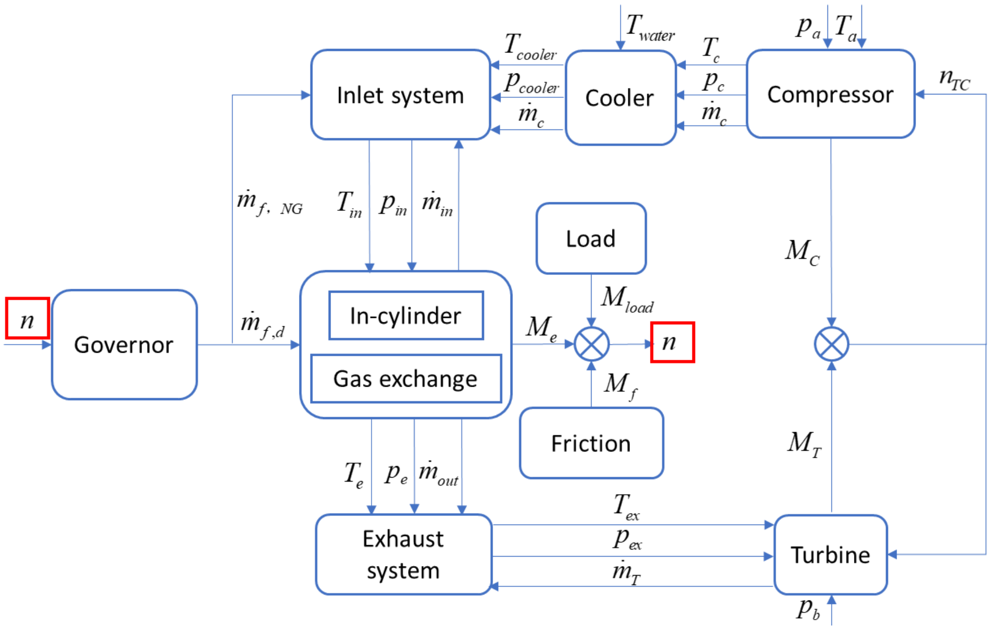

Figure 3.4 Calculation flowchart of the proposed 0D/1D simulation model

3.4 Modelling methodology of 3D simulation model

3.4.1 Calculation principles

In the proposed 3D simulation model, the statement of the in-cylinder mixture is governed by the conservation equations of mass transport, momentum transport and energy transport, as well as the ideal gas state equation. The detailed information of the employed mathematical models and chemical mechanisms are presented in Table 3.2. The Blob injection model, the KH-RT model and the Frossling model were selected to simulate the injection, breakup and evaporation process of the pilot diesel, respectively. The SAGE model was used to modelling the detailed chemical kinetics via the optimised GRI-Mech 3.0 and Valeri coupling mechanism. The NOx emissions were calculated by using the Extended Zeldovich mechanism. In addition, the RNG k-ε model and the Woschni model were employed to characterise the in-cylinder turbulence and heat transfer. As the Extended Zeldovich mechanism and Woschni heat transfer formulae have been presented in previous section, the governing equations, pilot injection sub-model, spray breakup sub-model, evaporation sub-model, combustion sub-model and turbulence sub-model will be introduced in this section.

Table 3.2 Employed mathematical models and chemical mechanisms in the 3D simulation model

Models/mechanisms	**Setting**
Pilot injection	Blob model [122]
Spray breakup	KH-RT model [123]
Evaporation	Frossling model [124]
Combustion	SAGE model [125]
Reaction kinetics	Optimized GRI-Mech 3.0 and Valeri coupling mechanism [126]
Turbulence	RNG k-ε model [127]
NOx formation	Extended Zeldovich mechanism [47]
Heat transfer	Woschni model [118]

(1) Governing equations

The commercial tool CONVERGE, which is developed by the Convergent Science, Inc, is featured with autonomous meshing, state-of-the-art physical models, advanced chemistry solver and the prominent ability of accommodating complex moving geometries, making CONVERGE a leading tool for CFD simulation [128]. In CONVERGE, the dynamics of fluid flow are governed by equations that describe the conservation of mass, momentum and energy. Additional equations describe the turbulence and the transport of passive scalars and species. The compressible equations for mass transport, momentum transport and energy transport are given by the following equations:

$$\frac{\partial \rho}{\partial t}+\frac{\partial \rho u_i}{\partial x_i}=S \tag{3.52}$$

$$\frac{\partial \rho u_i}{\partial \mathrm{t}}+\frac{\partial \rho u_i u_j}{\partial x_j}=-\frac{\partial P}{\partial x_i}+\frac{\partial \sigma_{ij}}{\partial x_j}+S_i \tag{3.53}$$

$$\frac{\partial \rho \mathrm{e}}{\partial \mathrm{t}}+\frac{\partial u_j \rho \mathrm{e}}{\partial x_j}=-P\frac{\partial u_j}{\partial x_i}+\sigma_{ij}\frac{\partial u_i}{\partial x_j}+\frac{\partial}{\partial x_j}\left(K\frac{\partial T}{\partial x_j}\right)+\frac{\partial}{\partial x_j}\left(\rho D\sum_m h_m\frac{\partial \gamma_m}{\partial x_j}\right)+S \tag{3.54}$$

Where, ρ is density; u is velocity, S is the source term; P is pressure; σ_{ij} is the stress tensor; e is the specific internal energy; K is the conductivity; D is the mass diffusion coefficient; h is the enthalpy; Υ_m is the mass fraction of species m.

The ideal gas state equation is defined as:

$$PV = mRT \tag{3.55}$$

Where, V is the volume; m is the mass; R is the gas constant; T is the temperature.

(2) Injection, spray and evaporation model

In order to simulate the injection process, the core angle, nozzle position, orientation and hole size were inputted to model the injector geometry. N-heptane was used to represent the flow properties of diesel fuel. According to the Blob injection model [122], the injected drop sizes are considered to be equal to the nozzle diameter or effective diameter. The pilot injection mass, injection timing, injection duration and injection pressure are used as inputs to calculate the injection mass flow. Since the pilot diesel is supplied by a common-rail system in the investigated engine, the injection pressure is considered to be constant during the injection duration.

The KH-RT breakup length model [123] is the concurrent application of the Kelvin-Helmholtz [129] breakup model and the Rayleigh-Taylor [130] breakup model. This model assumes that only KH instabilities are responsible for drop breakup inside of the characteristic breakup distance L_b, while both KH and RT mechanisms are activated beyond the breakup length. When the KH-RT model is activated, the break length L_b can be specified as Eq (3.56).

$$L_b = C_{bl}\sqrt{\frac{\rho_l}{\rho_g}}r_p \tag{3.56}$$

Where, C_{bl} is the break length constant [131], which can be tuned to increase or decrease spray breakup by changing the parameter *distant* in spray input document; ρ_l and ρ_g are the density of liquid and gas; r_p is the droplet radius before breakup.

The change rate of the droplet radius in a parent parcel is given by

$$\frac{dr_p}{dt} = -\frac{\left(r_p - r_c\right)}{\tau}, \quad \left(r_c \le r_p\right) \tag{3.57}$$

Where, r_c is the droplet radius after breakup; τ is the break time.

When the droplet is inside the characteristic breakup length L_b, the break time τ is determined by the KH model. τ_{AH} is given by

$$\tau_{KH} = \frac{3.726 B_1 r_p}{\Lambda_{KH} \Omega_{KH}} \tag{3.58}$$

Where, B_1 is the breakup time constant related to the initial disturbance level; Ω_{KH} is the maximum growth rate of a given set of flow conditions, Λ_{KH} is the corresponding wavelength.

When the droplet is outside the characteristic breakup length L_b, the RT model plays a dominant role. The break time τ_{RT} is calculated by

$$\tau_{RT} = \frac{C_{RT}}{\Omega_{RT}} \tag{3.59}$$

Where, C_{RT} is the RT size constant; Ω_{RT} is the maximum growth rate calculated by RT model.

The Frossling [124] vaporisation correlation is expressed by the following equation:

$$\frac{dr_0}{dt} = -\frac{\alpha_{spray} \rho_g D}{2 \rho_l r_0} B_d Sh_d \tag{3.60}$$

Where, r_0 is the undisturbed droplet radius; α_{spray} is the user-specified scaling factor for the mass transfer coefficient; D s the mass diffusivity of liquid vapor in air; Sh_d is the Sherwood number.

B_d is defined as

$$B_d = \frac{\Upsilon_1^* - \Upsilon_1}{1 - \Upsilon_1^*} \tag{3.61}$$

Where, Υ_1^* is the vapor mass fraction at the drop's surface, Υ_1 is the vapor mass fraction.

(3) Combustion model

The SAGE solver [125], which models detailed chemical kinetics via a set of CHEMKIN-formatted input files, was selected to simulate the combustion of the dual fuel engine. SAGE calculates the reaction rates for each elementary reaction while the CFD solver solves the transport equations. The mechanism of the multi-step chemical reaction [132] can be described by Eq (3.62).

$$\sum_{m=1}^{M} v'_{m,r} \chi_m \Leftrightarrow \sum_{m=1}^{M} v''_{m,r} \chi_m \qquad \text{for } r = 1, 2, ...R \tag{3.62}$$

Where, $v'_{m,r}$ and $v''_{m,r}$ are the stoichiometric coefficients for the reactants and products, respectively, for species *m* and reaction *r*; *R* is the total number of reactions; χ_m *is* the chemical symbol for species *m*.

The net production rate of species *m* is given the following equation.

$$\dot{\omega}_m = \sum_{r=1}^{R} v_{m,r} q_r \quad \text{for } m = 1, 2, \ldots M \tag{3.63}$$

Where, *M* is the total number of species.

The rate-of-progress parameter *q*, for the r^{th} reaction is given by Eq (3.64).

$$q_r = k_{fr} \prod_{m=1}^{M} [X_m]^{v'_{m,r}} - k_{rr} \prod_{m=1}^{M} [X_m]^{v''_{m,r}} \tag{3.64}$$

Where, $[X_m]$ is the molar concentration of species *m*; k_{fr} and k_{fr} are the forward and reverse rate coefficients for reaction *r*.

With the above information, the governing equations for mass and energy conservation can be solved for a given computational cell. The following governing equation expresses the mass conservation:

$$\frac{d[X_m]}{dt} = \dot{\omega}_m \tag{3.65}$$

The governing equation for energy conservation is the following:

$$\frac{dT}{dt} = \frac{V \frac{dP}{dt} - \sum_m (\bar{h}_m \dot{\omega}_m)}{\sum_m ([X_m] \bar{c}_{p,m})} \tag{3.66}$$

Where, $\bar{h}_m$ is the molar specific enthalpy; $\bar{c}_{p,m}$ is the molar specific heat at constant pressure.

(4) Turbulence model

As turbulence significantly affects the mixing rate of momentum, energy and species, a turbulence model must be included to attain accurate CFD simulation results. The Renormalisation Group (RNG) *k*-*ε* turbulence model [127], which shows better performance in characterising anisotropic and non-equilibrium effect than the standard *k*-*ε* turbulence model, is employed to modelling the in-cylinder turbulence. The transport equation of turbulent kinetic energy *k* and the dissipation of turbulent kinetic energy *ε* are given by Eq (3.67) and Eq (3.68).

$$\frac{\partial \rho k}{\partial t}+\frac{\partial \rho u_i k}{\partial x_i}=\tau_{ij}\frac{\partial u_i}{\partial x_i}+\frac{\partial}{\partial x_j}\frac{\mu+\mu_t}{P_{r_k}}\frac{\partial k}{\partial x_j}-\rho\varepsilon+\frac{C_S}{1.5}S_S \tag{3.67}$$

$$\frac{\partial \rho \varepsilon}{\partial t}+\frac{\partial\left(\rho u_i \varepsilon\right)}{\partial x_i}=\frac{\partial}{\partial x_j}\left(\frac{\mu+\mu_t}{P_{r_\varepsilon}}\frac{\partial \varepsilon}{\partial x_j}\right)+C_{\varepsilon 3}\rho\varepsilon\frac{\partial u_i}{\partial x_i}+\left(C_{\varepsilon 1}\frac{\partial u_i}{\partial x_j}\tau_{ij}-C_{\varepsilon 2}\rho\varepsilon+C_S S_S\right)\frac{\varepsilon}{k}+S-\rho R \tag{3.68}$$

Where, u_i represent flow variables (e.g., velocity). τ_{ij} *is* the Reynolds stress. μ_t is the turbulent viscosity. *Pr* is the Prandtl constant. *S* is the user-supplied source term and S_s is the source term that represents interactions with discrete phase (spray). The $C_{\varepsilon i}$ terms are model constants that account for compression and expansion.

For the RNG *k*-*ε* model, *R* is defined as

$$R=\frac{C_\mu \eta^3\left(1-\eta/\eta_0\right)\varepsilon^2}{\left(1+\beta\eta^3\right)k} \tag{3.69}$$

$$\eta_0=\sqrt{\frac{C_{\varepsilon_1}\text{-}1}{C_\mu\left(C_{\varepsilon_1}\text{-}1\right)}} \tag{3.70}$$

Where, C_μ is a model constant that can be tuned for a particular flow. $\beta = 0.012$.

The expression for η is

$$\eta=\frac{k}{\varepsilon}\sqrt{2S_{ij}S_{ij}} \tag{3.71}$$

Where, S_{ij} is the mean strain rate tensor.

3.4.2 Calculation flowchart

Figure 3.5 shows the calculation flowchart of 3D model developed in the CONVEGE software. As seen from Figure 3.5, the calculation starts with the initialisation of the mesh and boundary conditions, then the thermodynamic properties of the initial species are loaded. After completing the fluid field calculation, the temperature is used to determine whether the combustion starts. In the present study, when the calculated temperature is higher than the threshold value (600 K), the physical fluid process starts to couple with the chemical reaction process. The thermodynamic and species data are transferred to the CHEMKIN-based library, which returns the chemical reaction rates. After the combustion resource is updated, there will be the mesh regeneration and results output. When the calculated temperature is lower than 600 K, the calculation flow jumps directly to the mesh regeneration and results output. If the iteration is not yet finished, the calculation flow returns to the fluid flow calculation at next simulation step, otherwise the calculation flow ends.

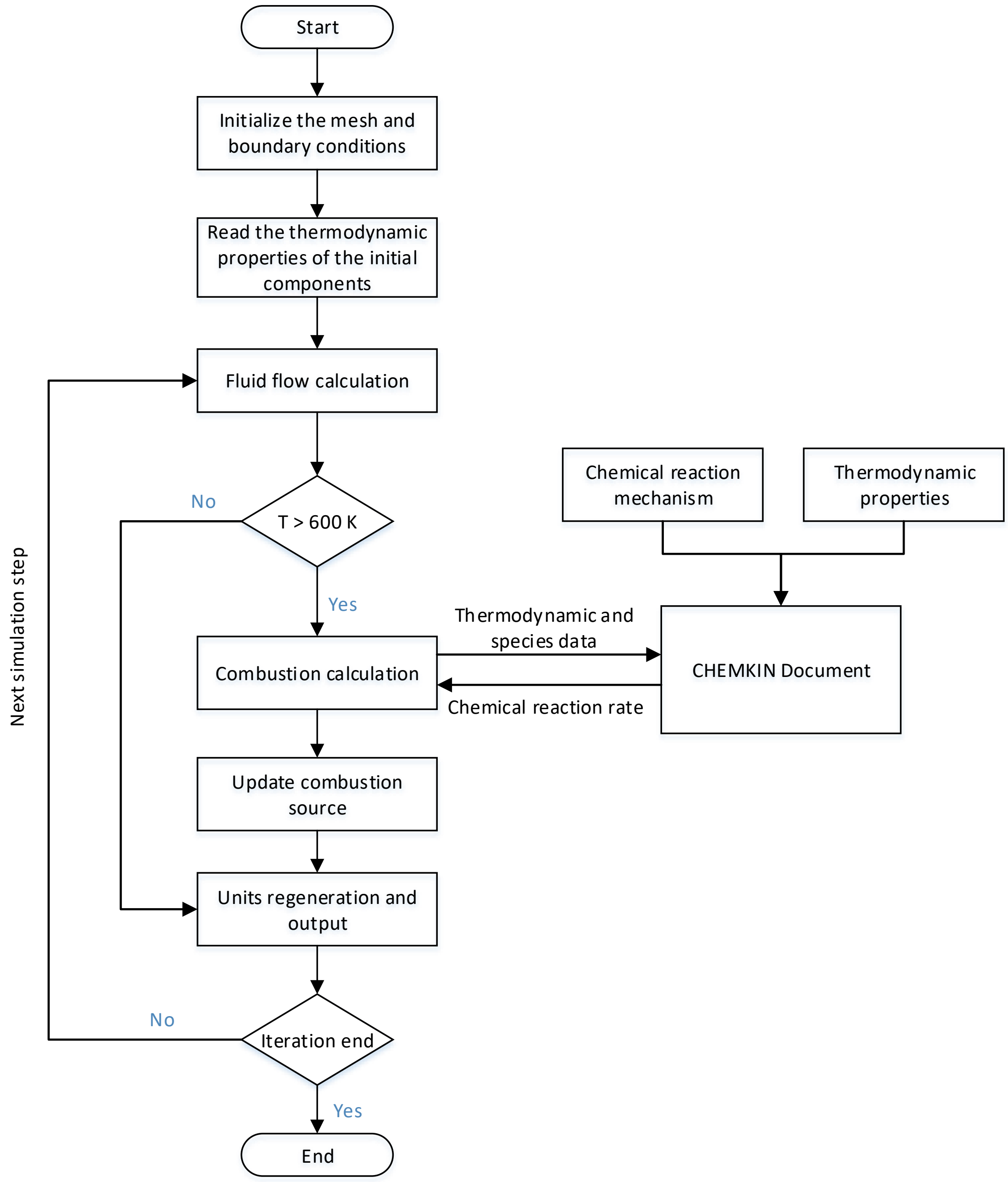

Figure 3.5 Calculation flowchart of the developed 3D simulation model in CONVERGE

3.5 Combustion model calibration

In this study, three methods including the Wiebe combustion model, CFD simulation model and engine experiment are employed to analyse the heat release rate of marine dual fuel engines. The Wiebe combustion model is used for simulating HRR of the proposed 0D/1D simulation model for operating setting optimisation, whilst the CFD simulation model is employed to produce HRR for calibrating the Wiebe combustion model. However, the accuracy of the proposed CFD model must be verified first by using the HRR obtained from engine experiment. Thus, the first step of combustion model calibration is calculating HRR from the measured in-cylinder pressure.

3.5.1 Heat release calculation

Heat release rate (HRR) analysis is an efficient way to obtain the combustion information inside the engine cylinders, which can be used for calibrating the combustion model in engine simulation and modelling. The HRR is defined as the rate at which the chemical energy of the fuel is released during the combustion process [47]. However, there are many different ways to formalise HRR depending on the consideration of heat loss or normalisation. The three definitions used in this study are the following:

(a) Net Apparent Heat Release Rate (NAHRR):

$$NAHRR = \dot{Q}_{\mathrm{comb}} - \dot{Q}_{\mathrm{loss}} + \dot{E}_f = m \cdot c_v \cdot \frac{dT}{dt} + p \cdot \frac{dV}{dt} \tag{3.72}$$

(b) Gross Apparent Heat Release Rate (GAHRR):

$$GAHRR = \dot{Q}_{comb} + \dot{E}_f = m \cdot c_v \cdot \frac{dT}{dt} + p \cdot \frac{dV}{dt} + \dot{Q}_{\mathrm{loss}} \tag{3.73}$$

(C) Combustion Reaction Rate (CRR):

$$CRR = \xi = \frac{m \cdot c_v \cdot \frac{dT}{dt} + p \cdot \frac{dV}{dt} + \dot{Q}_{\mathrm{loss}}}{u_{\mathrm{comb}}} \tag{3.74}$$

Where, $\dot{Q}_{comb}$ is the energy release rate caused by the fuel combustion; $\dot{Q}_{loss}$ is the heat loss rate from the in-cylinder gas to cylinder walls; $\dot{E}_f$ is the energy absorption rate caused by pilot diesel evaporation.

Figure 3.6 shows the calculation flowchart of the heat release calculation for dual fuel engines. The measured in-cylinder pressure against the crank angle is the primary input of the calculation, whilst the reaction coordinate (RCO) is the main output. The other parameters, like the volume, temperature, mass, composition, gas properties and others, are calculated by using the same way presented in Figure 3.3. In addition, it is assumed that the natural gas and diesel fuels burn proportionally according to their total injection mass ratio, as natural gas contributes around 90% of the total energy input and thus dominates the combustion process.

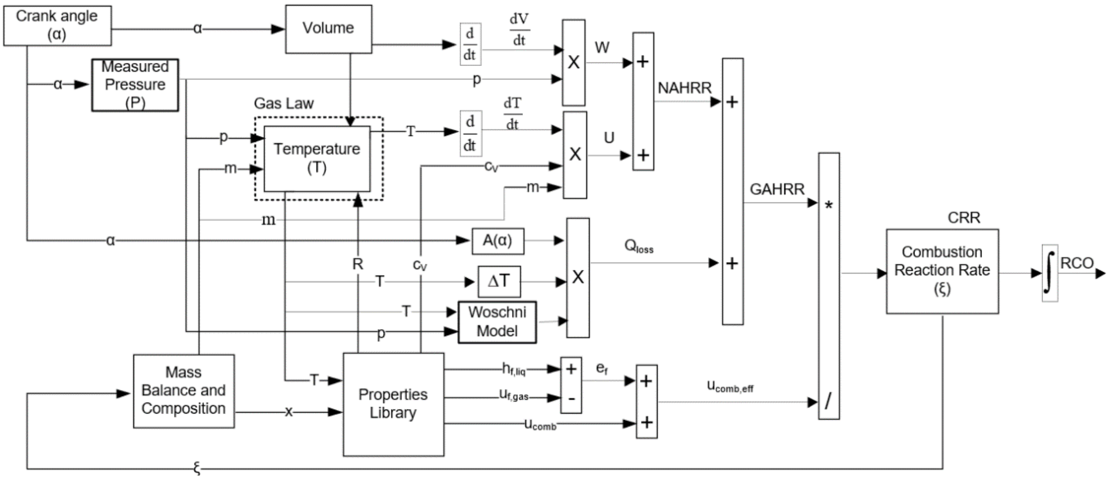

Figure 3.6 Calculation flowchart of the heat release calculation for dual fuel engines

3.5.2 Wiebe combustion parameters determining and fitting

DF engines, which employ a small amount of pilot fuel to ignite the gaseous fuel, exhibit characteristics of both the diffusion combustion and the premixed combustion, and therefore require more complex models rather than a single Wiebe function. As reported in pertinent literature [94, 117], combustion models based on two or three Wiebe functions exhibited sufficient accuracy for predicting the burned mass fraction, heat release rate and in-cylinder pressure of DF engines. The model can be developed into a widely applicable model if enough experimental data or CFD simulations are available to find the unique set (or sets) of parameters that minimise the error at most conditions. Hence, a multiple Wiebe function as described by Eq (3.75) is used in this study to represent the combustion of the investigated DF engine.

$$\frac{dQ}{d\varphi}=\sum_{i=1,2,3} Q_T\cdot b_i\cdot\frac{6.9\cdot\left(m_{v,i}+1\right)}{\Delta\varphi_i}\cdot\left(\frac{\varphi-\varphi_i}{\Delta\varphi_i}\right)^{m_{v,i}}\cdot\exp\left[-6.9\cdot\left(\frac{\varphi-\varphi_i}{\Delta\varphi_i}\right)^{m_{v,i}+1}\right] \tag{3.75}$$

Where, b_i is the weight factor of each Wiebe function. $m_{v,\mathrm{i}}$ is the shape factor of each combustion stage. φ_i is the start of each combustion stage. $\Delta\varphi_\mathrm{i}$ is the duration of each combustion stage.

After obtaining HRR from measured in-cylinder pressure by using HRR calculation or from CFD simulation result, the Fit function in MATLAB environment is used to fit the Wiebe combustion parameters according to the following steps:

1. Identify the number of Wiebe combustion parameters that need to be determined when Double-Wiebe or Triple-Wiebe function is employed for characterising the combustion of reference engine;

2. Determine the lower limit, upper limit and initial values of Wiebe combustion parameters by referring to literature review [81, 133] and Bilcan's schematic algorithm [97];
3. Compare the fitting results of Double-Wiebe function and Triple-Wiebe function with experimentally obtained HRR and in-cylinder pressure, deciding which Wiebe function will be employed in this study;
4. Select operating settings (such as pilot injection timing, equivalence ratio and NG mass) as the controlling (independent) parameters of each Wiebe combustion parameters;
5. Use Response Surface Methodology (RSM) to obtain the Wiebe parameter correlations of selected operating settings by using Linear and Quadratic response models;
6. Compare the HRR and pressure simulated by using Linear and Quadratic response models, deciding which response model will be used for combustion model calibration considering the balance between accuracy and complexity.

Table 3.3 Wiebe parameters determining method of a Triple-Wiebe function

Wiebe	Parameter	Marker	Determining method
1th	φ_1	✓	Start of the entire combustion process
	$\Delta\varphi_1$	O	Approximated by using Bilcan's schematic algorithm [97]
	b_1	O	Estimated by using Watson et al. [134]
	m_1	×	Fitting function
2nd	φ_2	✓	Same with φ_1, start of the entire combustion process
	$\Delta\varphi_2$	×	The second combustion stage ends after the peak HRR position and before the end of the entire combustion process
	b_2	✓	Calculated by one minus b_1 and b_3
	m_2	×	Fitting function
3rd	φ_3	✓	Same with φ_1, start of the entire combustion process
	$\Delta\varphi_3$	✓	End of the entire combustion process
	b_3	×	Fitting function
	m_3	×	Fitting function

Comments: ✓ represent low uncertainty (5 parameters); O represents medium uncertainty (2 parameters); × represent high uncertainty (5 parameters).

Eight parameters need to be determined when a Double-Wiebe function is employed for characterising DF engine combustion, whilst twelve parameters are used with a Triple-Wiebe function. Table 3.3 shows the Wiebe parameter determining method of a

Triple-Wiebe function with markers representing three uncertainty levels. The Wiebe parameter determining method of a Double-Wiebe function can refer to the first and second Wiebe function in Table 3.3. When a Triple-Wiebe function is used, there are 12 parameters need to be determined, including 5 low-uncertainty parameters ($\varphi_1, \varphi_2, \varphi_3, \Delta\varphi_3$ and b_2), 2 medium-uncertainty parameters ($\Delta\varphi_1$, b_1) and 5 high-uncertainty parameters ($m_1, m_2, m_3, \Delta\varphi_2$ and b_3). Low-uncertainty represents the parameter can be determined by using the HRR analysis, whilst medium-uncertainty means the parameters are estimated by employing empirical formulae. High-uncertainty parameters can only be obtained by using the abovementioned Fitting function in MATLAB environment.

By assuming the SOCs of each Wiebe function start at the same time, φ_1, φ_2 and φ_3 are fixed at the start of combustion (SOC). $\Delta\varphi_3$ is the combustion duration of the third Wiebe function, which can be represented by the interval between the end of combustion (EOC) and the SOC. In this study, the SOC and EOC are defined as the crank angles corresponding to 1% and 99% of the total heat release, respectively, which can be obtained from the integrated HRR curve. Weigh factor b_2 can be calculated after b_1 and b_3 are known based on the principle that the sum of b_1, b_2 and b_3 equals to one. Watson et al. [134] proposed a function of ignition delay and equivalence ratio to estimate the premixed fraction b_1 of a direct injection diesel engine, which could be calibrated for estimating b_1 for DF engines by using experiment data. Another medium-uncertainty parameter $\Delta\varphi_1$ can be approximated by using the schematic algorithm proposed by Bilcan's [97] (presented in APPENDIX A). The rest five high-uncertainty parameters ($m_1, m_2, m_3, \Delta\varphi_2$ and b_3) will be determined by using the Fitting function in MATLAB environment. The variation ranges of the employed Wiebe combustion parameters can refer to literature [81, 133], which helps the Fitting function converge faster. The optimal combination of Wiebe parameters will be found by using the least square regression to minimising the error between the predicted and calculated HRR. The error is defined for each combustion phase according to the following equation:

$$\varepsilon^k = \frac{\int_{\varphi_S}^{\varphi_e \left(\frac{dQ_p^k}{d\varphi}(\varphi) - \frac{dQ_m^k}{d\varphi}(\varphi) \right)^2} d\varphi}{\int_{\varphi_S}^{\varphi_e \left(\frac{dQ_m^k}{d\varphi}(\varphi) \right)^2 d\varphi} 100} \tag{3.76}$$

Where, ε^k is the error in %, φ_s and φ_e represent the start and end crank angle of each combustion phase, dQ_p and dQ_m are predicted and calculated HRR.

After obtaining the Wiebe combustion parameters, the Response Surface Methodology (RSM) [72] is used to calibrate the combustion model, which assumes that the Wiebe combustion parameters are hypothetically affected by the engine operating settings like pilot injection timing, equivalence ratio and NG mass. The Wiebe combustion parameters are considered as responses whilst the engine operating settings are called independent variables or factors. An empirical statistical model is developed to provide an approximation for correlating the factors to the responses. In this study, a linear response model and a quadratic response model are compared to in terms of the computational cost and prediction accuracy. The equations of the linear response model and quadratic response model are shown as Eq (3.77) and Eq (3.78).

Linear response model:

$$y = a \cdot x_1 + b \cdot x_2 + c \cdot x_3 + C \tag{3.77}$$

Quadratic response model:

$$y = a \cdot x_1 + b \cdot x_2 + c \cdot x_3 + d \cdot x_1 \cdot x_2 + e \cdot x_1 \cdot x_3 + f \cdot x_2 \cdot x_3 + g \cdot x_1^2 + h \cdot x_2^2 + i \cdot x_3^2 + C \tag{3.78}$$

Where, y represents the Wiebe combustion parameters (SOC, b_i, $\Delta\varphi_\mathrm{i}$ and m_i); x_1 is the pilot injection timing; x_2 is the equivalence ratio variation; x_3 is the NG mass variation.

3.6 Multi objective optimisation

3.6.1 Multi objective optimisation and PARETO optimal solution

Optimisation is defined as an act, process or methodology of making something (such as a design, system or decision) as fully perfect, functional, or effective as possible. The mathematical procedure is to find the optimal variables which generates the maximum or minimum of a predefined objective function. However, practical engineering optimisation problems usually have multiple conflicting objectives, which means the derived solution may optimise one objective function but also cause undesired changes to other objective functions. This kind of optimisation tasks is called Multi-Objective Optimisation (MOP) [135], which can be defined as the follow equation:

$$\begin{cases} \text{Max/ Min}\left[f_1(X), f_2(X), \cdots, f_n(X) \right] \\ s.t. \\ g_j(X) \leq 0, j = 1, 2, \cdots J \\ h_k(X) = 0, k = 1, 2, \cdots K \end{cases} \tag{3.79}$$

Where, $X = (x_1, x_2, \dots x_p)$ is a p-dimensional vector representing the variables; $f_i(X)$ is objective function, $i = 1, 2, \dots$ n; $g_j(X) \leqslant 0$ and $h_k(X) = 0$ are the constrain functions.

For single-objective optimisation, the derived optimal solution is usually the global maximum or minimum, which is also called the global optimal solution and supposed to outperform all the rest solutions. For multi-objective optimisation, especially when the objectives conflict with each other, it is challenging to find a solution to optimise all the objective functions simultaneously. Thus, the Pareto front is introduced to solve this kind of conflicting multi-objective optimisation problems.

Before defining the Pareto front, the concept of dominance must be explained first. The dominance relationship in a minimisation problem is defined as follow: for any two decision variables $\bar{X}_u, \bar{X}_v \subseteq U$, if and only if for all the cases $\forall i \subseteq \{1, 2, \cdots n\}$, the objective functions meet the relationship $f_i\left(\bar{X}_u\right) < f_i\left(\bar{X}_v\right)$, then $\bar{X}_u$ dominates $\bar{X}_v$; if and only if for all the cases $\forall i \subseteq \{1, 2, \cdots n\}$, the objective functions meet the relationship $f_i\left(\bar{X}_u\right) \leq f_i\left(\bar{X}_v\right)$. And at least there exists $j \in \{1, 2, \cdots, n\}$ making $f_j\left(\bar{X}_u\right) < f_j\left(\bar{X}_v\right)$, then $\bar{X}_u$ weakly dominates $\bar{X}_v$; if and only if there exists $i \in \{1, 2, \cdots, n\}$ making $f_i\left(\bar{X}_u\right) < f_i\left(\bar{X}_v\right)$, at the same time, there exists $j \in \{1, 2, \cdots, n\}$ making $f_i\left(\bar{X}_u\right) > f_i\left(\bar{X}_v\right)$, then there is no dominance relationship between $\bar{X}_u$ and $\bar{X}_v$.

The Pareto front is defined as the set of Pareto optimal solutions (or nondominated solutions) which are not dominated by any other solutions. In addition, the solutions in the Pareto front cannot be improved for one objective function without worsening the other ones. Taking minimisation MOP problems as example, a solution $\bar{X}_v$ is in the Pareto front if and only if $\bar{X}_v$ is not dominated by any other decision variables. In other word, there is no decision variable $\bar{X}_u$ meeting the flowing equation:

$$\forall i \subseteq \{1, 2, \cdots n\}, f_i\left(\bar{X}_u\right) \leq f_i\left(\bar{X}_v\right) \wedge \exists j \in \{1, 2, \cdots n\}, f_j\left(\bar{X}_u\right) < f_j\left(\bar{X}_v\right) \tag{3.80}$$

3.6.2 Nondominated sorting genetic algorithm II

Genetic algorithms, which is inspired by natural selection process using biologically operators such as mutation, crossover and selection to generate high-quality solutions

[63], have been widely used for solving multi-objective optimisation and searching problems [58, 64]. In this study, the Nondominated Sorting Genetic Algorithm II (NSGA II) [69] will be used for optimising the operating settings of marine DF engines because of its prominent searching ability, fast convergence and high robustness. NSGA II employs the Pareto ranking method for selecting individuals in each generation and uses the crowding distance as the following selection criterion to guarantee the even distribution of Pareto solutions. The crowding distance is defined as the distance from an individual to its nearest neighbour. Figure 3.7 presents the calculation flowchart of NSGA II, which can be explained by the following steps:

1. An initial population of the individuals (parent generation P_i) is generated randomly by converting the real number which representing decision variables to binary number. The Pareto ranking method will be employed to select the individuals until all the individuals are placed in different Pareto fronts with different rankings. In addition, the crowding distance between individuals in the same Pareto rankings will be calculated;
2. The new generation of individuals (child generation C_i) will be produced by using selection, crossover and mutation operators while referring to the Pareto rankings and crowding distance;
3. In order to extend the searching space, elitist strategy will be used to merge the parent and child generations. Then Pareto ranking, crowding distance calculation and population trim are performed to produce the new generation $P_{\mathrm{i+1}}$.
4. After each new generation is produced, it will be checked whether the maximum evolutionary generation has been reached. If the answer is no, the abovementioned 3 steps will be repeated. Otherwise, the calculation flow stops and outputs the optimal Pareto solutions.

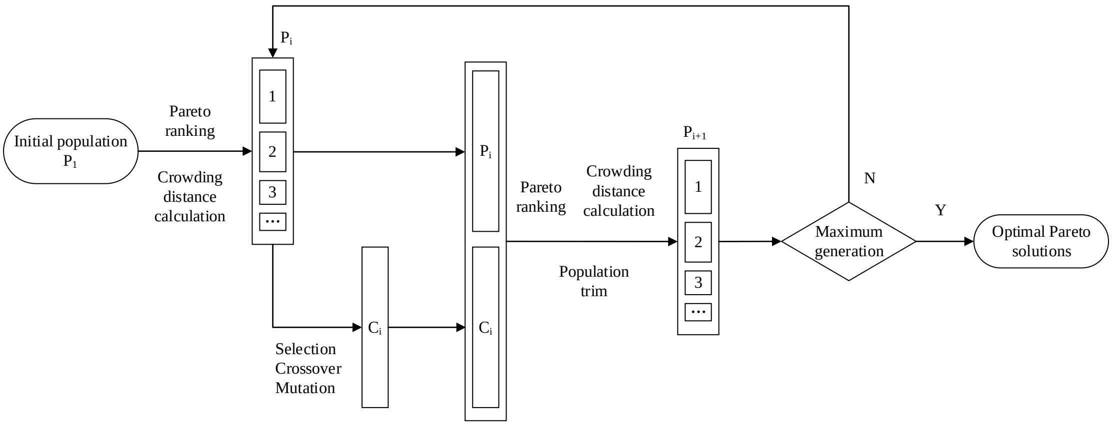

Figure 3.7 Calculation flowchart of NSGA II

The selection of excellent individuals in each generation is based on the Pareto ranking method and the crowding distance. Before executing the selection operator, the Pareto ranking of two individuals is compared. If their Pareto rankings are different, the individual with smaller ranking is selected and transferred to next generation. Otherwise, the individual with larger crowding distance is selected. The combination of the Pareto ranking method and crowding distance guarantee high-resolution and evenly distributed Pareto front, which improve the calculation speed and robust of the NSGA II algorithm.

3.7 Chapter summary

The modelling principles, calculation flowchart and model development of the proposed 3D and 0D/1D models for simulating marine DF engines were first introduced. Then, the combustion model calibration process is described, including heat release calculation from in-cylinder pressure, Wiebe combustion parameters determining and fitting. Finally, the concept of multi objective optimization, Pareto optimal solutions and Nondominated Sorting Genetic Algorithm II are illustrated.

Chapter 4. Experiment setup and case studies

4.1 Chapter outline

Before developing the simulation models, characteristics of the reference engine are introduced firstly. Then, testing of the investigated marine DF engine is conducted under the working conditions of propulsion characteristic curve for model validation. Finally, simulation case studies are designed with regard to addressing the research gaps identified in the critical review.

4.2 Engine characteristics and experiment setup

4.2.1 Engine characteristics

The investigated YC6K dual fuel engine (as shown in Figure 4.1) was converted from YC6K diesel engine by adding a natural gas supply system and updating its Electronic Control Unit (ECU). It operates in two different modes, the diesel mode and dual-fuel mode. Diesel fuel with lower auto-ignition temperature serves as an ignition source for the natural gas combustion. The diesel fuel contributes to around 10% of the total energy release in dual-fuel mode at the nominal working condition. The main characteristics of the YC6K dual-fuel engine are shown in Table 4.1.

Figure 4.1 YC6K DF engine testbed

Table 4.1 Main characteristics of YC6K DF engine

Parameter	Unit	
Bore	mm	129
Stroke	mm	155
Nominal Engine Speed	Rpm	1800
Nominal power per cylinder	kW	65
Compression Ratio	-	16.5:1
Inlet valve close	°CA, ABDC	2
Exhaust valve open	°CA, BBDC	31

The compressor and turbine maps are important inputs of the proposed 0D/1D simulation model, as shown in Figure 4.2. Since only limited points are provided by the original turbocharger map, surface fitting techniques are used prior to using the maps to the turbocharger sub-model. The Griddata and Gridfit functions provided by MATLAB are comparatively used to fit the turbine mass flow in Figure 4.3. Case π_t = 2.6 is taken as the validation case whilst the others are used as the surface fitting inputs. As observed from Figure 4.3, the surface obtained by Gridfit function shows much higher accuracy with a correlation coefficient of 0.999 than the surface obtained by Griddata function with a correlation coefficient of 0.810. Thus, the Gridfit function is used for fitting the characteristics surface of the compressor mass flow, compressor efficiency, turbine mass flow and turbine efficiency, as show in Figure 4.4.

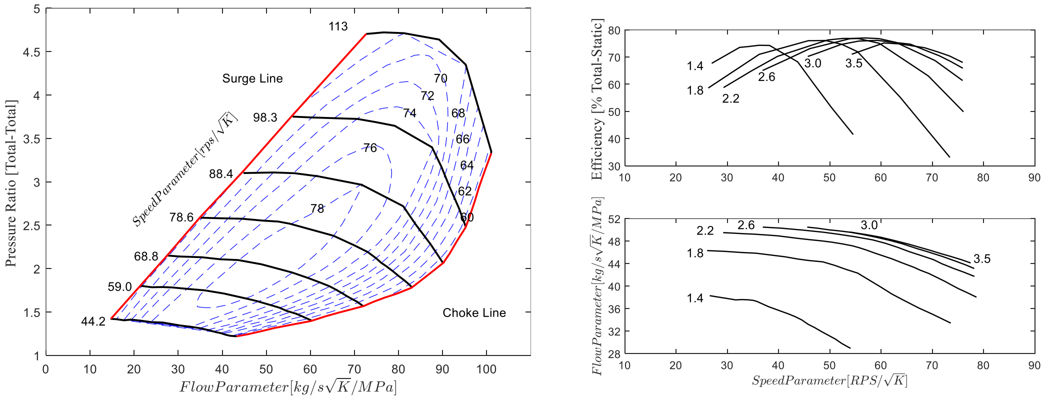

(a) Compressor MAP

(b) Turbine MAP

Figure 4.2 The original maps of the employed compressor and turbine

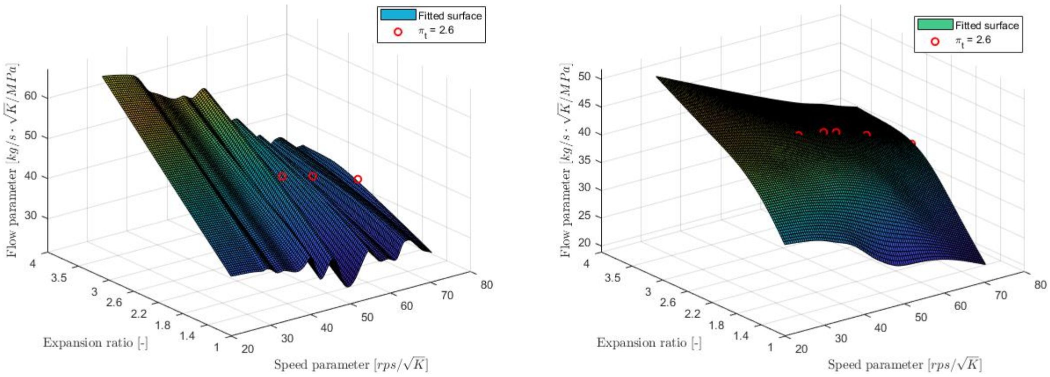

(a) Surface fitting by using Griddata function (b) Surface fitting by using Gridfit function

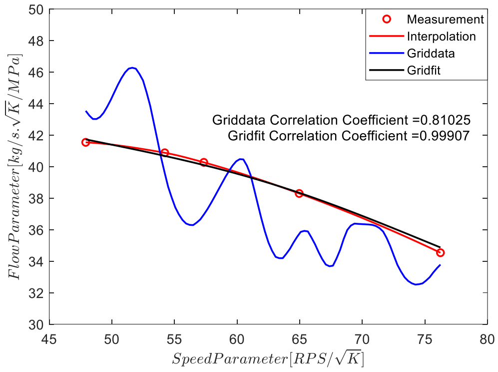

(c) Correlation coefficients comparison ($\pi_t = 2.6$)

Figure 4.3 Turbine mass flow validation by using the Griddata and Gridfit functions

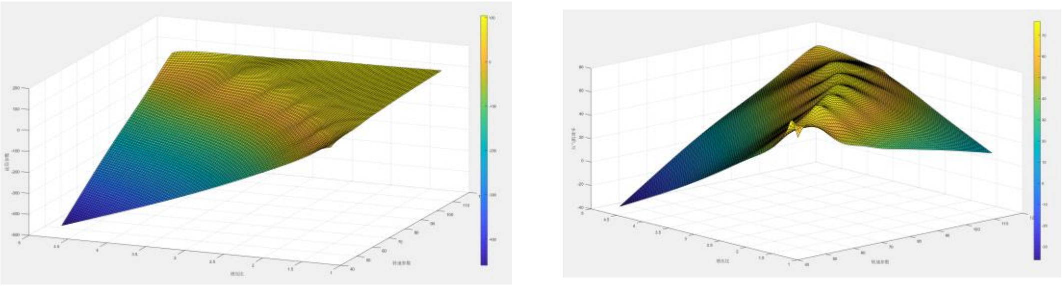

(a) Compressor mass flow (b) Compressor efficiency

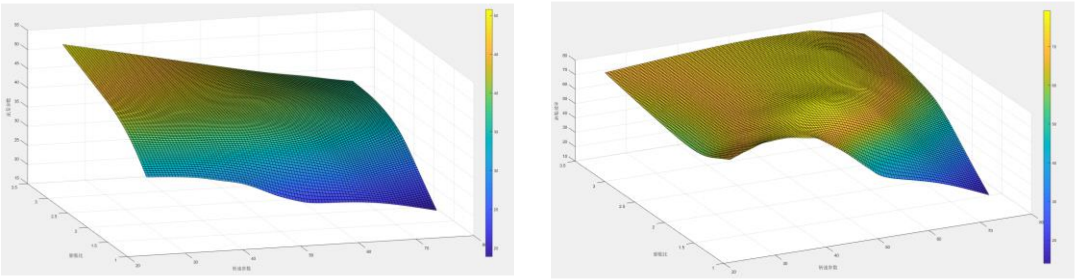

(c) Turbine mass flow (d) Turbine efficiency

Figure 4.4 The fitted turbocharger characteristic surface

4.2.2 Experiment setup

The experimentally measured parameters for the investigated engine include in-cylinder pressure, fuel mass flow rate, inlet air mass flow rate, inlet/exhaust manifold pressure and emissions. Heat release rate (HRR) will be calculated based on the measured in-cylinder pressure. The technical specifications of the employed sensors are shown in Table 4.2. Figure 4.5 presents the sensor layout of YC6K DF engine testbed. Three flow meters are used to measure the mass flow rate of the pilot diesel fuel (AVL 735C), the natural gas (E+H 83F25-XRW2/0) and the inlet air (ABB FMT 700). A piezoelectric in-cylinder pressure sensor (AVL GU22CK) is installed on the cylinder head to obtain the in-cylinder pressure diagram, which is then transferred to the combustion analyser (KiBox To Go 2893) for heat release analysis. The emissions analyser (AVL AMA i60 R1) receives exhaust gas samples from the gas sampling device and provides the concentrations of various exhaust gas species including NOx, CO and HC. A low-pressure indicating sensor (LP11DA) is used to measure the exhaust pressure at the exhaust gas manifold upstream turbine.

Table 4.2 Employed sensors specifications

Equipment	Type	Measured Error/ Uncertainty/Linearity
In-cylinder pressure sensor	AVL GU22CK [136]	≤ ±0.3%
Combustion analyser	KiBox To Go 2893 [137]	Approx. 5 ms (<< 1 combustion cycle)
Diesel consumption meter	AVL 735C [138]	≤ 0.12%
Gas consumption meter	E+H 83F25-XRW2/0 [139]	≤±0.05
Air-mass flow meter	ABB FMT 700 [140]	≤ 0.8%
Exhaust pressure sensor	AVL LP11DA [141]	≤ ±0.1%
Emission analyser	AVL AMA i60 R1 [142]	≤ ±2%

A natural gas chromatographic analyser [143] is used to measure the composition of the employed compressed natural gas (CNG), as shown in Table 4.3. The Lower Heating Value (LHV) of the employed natural gas is 47.18 MJ/kg. The diesel fuel used in the DF engine testing was the light fuel of grades 0# [144]. The diesel LHV is 42.652 MJ/kg, whilst its Cetane Number is 50. Table 4.4 shows the operating parameters under six working conditions of the propulsion characteristic curve.

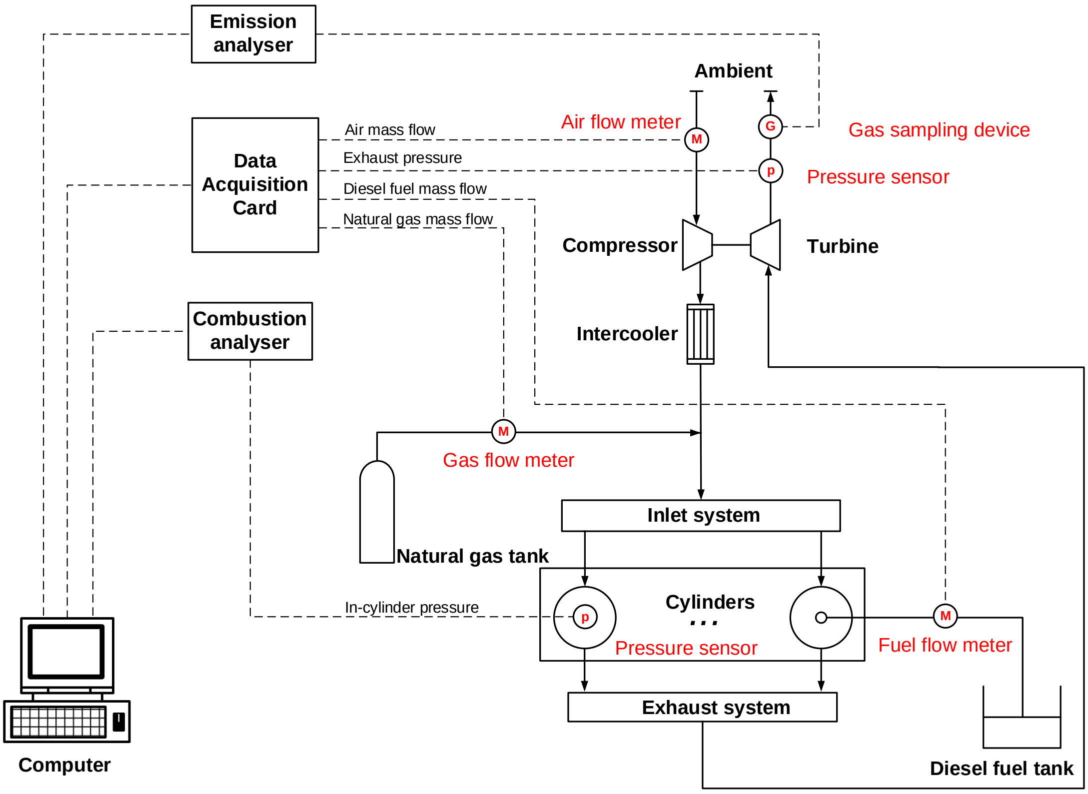

Figure 4.5 Sensor layout of YC6K DF engine test bed

Table 4.3 Compositions of the employed natural gas

Compositions	Volumetric fraction (%)
CH_4	86.37
C_2H_6	3.67
C_3H_8	0.02
n-C_4H_{10}	0.01
CO_2	4.70
N_2	2.55
CO	2.68

Table 4.4 Operating parameters under 6 working conditions of the propulsion characteristic curve

Operation load	%	32	42	53	74	85	100
Power	kW	95	127	159	222	254	300
Rotational speed	rpm	1228	1352	1457	1629	1703	1800
Intake manifold pressure	bar	1.48	1.79	2.11	2.69	2.80	2.91
Intake manifold temperature	°C	24	26	29	35	37	38
Pilot injection timing	°CA	–5	–5	–5	–5	–5	–5
Maximum pilot injection pressure	bar	800	800	800	800	800	800
Pilot diesel mass flow	kg/h	3.75	4.15	4.62	5.33	5.58	5.91
Natural gas mass flow	kg/h	17.89	25.53	32.90	47.89	53.03	59.47
Air mass flow	kg/h	659	860	1098	1542	1664	1783

For dual fuel engines, the equivalent fuel consumption rate [145] is defined as converting the consumption rate of the two employed fuels (diesel and natural gas) into that of natural gas according to the principle of equivalent calorific value.

$$\dot{m}_{fuel} = \frac{\dot{m}_d \cdot LHV_d + \dot{m}_{NG} \cdot LHV_{NG}}{LHV_{NG}} \tag{4.1}$$

Where, $\dot{m}_{fuel}$ is the equivalent fuel consumption rate in kg/h. $\dot{m}_d$ and $\dot{m}_{NG}$ are the consumption rates of pilot diesel and natural gas in kg/h, respectively. LHV_d and LHV_{NG} are the Lower Heating Values (*LHV*) of pilot diesel and natural gas in J/kg, respectively.

As there are two fuels (diesel and natural gas) involved in the combustion of dual-fuel engines, the total air−fuel equivalence ratio λ_t is defined according to the following equation:

$$\lambda_t = \frac{\dot{m}_{air}}{\dot{m}_d \cdot AFR_{d,0} + \dot{m}_{NG} \cdot AFR_{NG,0}} \tag{4.2}$$

Where, $AFR_{d,0}$ and $AFR_{NG,0}$ are the stoichiometric air-fuel ratio of diesel and natural gas, respectively.

4.3 Case studies

The aforementioned engine characteristics and experiment design are used for developing the proposed two simulation models and validating the model accuracy. Then the validated simulation models will be employed to conduct the case studies with regard to addressing the research gaps derived from the critical literature review. The designed case studies in this thesis include parametric investigation using 3D simulation model, Wiebe combustion model calibration and engine operating settings optimisation.

4.3.1 Parametric investigation using 3D simulation model

The prediction accuracy of the proposed 0D/1D simulation model is primarily affected by Wiebe combustion model, which needs to be calibrated by using experimental data. However, conducting an engine test with different operating settings could be both time-consuming and costly. A computational fluid dynamics (CFD) tool, which considers the detailed physical and chemical process as well as the in-cylinder space distribution, can be used as a virtual engine to produce HRR for calibrating 0D combustion model. For the first case study, a 3D simulation model developed with the CONVERGE software will be used to investigate the effects of each selected operating setting on the engine performance, emissions and knocking occurrence at 100% operation load. Furthermore, a parametric run will be performed to obtain the HRR for calibrating Wiebe combustion model at three operation conditions covering medium and high operation loads. Simulation results of the parametric run will also be analysed to explore the potential engine settings that could provide a simultaneous reduction of BSFC and NOx emission whilst avoiding knocking occurrence.

(1) Effects investigation at 100% operation load

In this part, the pilot injection timing, equivalence ratio and natural gas mass are selected for an effect investigation on the engine performance, emissions and knocking occurrence of the investigated dual fuel engine at 100% operation load. As the NG-air mixture is ignited by pilot diesel in DF engines, the pilot injection timing plays an important role in determining the start of combustion and the following combustion process [146], thus affecting the engine performance and emissions significantly. Equivalence ratio proves to be an influencing factor for DF engine combustion characteristics including peak heat release and combustion duration, which subsequently affect the BSFC and emissions [147]. Natural gas mass, which has a direct impact on the input energy, NG-diesel mass ratio and in-cylinder gas properties [148], is also included in the effect investigation.

The variation levels of selected engine operating settings for individual effect investigation are presented in Table 4.5. Since the pilot injection timing at baseline case is –5°CA ATDC, the variation levels of pilot injection timing in Table 4.5 are set in advance to the baseline case (–15°, –12.5°, –10°, –7.5° and –5° ATDC) rather than equally distributed around the baseline case to avoid injection starting after the TDC. When the effect of pilot injection timing is individually investigated, the equivalence ratio variation and natural gas mass variation are kept at baseline values (0%).

Table 4.5 Operating settings of the effect investigation

Operating settings	Units	Levels				
Pilot injection timing	°CA	–15	–12.5	–10	–7.5	–5
Equivalence ratio variation	%	–10	–5	0	5	10
Natural gas mass variation	%	–10	–5	0	5	10

Five different equivalence ratio variations were investigated: –10%, –5%, 0%, 5% and 10% from the reference value while keeping the pilot fuel injection timing at –5 °CA ATDC and natural gas mass variation at 0%. The equivalence ratio was varied from –

10% to 10% with a constant NG mass by increasing the initial pressure at IVC from 2.83 bar to 3.45 bar and thus reducing the NG mass fraction from 3.56% to 2.91%, as presented in Table 4.6. It is worth mentioning that the total equivalence ratio of baseline case is 1.62 rather than the experimentally measured 1.92 because methane is used to represent natural gas in the proposed 3D simulation model.

Table 4.6 Equivalence ratio variation settings for the effect investigation

Input parameter	Unit	Levels				
Air-NG equivalence ratio variation	%	–10	–5	0	+5	+10
Air-NG equivalence ratio	-	1.58	1.67	1.76	1.85	1.94
Total equivalence ratio	-	1.46	1.55	1.62	1.72	1.90
Initial pressure	bar	2.83	2.98	3.14	3.30	3.45
NG mass fraction	%	3.56	3.37	3.20	3.05	2.91

Five different natural gas mass variation were investigated: –10%, –5%, 0%, 5% and 10% from the reference value while keeping the pilot fuel injection timing at –5 °CA ATDC and equivalence ratio variation at 0%. The NG mass variation was increased from –10% to 10% with a constant equivalence ratio by adjusting the initial pressure from 2.83 bar to 3.45 bar whilst keeping the initial NG mass fraction the same, as presented in Table 4.7.

Table 4.7 Natural gas mass variation settings for the effect investigation

Input parameters	Unit	Levels				
NG mass variation	%	–10	–5	0	5	10
NG injection mass	kg/h	53.52	56.50	59.47	62.44	65.42
Initial pressure	bar	2.83	2.98	3.14	3.30	3.45
NG mass fraction	%	3.20	3.20	3.20	3.20	3.20

(2) Parametric investigation at different operation loads

Before conducting the parametric run, the performance-emission trade-off at different operation loads (100%, 74% and 53%) was analysed to determine the variation ranges of the three operating settings. It is worth mentioning that the involvement of NG mass variation as one of the selected operating settings will cause an inevitable change to the engine output power, which means that the operation loads of the parametric run are not exactly kept at the abovementioned 100%, 74% and 53%. Thus, the corresponding constant rotational speeds 1800 r/min, 1629 r/min and 1457 r/min will be used in the following study to replace the 100%, 74% and 53% operation loads, respectively.

Subsequently, the parametric study was designed and performed with various combinations of the pilot injection timing, equivalence ratio variation and natural gas mass variation. Finally, the simulation results were presented and discussed to investigate the potential for a simultaneous reduction of NOx emissions and BSFC as well as avoiding knocking occurrence. At the same time, the simulated heat release rates were analysed to obtain the combustion characteristics, which would be used for Wiebe combustion model calibration in the following study.

4.3.2 Wiebe combustion model calibration

(1) Wiebe combustion parameters determining

As concluded in Section 2.3.2, two or three Wiebe functions are usually used to characterize the combustion of dual fuel engines. In order to reduce the computational cost of the engine setting optimisation, the minimum number of employed Wiebe functions that are sufficient for characterizing the DF engine combustion need to be determined before calibrating the combustion model. Thus, a comparison between double Wiebe function and triple Wiebe function are conducted considering the heat release rate and in-cylinder pressure. Finally, the determined Wiebe function was employed to obtain the Wiebe parameters of selected simulation cases at 1800 r/min, 1629 r/min and 1457 r/min operation conditions.

(2) Wiebe combustion parameters fitting

The Response Surface Methodology (RSM) [72] was used to fit the Wiebe combustion parameters which are considered as functions of pilot injection timing, equivalence ratio variation and NG mass variation. An empirical statistical model was developed to correlate the abovementioned engine operating settings to Wiebe combustion parameters. In addition, the in-cylinder pressure simulated by using linear response model and quadratic response model will be compared aiming at a compromise between the model complexity and prediction accuracy. Finally, the determined response model was employed to obtain the correlations of Wiebe combustion parameters (SOC, b_i, m_i and $\Delta\varphi_i$).

4.3.3 Engine operating settings optimisation

In order to improve the engine performance and simultaneously reduce the NOx emission below the IMO Tier III limit, it's essential to optimise the engine operating settings that affect the engine responses. In this study, the following factors are considered for the optimisation: (a) pilot injection timing, that imposes a direct effect on the combustion phase, and consequently the NOx emission and BSFC; (b) waste gate opening affecting the boost pressure and equivalence ratio; (c) natural gas mass which determines the input energy and equivalence ratio. The GT-ISE built-in multi-objective genetic algorithm (MOGA) was employed to conduct the optimisation due to its outstanding performance in dealing with multiple conflicting objectives (engine responses). The Nondominated Sorting Genetic Algorithm II (NSGA II) [69] was selected because of its high-resolution and evenly distributed Pareto front, which improve the calculation speed and robustness of the optimisation process. Table 4.8 presents the genetic algorithm settings, which are recommended by the GT-ISE manual by considering the variable number and simulation cases.

Table 4.8 Genetic algorithm settings

Parameter	Valve
Population size	40
Number of generations	10
Crossover rate	1
Crossover rate distribution index	15
Mutation rate	Calculated
Mutation rate distribution index	20
Random seed	Random

The optimisation flowchart and optimisation process parameters are presented in Figure 4.6 and Table 4.9, respectively. In this study, the Nondominated Sorting Genetic Algorithm II (NSGA II) [140] was used for conducting the engine settings optimisation. Pilot injection timing, equivalence ratio variation and natural gas mass variation were employed as inputs variables, whilst the NOx emission and BSFC were set as objectives. The optimisation process was constrained by the Tier III NOx emission limit and compressor surge margin.

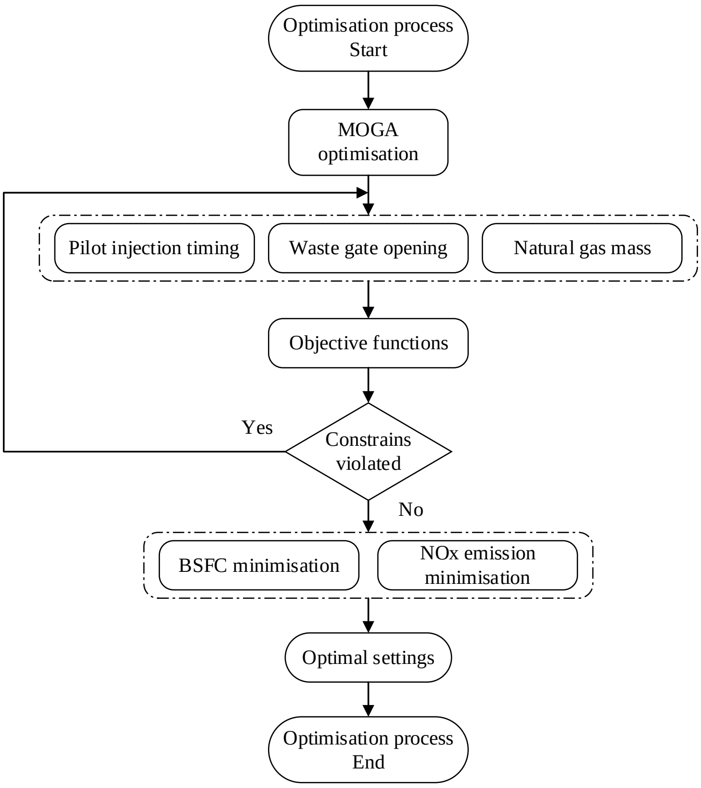

Figure 4.6 Optimisation flowchart

As seen from Table 4.9, three operation conditions (1457 r/min, 1629 r/min and 1800 r/min) are included in the optimisation and represented by the case ID 1, 2 and 3. The pilot injection timing is assumed to vary from –7.5 °CA to –5 °CA with step intervals of 0.5 °CA. The waste gate in the proposed 0D/1D simulation model is represented by an orifice which renders variable flow area for the turbine bypass flow by changing the diameter. In this study, the waste gate opening is defined as the fraction of the current flow area to the maximum flow area rather than rotational angle of the waste gate valve. The range of waste gate opening is assumed to be 0-100%, considering step intervals of 10% of the maximum flow area. The natural gas mass variation ranges from 0 to 20% at 1800 r/min and 1629 r/min operation conditions, whilst NG mass variation at 1457 r/min operation condition varies between –10% to 10%. The step intervals for NG mass variation at three operation loads are set to be 5%. The optimization process is constrained by the Tier III NOx emission limit (2.01 g/kWh) and the compressor surge margin limit (15%). A surge margin provides a measure of how close an operating point is to surge. The objectives are the simultaneous reduction of NOx emission and brake specific fuel consumption (BSFC).

Table 4.9 Optimisation process parameters

Optimisation phase	Case study ID	-	1	2	3
	Rotational speed	r/min	1457	1629	1800
Variable settings	Pilot injection timing	°CA	–7.5 to –5		
	Waste gate valve opening	%	0 to 100		
	Natural gas mass variation	%	–10 to 10	0 to 20	
Constrains	Tier III NOx emission limit	g/(kW·h)	2.01		
	Compressor surge margin limit	%	15		
Objectives	NOx emission	g/(kW·h)	minimise		
	BSFC	g/(kW·h)	minimise		

4.4 Chapter summary

In this chapter, the engine characteristics and experiment setup were introduced firstly and followed by the design of simulation case studies including parametric investigation using 3D simulation, Wiebe combustion model calibration and engine setting optimisation.

Chapter 5. Models setup and validation

5.1 Chapter outline

In this chapter, the model setting up process of the proposed 0D/1D and 3D simulation models will be introduced. Then, the prediction accuracy of the proposed 0D/1D model will be validated by a quantitative comparison between the simulated and measured in-cylinder pressures as well as performance parameters. Finally, the accuracy of the proposed 3D simulation model will be verified by using the in-cylinder pressure, heat release rate and emissions obtained from the experiment.

5.2 0D/1D Model setup and validation

5.2.1 Model layout and setup

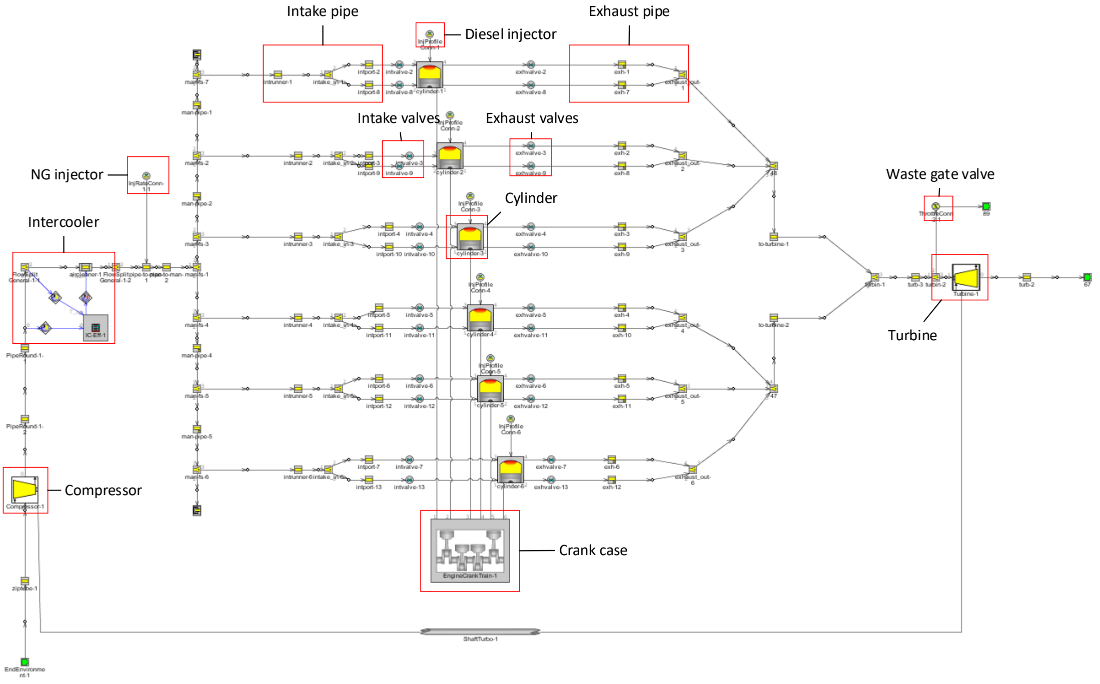

Figure 5.1 The 0D/1D model of the investigated DF engine developed with GT-ISE

The 0D/1D simulation model of the investigated marine DF engine is developed with the GT-ISE software. As seen from Figure 5.1, the major sub-models include the compressor, intercooler, NG injector, intake pipes, intake valves, diesel injectors, cylinders, exhaust valves, exhaust pipes, turbine, waste gate valve and crank case. NG is injected into the manifold and mixed with the boosted air before entering the cylinders. The pilot diesel is injected directly into the cylinders and ignite the NG-air mixture at the end of compression stroke. The waste gate valve is employed to adjust the bypass mass of exhaust gas directly to the atmospheric environment, thus controlling the turbine mass flow and the compression ratio.

Table 5.1 Input parameters of the developed 0D/1D simulation model

Geometric dimensions	Bore [m]	Fuel parameters	Composition
	Stroke [m]		Injection pressure [bar]
	Compression ratio [-]	Combustion model	*SOC*, *EOC* [°CA]
	Connecting rod length [m]		b_i
	Valve timings [°CA]		$m_{v,\,i}$
Working condition	Rotational speed [r/min]	Heat loss model	T_{head} [K]
	Injected fuel mass [kg/cycle/cylinder]		T_{liner} [K]
			T_{piston} [K]
Intake/exhaust system	Pipe length [m]	Turbocharger	MAP
	Pipe diameter [m]		Rotational inertia [kg·m^2]
	Split angle [°]		
Intercooler	Cooling coefficient [-]	Speed governor	Proportionality constant [-]
	Coolant temperature [K]		Integration constant [-]
Initial conditions	Pressure [bar]	Simulation parameters	Duration
	Temperature [K]		Step
	Charge efficiency [-]		Solver

Table 5.1 shows the input parameters of the developed 0D/1D simulation model. The geometric dimensions are the primary inputs of the proposed model. The engine rotational speed and the injected fuel mass need to be provided for determining the working conditions of the investigated internal combustion engines. The employed fuels (liquid or gaseous) along with their compositions needs to be provided as input. For the combustion simulation of a direct-injection liquid fuel engine, the injection pressure is essential to evaluate the specific energy (e_f) caused by the injection pressure difference and the evaporation. In the *Combustion Model*, the Wiebe parameters are required to calculate the heat release rate. In addition, the wall temperatures of the cylinder head, the cylinder liner and the piston top need to be set. For modelling the intake and exhaust systems, pipe length, pipe diameter and split angle are essential inputs. The shaft inertia, turbine and compressor MAPs are used to determine the working condition of the turbocharger. Cooling coefficient and coolant temperature are needed for modelling the intercooler. The working condition of speed governor is determined by the PI controller, which requires the proportionality constant and integration constant as inputs. The in-cylinder pressure and temperature at IVC are used

to calculate the gas mass trapped in the cylinder at IVC for determining the initial conditions. The charge efficiency is defined as the mass ratio of the fresh air and the total trapped gas, which considers the existence of residual gas from previous working cycle. The simulation period is set as 100 cycles, whilst the simulation step is set to be 0.5°CA. The crank angle is obtained from the time integration of the rotational speed assuming that the rotational speed remains constant. In addition, the fourth-order Runge-Kutta algorithm is used as the equation solver.

5.2.2 Combustion model calibration based on measured in-cylinder pressure

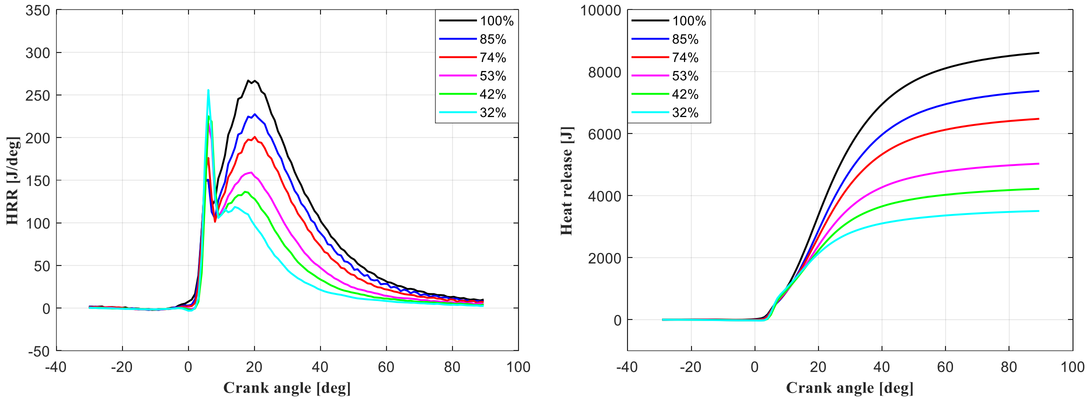

(a) Heat release rate (b) Integrated heat release

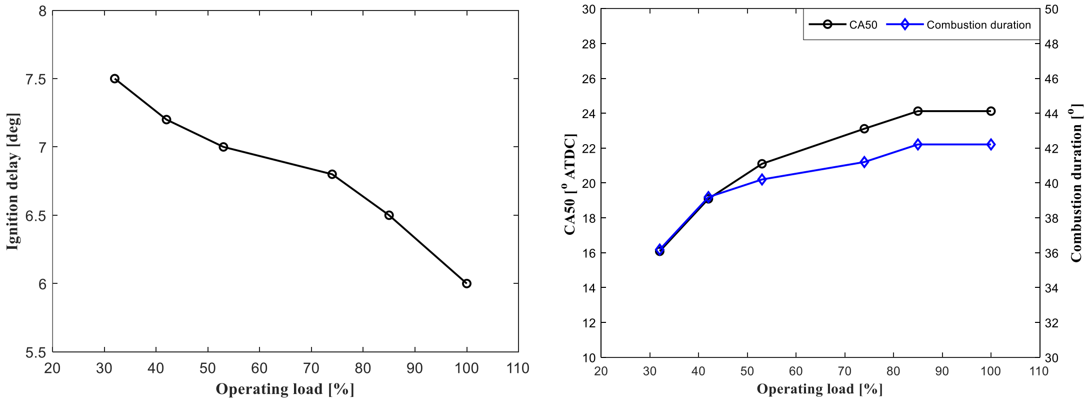

(c) Ignition delay (d) CA50 and combustion duration

Figure 5.2 HRR analysis at different operating conditions under propeller characteristics

The smoothed in-cylinder pressures were used to calculate the HRR under 6 working conditions of the propulsion characteristic curve, as presented in Figure 5.2. As seen from Figure 5.2 (a) and (b), the integrated heat release (IHR) and second peak heat release rate (HRR) get higher with the operation load increase, whilst the first peak HRR decreases. The higher first peak HRR at low operation load can be explained by the longer ignition delay in Figure 5.2 (c) which allows enough time for entraining gaseous fuel into the diesel spray resulting in more heat release in the Stage 1 combustion. The shortened ignition delay at higher operation load is caused by the higher compression pressure and temperature, which stimulates the spontaneous combustion after the pilot injection timing. In Figure 5.2 (d), CA50 and the combustion duration are used to characterize the combustion phase at different operating load. CA50 is the crank angle corresponding to 50% of the IHR end value. The combustion duration of the total HRR is defined as the difference between CA10 and CA90, namely the crank angle corresponding to 10% IHR and 90% IHR. CA10 and CA90 are selected for describing the overall combustion duration because SOC (1% IHR) and EOC (99% IHR) may lead to an inaccurate characterisation of the main combustion stage by involving flame kernel development period and tail combustion period. When the operation load increases from 32% to 100%, the CA50 is postponed by around 8 °CA while the combustion duration increased by 6 °CA.

Before validating the 0D/1D simulation model of reference DF engine, the Wiebe combustion parameters must be calibrated first by using experimentally obtained HRR. According to the critical review on DF engine combustion characterisation in Section 2.3.2, the heat release rate of DF engines can be characterized by employing two or three Wiebe functions. In this section, three Wiebe functions are adopted for DF engine combustion characterisation to guarantee sufficient accuracy. Subsequently, the combined use of curve fitting technology and schematic algorithm proposed by Bilcan [97] was employed to obtain the three sets of Wiebe parameters (φ_i, $\Delta\varphi_\mathrm{i}$, b_i and m_i). The detailed procedures followed for determining Wiebe combustion parameters can be referred to Section 3.5.2. Table 5.2 shows the variation range of the Wiebe combustion parameters at 100% operation condition. The lower and upper limits of the employed Wiebe combustion parameters are referred to literature [81, 133], whilst the initial values were obtained by using the schematic algorithm proposed by Bilcan's [97]. It is worth mentioning that weigh factor b_3 can be calculated after knowing b_1 and b_2 based on the principle that the sum of b_1, b_2 and b_3 equals to one. The upper limits of $\Delta\varphi_2$ and $\Delta\varphi_3$ are represented by the overall combustion duration τ_{comb}.

Table 5.2 Variation range of the Wiebe combustion parameters at 100% operation load

	b_1	b_2	m_1	m_2	m_3	$\Delta\varphi_1$	$\Delta\varphi_2$	$\Delta\varphi_3$
	-	-	-	-	-	°CA	°CA	°CA
Lower limit	0.00	0.40	0.0	0.0	0.0	0.0	5.0	5.0
Upper limit	0.20	0.90	5.0	5.0	5.0	8.0	τ_{comb}	τ_{comb}
Initial value	0.09	0.60	1.7	1.8	0.8	4.0	50.0	100.0

The fitted Wiebe parameters are presented in Table 5.3. Figure 5.3 shows the Wiebe parameters variation against the normalized load on the propeller operation characteristic curve. As can be deduced from Table 5.3 and Figure 5.3, the SOC of the diesel fuel and natural gas is advanced from 2.5°CA ATDC to 1°CA ATDC when the operating condition varied from 32% load to 100% load. The shape exponents (m_1, m_2 and m_3) for the three combustion stages exhibit a rough rising trend with the load increase. The weight factors b_1 and b_2 decrease when the operating condition increases from 32% load to 100% load, whilst the weight factor b_3 shows an opposite trend. The combustions duration of stage 1 and stage 2 show minor difference with the operating condition, while that of stage 3 decrease by 10 ° with the operating load increase.

Table 5.3 Wiebe combustion parameters under working conditions of propeller characteristics curve

Load %	SOC °CA	b_1 -	b_2 -	b_3 -	m_1 -	m_2 -	m_3 -	$\Delta\varphi_1$ °CA	$\Delta\varphi_2$ °CA	$\Delta\varphi_3$ °CA	R_s -
100	1.0	0.02	0.44	0.53	4.0	1.4	0.9	6.64	49.0	108	0.998
85	1.5	0.04	0.46	0.50	3.0	1.3	0.8	6.63	50.4	111	0.999
74	1.8	0.05	0.50	0.45	2.9	1.3	0.8	6.69	51.7	116	0.999
53	2.0	0.09	0.60	0.32	3.4	1.1	0.9	7.11	51.3	116	0.999
42	2.2	0.11	0.60	0.29	3.3	1.0	0.9	7.11	49.1	116	0.998
32	2.5	0.15	0.58	0.28	2.7	0.9	0.8	6.59	45.6	119	0.999

To predict Wiebe combustion parameters under working conditions of propeller characteristics curve, a response model was proposed based on the obtained Wiebe combustion parameters in Table 5.3. Table 5.4 shows the fitted correlations of Wiebe combustion parameter obtained by using curve fitting tool in MATLAB. Wiebe combustion parameters are considered as functions of normalised operating load. The effect of rotational speed is also included in the correlations because there is a certain correspondence between rotational speed and engine load when engines operate under propeller characteristics curve. It is worth mentioning that the proposed correlations can only be used for investigating engine behaviour on the propeller characteristics curve.

Figure 5.4 presents the original HRR calculated from measured pressure and the fitted HRR surface obtained by using correlations in Table 5.4. As indicated by the comparison, the fitted HRR surface proves to accurate enough in predicting HRR against the normalised operating load and crank angle. Nevertheless, the fitted HRR surface in Figure 5.4 can only be used for predicting HRR under propeller characteristic curve because the correlations accuracy in Table 5.4 highly depends on experimentally obtained HRR.

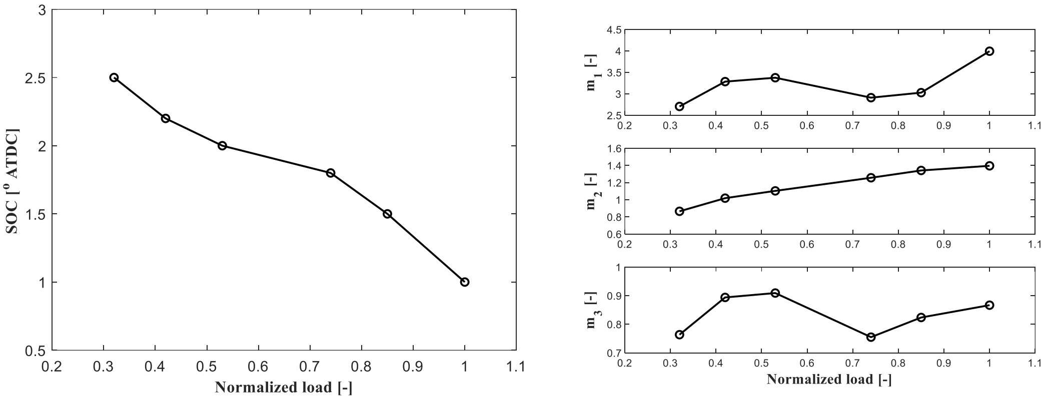

(a) Start of combustion

(b) Shape factors

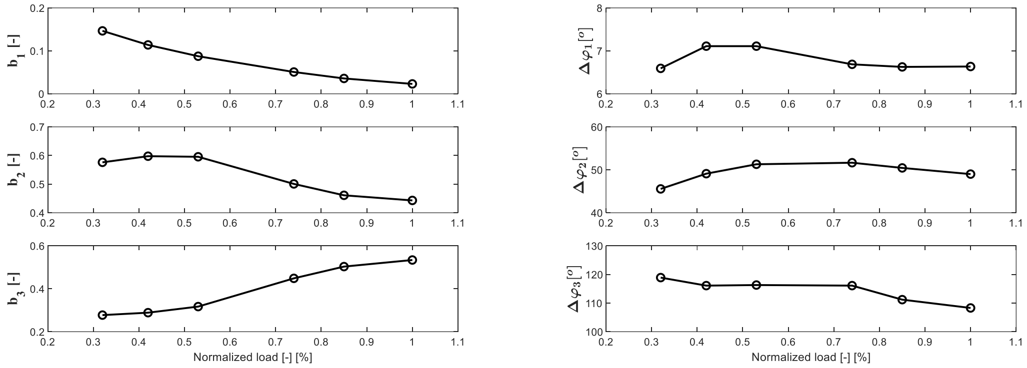

(c) Weight factors

(d) Combustion duration

Figure 5.3 Wiebe parameter variation with normalised load

Table 5.4 Wiebe parameters correlations under working conditions of propeller characteristics curve

	Functions	R-square
SOC	$f(x) = -1.15\cdot x^2 - 0.464\cdot x + 2.68$	0.971
m_1	$f(x) = 36.56\cdot x^3 - 70.2\cdot x^2 + 42.57\cdot x - 4.992$	0.997
m_2	$f(x) = -0.6821\cdot x^2 + 1.657\cdot x + 0.4189$	0.995
m_3	$f(x) = -97.46\cdot x^5 + 296.7\cdot x^4 - 338.9\cdot x^3 + 178.7\cdot x^2 - 42.67\cdot x + 4.439$	0.999
b_1	$f(x) = 0.1918\cdot x^2 - 0.4311\cdot x + 0.2631$	0.999
b_2	$f(x) = 2.273\cdot x^3 - 4.776\cdot x^2 + 2.878\cdot x + 0.06801$	0.997
$\varDelta\varphi_1$	$f(x) = 19.62\cdot x^3 - 41.4\cdot x^2 + 26.8\cdot x + 1.642$	0.951
$\varDelta\varphi_2$	$f(x) = 56.98\cdot x^3 - 153\cdot x^2 + 126\cdot x + 19$	0.999
$\varDelta\varphi_3$	$f(x) = 851.5\cdot x^4 - 2299\cdot x^3 + 2195\cdot x^2 - 883.3\cdot x + 243.3$	0.992
x is the normalised operating load, $0 < x < 1$.		

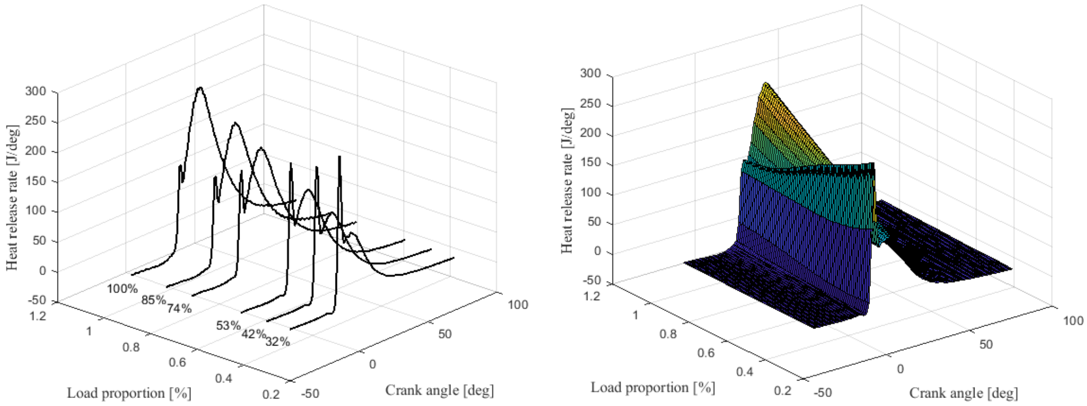

(a) Calculated HRR (b) Fitted HRR surface

Figure 5.4 Calculated HRR and fitted HRR surface under working conditions of propeller characteristics curve

5.2.3 Model validation

As the proposed 0D/1D model is based on the calculation of the working medium thermodynamic properties and multi-Wiebe combustion functions, it is practically capable of predicting the performance of dual fuel engines with the developed properties library and the appropriate combustion model calibration. In order to validate the model accuracy at steady operating conditions, the comparison between the simulation result and measured data are carried out at the 32%, 53%, 74% and 100% operation loads covering the full range conditions. The NG fuel injection model for the DF engine is described by employing constant injection rates of 17.89 kg/h, 32.90 kg/h, 47.89 kg/h and 59.47 kg/h at 32%, 53%, 74% and 100% operation loads, respectively. The pilot diesel injection timing is fixed at 5°CA before TDC, whilst the injection mass rates of each diesel injector (6 diesel injectors in total) are 0.63 kg/h, 0.77 kg/h, 0.89 kg/h and 0.99 kg/h at 32%, 53%, 74% and 100% operation loads, respectively. The simulation cycle for each operating condition is fixed to 100 cycles with fixed simulation step 0.001 s, which guarantee enough stabilization time and high resolution.

The simulated and measured in-cylinder pressure variations are presented in Figure 5.5, which demonstrates that the simulated pressure diagrams exhibit a sufficient agreement with the measured ones. The quantitative comparisons of p_{max}, α_1, p_{com}, p_{EO} and IMEP are shown in Table 5.5. As the combustion starts after TDC in the investigated engine, the pressure at TDC is selected as the p_{com}. As can be deduced from Table 5.5, the relative errors of p_{max}, p_{com}, p_{EO} and *IMEP* are below 4%, whilst the absolute difference of the peak pressure position is less than 1°CA.

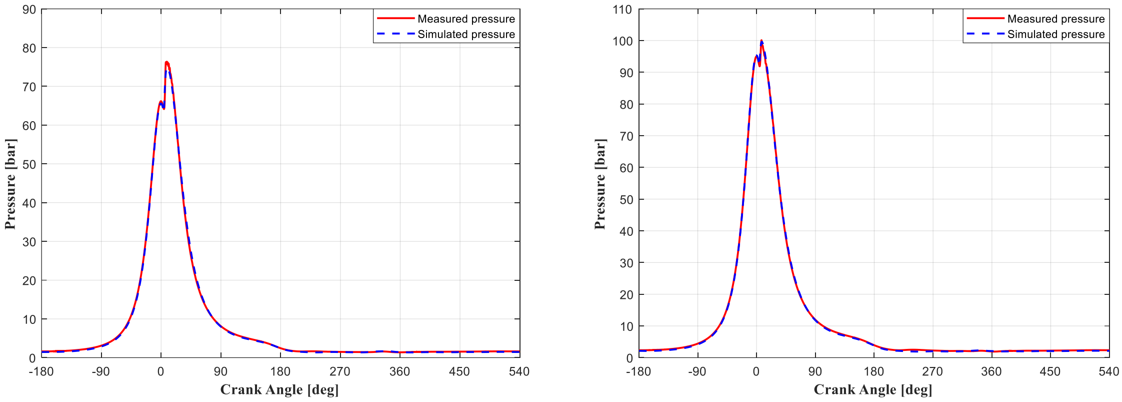

(a) 32% load (b) 53% load

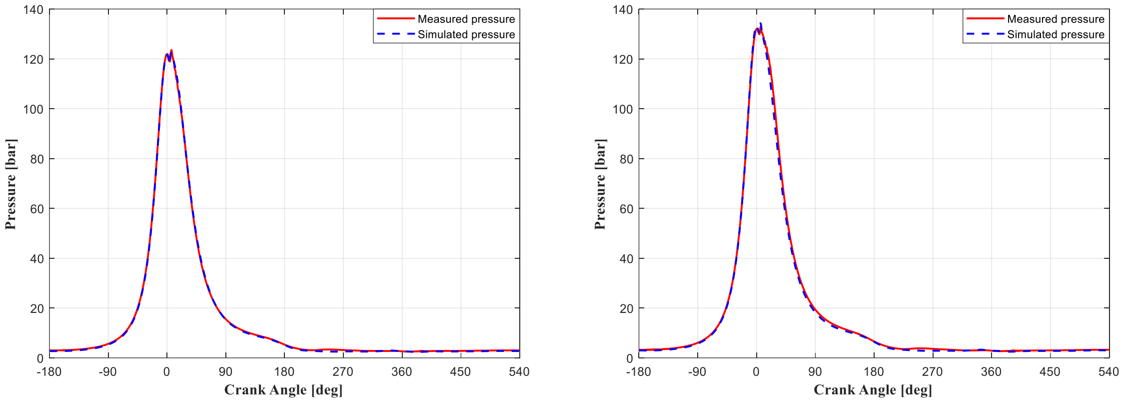

(c) 74% load (d) 100% load

Figure 5.5 In-cylinder pressure comparison at different operation loads

Table 5.5 Quantitative Comparison between the simulated and measured in-cylinder pressure

Load	Parameters	p_{max} (bar)	α_1 (°CA)	p_{com} (bar)	p_{EO} (bar)	IMEP (bar)
32%	Simulation	76.05	7.30	66.15	4.87	9.37
	Experiment	74.81	9.49	65.59	5.06	9.70
	Error (% or °CA)	1.66	2.19	0.85	3.75	3.40
53%	Simulation	99.37	8.02	94.87	7.25	12.84
	Experiment	100.08	7.80	95.06	7.48	12.39
	Error (% or °CA)	0.7	0.22	0.2	3.07	3.63
74%	Simulation	128.43	5.64	128.09	10.46	17.89
	Experiment	128.00	6.23	127.42	10.56	18.00
	Error (% or °CA)	0.33	0.59	0.52	0.95	0.61
100%	Simulation	134.31	5.29	133.20	11.36	19.16
	Experiment	132.89	6.40	132.10	11.80	18.90
	Error (% or °CA)	1.07	1.11	0.83	3.73	1.38

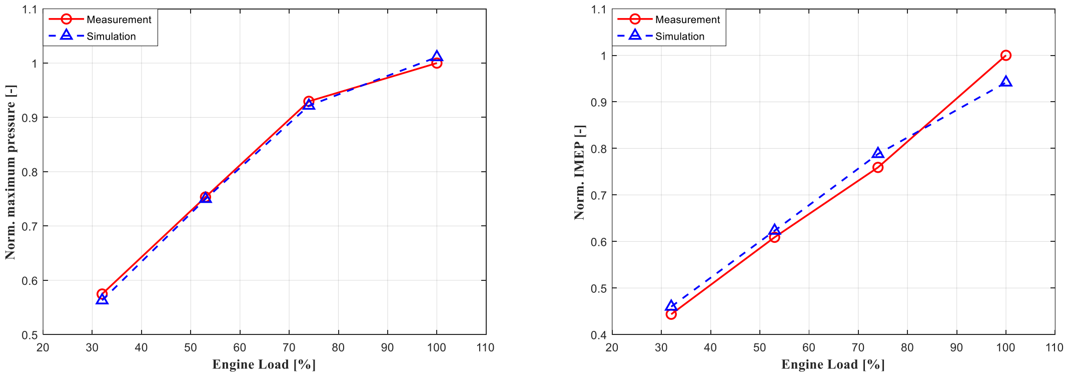

(a) Normalised maximum pressure (b) Normalised IMEP

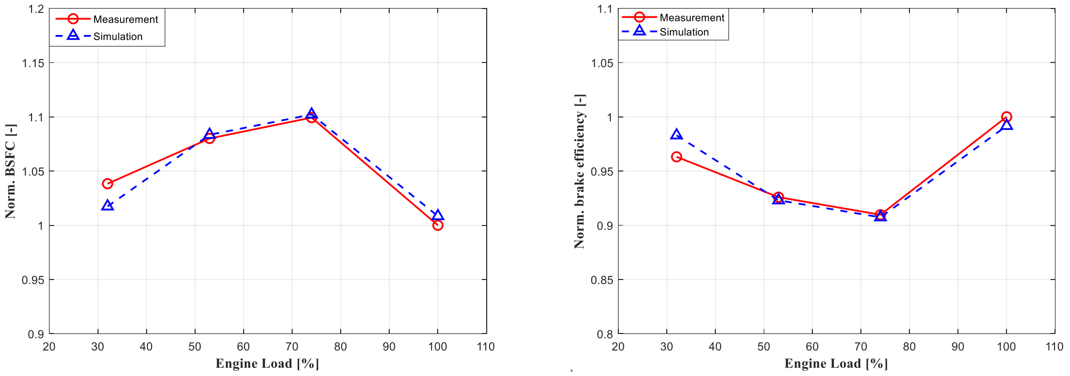

(c) Normalised equivalent BSFC (d) Normalised brake efficiency

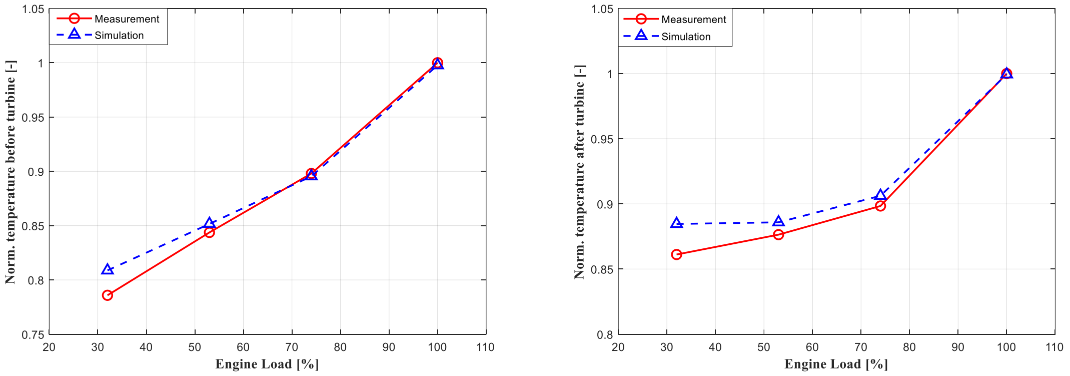

(e) Normalised temperature before turbine (f) Normalised temperature after turbine

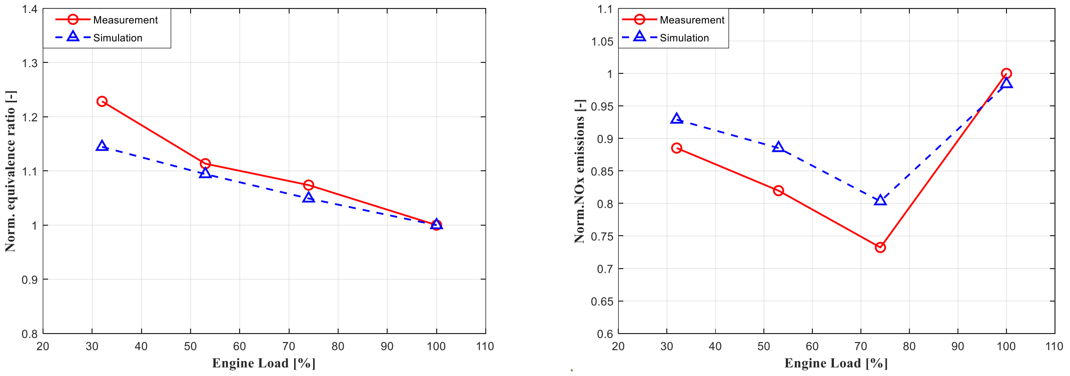

(g) Normalised equivalence ratio (h) Normalised NOx emission

Figure 5.6 Simulation results and comparison with available experiment data

In Figure 5.6, a set of engine performance parameters are compared to the measured data, including the maximum pressure, the indicated mean effective pressure (IMEP), the equivalent brake specific fuel consumption (BSFC), the brake efficiency, the exhaust temperature before and after turbine, equivalence ratio and NOx emissions. The equivalent BSFC in this study is obtained by converting the BSFC of the two employed fuels (natural gas and diesel) into that of natural gas according to the principle of equivalent calorific value. All the presented parameters in Figure 5.6 are normalised by using the measured data at 100% operation load. As inferred from Figure 5.5, Table 5.5 and Figure 5.6, the developed 0D/1D model is capable of adequately predicting the performance and NOx emissions of the investigated DF engine, and thus can be used with fidelity for the operating setting optimisation presented in the following study. It's worth mentioning that the lowest brake efficiency is achieved at 74% operation load, which seems abnormal for a marine DF engine operating under the propeller characteristics. It might be attributed to the decreasing equivalence ratio with the increase of operation load or potential measurement errors.

5.3 3D Model setup and validation

5.3.1 Model setup

In the present study, the combustion chamber geometry of the investigated DF engine was modelled by using the *Make engine sector surface* tool which is embedded in the CONVERGE software. As the eight nozzle orifices are evenly spaced around the pilot injector, a 45°CA sector mesh of the combustion chamber was used to model one spray plume to take advantage of the axial symmetry. The computational domain at the TDC is shown in Figure 5.7. The mesh document in CVG.in format was then imported to the CONVERGE studio, which was used to set the initial conditions, boundary conditions, spray model, combustion model and emission model. The simulation duration of the developed three-dimensional (3-D) model starts from the inlet valve closure (IVC) to exhaust valve open (EVO).

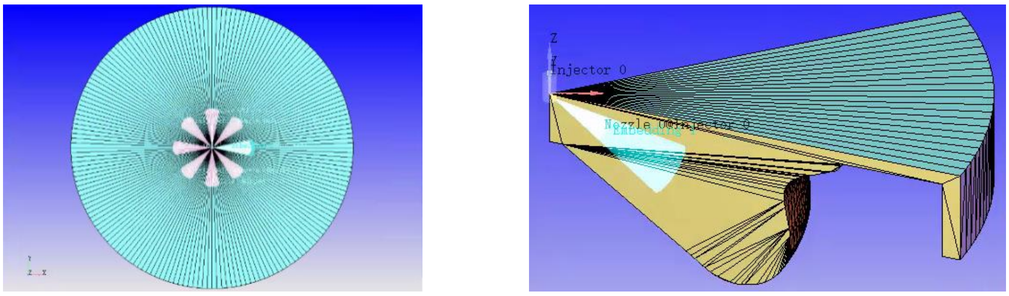

Figure 5.7 Computational domain of complete and one-eighth of the combustion chamber at TDC

Table 5.6 Input parameters of the developed 3D simulation model

Geometric dimensions	Basic dimensions	Bore [m]	
		Stroke [m]	
		Compression ratio [-]	
		Connecting rod length [m]	
		Valve timings [°CA]	
		Rotational speed [r/min]	
	Combustion chamber dimensions	Piston bowl profile [-]	
		Cylinder head profile [-]	
		Crevice distance [m]	
	Pilot injector dimensions	Injector profile [-]	
		Nozzle diameter [-]	
		Spray cone angle [°CA]	
		Tilt angle in the xz plane [°CA]	
Combustion model	Activation temperature [K]	Injection model	Start of injection [°CA]
	Reaction kinetics mechanism		Injection duration [°CA]
			Injection mass [kg]
	Reaction multiplier [-]		Injection rate profile [-]
Initial conditions	Pressure [bar]	Boundary conditions	Head temperature [K]
	Temperature [K]		Linear temperature [K]
	Species mass fraction [%]		Piston temperature [K]
	Turbulence kinetic energy $[m^2/s^2]$	Simulation setting	Start time [°CA]
			End time [°CA]
	Turbulence dissipation $[m^2/s^2]$		Step [s]
			Solver

Table 5.6 shows the input parameters of the developed 3D simulation model. The geometric dimensions especially the profiles of piston bowl, cylinder head and pilot injector are essential inputs for generating an accurate mesh document of the in-cylinder space. The SAGE model is selected for simulating the dual fuel combustion, whilst the optimized GRI-Mech 3.0 and Valeri coupling mechanism [126] are used to describe the detailed chemical kinetics. The combustion activation temperature is usually set to be 600 K representing the minimum cell temperature for combustion beginning. The reaction multiplier is the scaling factor of reaction rate in the SAGE combustion model ranging from 0.1 to 10, whilst the default value 1 is recommended by the CONVERGE manual. In order to obtain an accurate description of the pilot diesel, the Blob injection model [122], the KH-RT model [123] and the Frossling model [124] were selected to simulate the injection, breakup and evaporation process of the pilot diesel, respectively. The start of injection, injection duration, injection mass and injection rate profile are

obtained by experiment measurement. The in-cylinder pressure and temperature at IVC, which are approximated by using the inlet pressure and temperature measured at manifold, are used to calculate the gas mass trapped in the cylinder at IVC for determining the initial conditions. As the natural gas is injected into the manifold and premixed with fresh air, the mass fractions of air and natural gas are calculated according to the equivalence ratio assuming that there is no residual gas left inside the cylinder. In order to reduce the computation complexity, methane is used to represent natural gas for chemical kinetic calculation in the developed 3D simulation model. In addition, the turbulence kinetic energy and turbulence dissipation need to be provided in the RNG k-ε turbulence model [127]. The boundary conditions, i.e., temperatures of cylinder head, linear and piston, are taken from reference [149]. The simulation period is set from inlet valve close (IVC) to exhaust valve open (EVO), whilst the simulation step is set to be 0.5°CA during the combustion stage and 1°CA during the rest stages.

5.3.2 Computation mesh study

CONVERGE provides a mesh control strategy with base grid size, adaptive mesh refinement (AMR) and fixed mesh refinement. The details of employed mesh control strategy are shown in Table 5.7. In the present study, the maximum embedding level and sub grid criterion of velocity adaptive mesh refinement were set to 2 and 2.0 m/s, respectively. The maximum embedding level and sub grid criterion of temperature adaptive mesh refinement was set to 2 and 5.0 K, respectively. The fixed refinement scale of the nozzle was set to 2, while those of the piston and head were set to 1. For all the mesh refinement except the nozzle, the refinement durations start from –20 °CA to 129 °CA in order to cover the combustion and compression process. However, the duration of the nozzles mesh refinement was set from –5° CA to 10 °CA, which corresponds to the pilot injection duration of the baseline case. When investigating the effects of pilot injection timing in the following study, the duration of the nozzles mesh refinement needs to be adjusted according to the actual injection timing.

The base grid size is an important parameter that affects the computation speed and prediction accuracy of CFD models. In order to exclude the influence brought by mesh grid size, a comparison of in-cylinder pressure with 4 grid sizes at nominal operation condition is conducted to check the mesh grid size independence, as presented in Figure 5.8. The pressure curve of grid 3 is remarkably consistent with that of grid 4, but differs from that of grid 1 and grid 2. Balancing the computation cost and prediction accuracy, grid 3 of 2 mm basic grid size and 33689 basic cells would be the best choice for the following CFD modelling.

Table 5.7 Mesh control strategy

Base grid size	1.5mm, 2.0mm, 2.5mm,3.0mm			
Adaptive mesh refinement		Max embedding level	Sub-grid criterion	Duration
	Velocity	2	2.0 m/s	–20 °CA to 129 °CA
	Temperature	2	5.0 K	–20 °CA to 129 °CA
Fixed mesh refinement		Scale	Embed layers	Duration
	Nozzles	2	-	–5° CA to 10 °CA
	Piston	1	1	–20 °CA to 129 °CA
	head	1	1	–20 °CA to 129 °CA

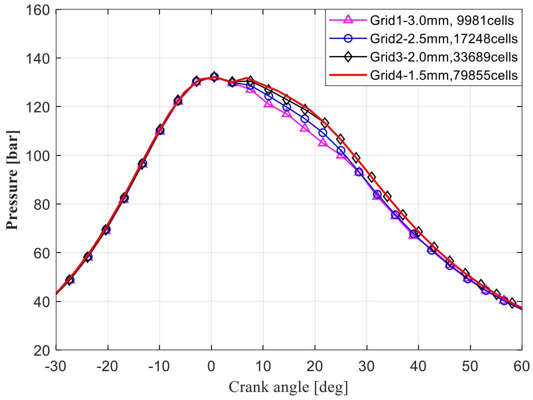

Figure 5.8 In-cylinder pressure comparison with 4 base grid sizes

5.3.3 Knocking detection

In order to detect potential knocking occurrence inside the combustion chamber, seven monitoring points were evenly placed at the XY plane to monitor the local pressure oscillation, as shown in Figure 5.9. Considering knocking phenomenon is usually caused by spontaneous combustion in the end-gas region before flame front arrives [47], knocking is not likely to occur around the piston bowl because the spray penetration of pilot diesel almost reaches the longest distance of piston bowl. The seven monitoring points were placed near cylinder head (points P1-P4) and liner (points P5-P7) [149, 150] which are away from the pilot diesel spray and thus are prone to auto-ignition before approached by the flame front.

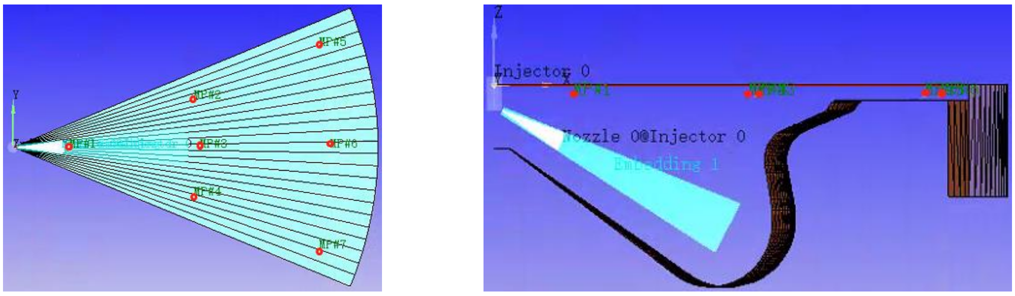

Figure 5.9 Location of the monitoring points

The knock index (KI) was introduced to define the intensity of knock [151] to quantity the knock phenomenon. The definition of KI is shown in Eq (5.1).

$$KI = \frac{1}{N}\sum_{1}^{N} PP_{\max,n} \tag{5.1}$$

Where, $PP_{max,n}$ is the largest absolute difference of the band-pass (5 kHz ~ 20 kHz) filtered pressure [152] at position n.

Figure 5.10 (a) shows the local pressure at 7 positions and the average pressure at the baseline case. As seen from Figure 5.10 (a), the local pressures at position 2,3 and 4 almost coincide with each other, which is the same case for the local pressures at position 5, 6 and 7. The local pressure at position 1 indicates the highest fluctuation frequency, while that of the local pressures at position 5, 6 and 7 is the lowest. In addition, the maximum local peak pressure occurs at position 5, 6 and 7. The raw pressure and band-pass filtered pressure at position 1 are presented in Figure 5.10 (b), which explains the determination of the parameter $PP_{max,n}$.

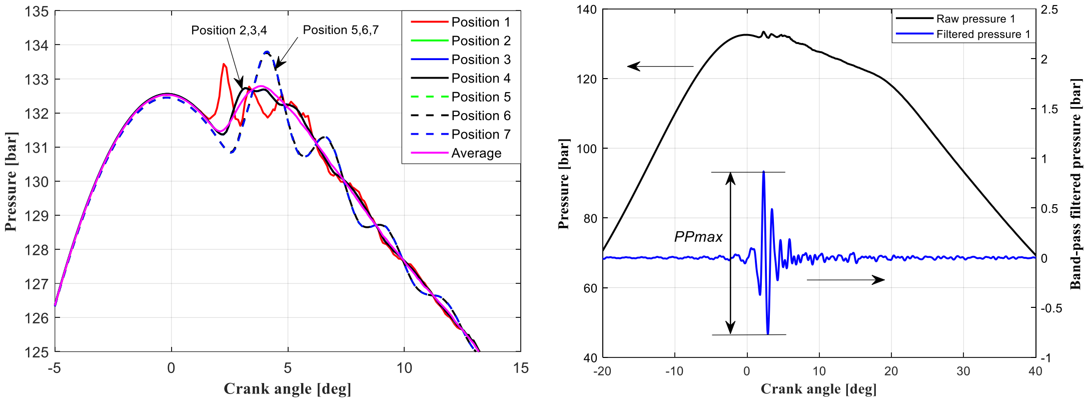

(a) Local pressure at different positions and the average pressure

(b) Raw pressure and filtered pressure at position 1

Figure 5.10 Pressure analysis at the baseline case

5.3.4 Model validation

The measured in-cylinder pressure, heat release rate and emissions (NOx, CO and HC) at 4 operation conditions of propeller characteristic were used to validate the accuracy of the developed CFD model. The in-cylinder pressure signals, as measured from engine facilities, are very erratic due to the inherent character of the combustion process. Thus, the method in [153] was employed to smooth the pressure signal, which is then averaged by 200 cycles for model validation.

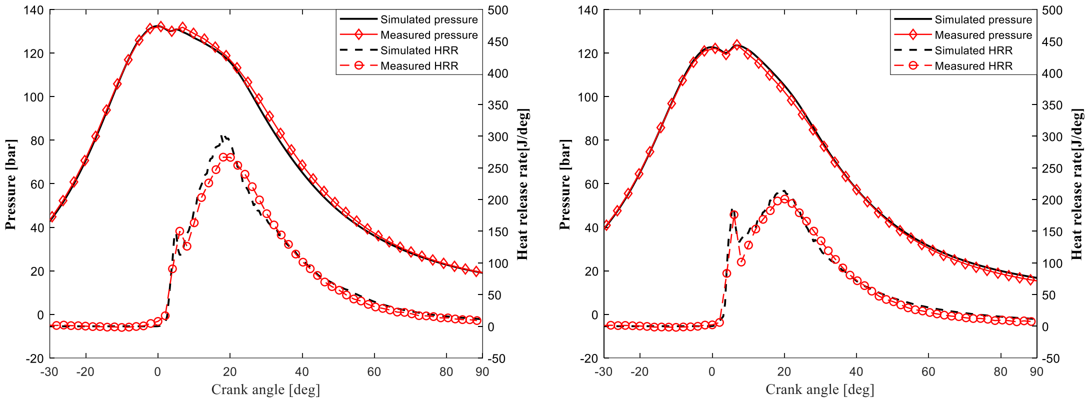

(a) 100%

(b) 74%

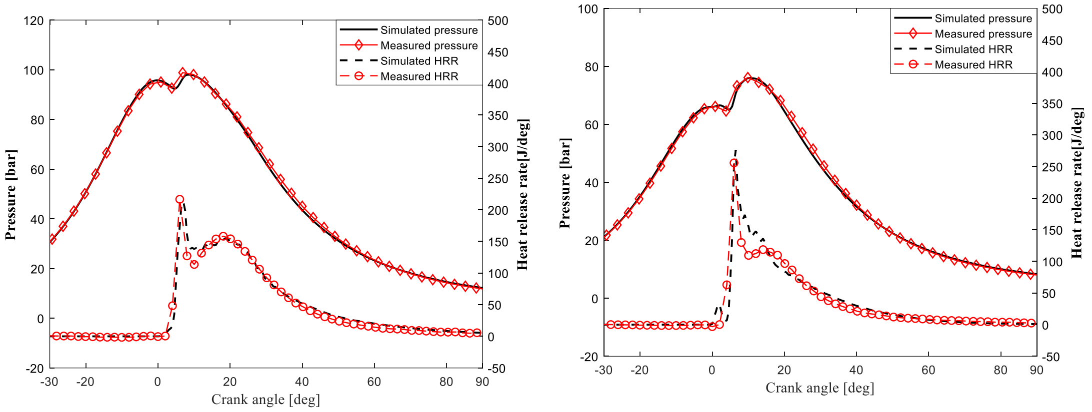

(c) 53%

(d) 32%

Figure 5.11 Simulated and measured in-cylinder pressure and heat release rate of the investigated engine at different operation loads: (a) 100%; (b) 74%; (c) 53%; (d) 32%.

Before comparing the simulated HRR and experimentally obtained HRR, the heat losses of CFD model and HRR calculation model need be checked if they match because the simulated HRR is a direct product of the actual fuel consumption rate, whilst the experimentally obtained HRR is calculated from the measure in-cylinder pressure with heat loss estimation. The match between the heat losses of CFD model and HRR calculation model can be justified by considering the heat transfer coefficient, heat transfer surface area, mean temperature and boundary conditions. First of all, the heat transfer coefficients in both cases are evaluated by using the Woschni model, whilst the heat transfer surface area is calculated according to the geometry dynamics. The measured pressure matches the simulated one, proving the average measured temperature is basically in accordance with the average temperature simulated by CFD model. In addition, the boundary conditions, i.e., the temperatures of cylinder head, linear and piston, are set the same in the CFD model and the HRR calculation model. Thus, it is inferred that the heat loss of the CFD model matches that of the HRR calculation model.

Figure 5.11 shows the comparison of the simulated and measured in-cylinder pressure and heat release rate (HRR) at 4 different operation conditions. As seen from Figure 5.11, the simulated results agree well with the measured data, which proves that the developed CFD model is capable of predicting the engine performance with high accuracy. However, the peak values of simulated HRR are higher than those of the measured HRR, which might be caused by the following reasons: (1) all the cells are considered as prefect mixing zones in the CFD model, resulting in faster combustion speed of homogeneous charger, whilst the actual mixture is usually inhomogeneous; (2) the boundary conditions set in the CFD model, like the cylinder head temperature, liner temperature and piston temperature, might not coincide with those actual values.

The comparisons of the simulated and measured emissions (NOx, CO and HC) are presented in Table 5.8. All the relative errors between the simulation result and measured data are less than 10% except those of HC emission at 74%, 53% and 32% operation load conditions. It might be caused by the over estimation of the in-cylinder temperature at these three operation conditions, which can be inferred from the fact that the simulated NOx emissions are higher than the measured NOx emissions. In addition, the methane slip during gas exchange is not included in the simulation, making the simulated HC emission less than the measured data. Considering the mentioned factors, the emission prediction accuracy of the developed model is acceptable.

Table 5.8 Comparison between the simulated and the measured emissions.

Load		NOx g/(kW·h)	CO g/(kW·h)	HC g/(kW·h)
100%	Measurement	1.83	6.82	17.67
	Simulation	1.67	7.47	18.80
	Relative error (%)	8.74	9.53	6.40
74%	Measurement	1.34	9.36	32.45
	Simulation	1.47	8.55	28.40
	Relative error (%)	9.70	8.65	12.48
53%	Measurement	1.50	7.21	24.93
	Simulation	1.62	6.50	22.30
	Relative error (%)	8.80	9.85	10.55
32%	Measurement	1.62	3.77	10.30
	Simulation	1.70	3.45	8.90
	Relative error (%)	4.94	8.49	13.59

Figure 5.12 show the simulated and measured emissions of the investigated engine at different operation conditions (32%, 53%, 74% and 100% load). As seen from Figure 5.12 (a), the NOx emission decreases with the increased operation load from 32% to 74% and turns up at 100% operation load, whilst the NOx emissions at all the 4 operation loads are below the Tier III limit. In Figure 5.12 (b), the simulated CO and HC emissions were in accordance with the trend of the measured date, which shows a peak value at the 74% load operation condition.

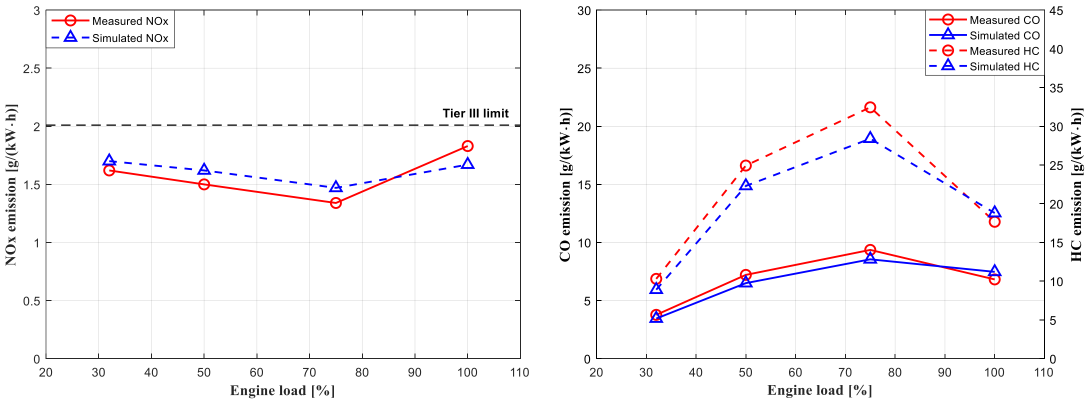

(a) NOx emissions

(b) CO and HC emissions

Figure 5.12 Simulated and measured emissions of the investigated engine at different operation conditions

It’s worth mentioning that in order to obtain an accurate CFD model, the spray model usually needs to be calibrated [149] by using experiment data like spray penetration, liquid length, vapor penetration, etc. But, the spray model in this study is not calibrated because the aforementioned experiment data is not available. However, the detailed injector geometry and measured injection parameters (pressure, duration, profile, mass) are provided, which help refine the spray model with sufficient input parameters. As the simulated diesel spray exhibits enough penetration distance without hitting the combustion chamber, the spray model is considered as qualitatively calibrated. In addition, the comparison with the experimentally obtained pressure, HRR and emissions proves the developed CFD model is with sufficient accuracy.

5.4 Chapter summary

The models setting up process (including layout, setup and calibration) of the proposed 0D/1D and 3D simulation models is introduced. A heat release analysis is performed with the measured in-cylinder for calibrating the 0D Wiebe combustion model. After validated by using experiment data, both the proposed 0D/1D and 3D simulation models prove to be capable of predicting the engine performance with sufficient accuracy, whilst the 3D simulation model can provide more detailed information including the heat release and emissions.

Chapter 6. Results and discussion

6.1 Chapter outline

Results derived from 3D simulation model are presented and discussed firstly, including the individual effects of the engine settings at 100% operation load and the parametric investigation at three operation conditions (1457 r/min, 1629 r/min and 1800 r/min). Subsequently, the obtained HRR from 3D simulation are employed for calibrating Wiebe combustion model by using Response Surface Methodology. Finally, the optimal solutions and sensitivity study of the engine setting optimisation are analysed.

6.2 Parametric investigation using the 3D model

6.2.1 Individual effect investigation at 100% operation load

(1) Effects of pilot injection timing

The 2-D simulation results with various pilot injection timings are shown in Figure 6.1. As seen from Figure 6.1 (a), (b) and (c), the maximum in-cylinder pressure, peak heat release rate (HRR) and maximum average temperature were found to increase with the advance of pilot injection timing. The heat release phase is advanced with a longer ignition delay due to lower temperature and pressure, as shown in Figure 6.1 (d). An abnormal sharp jump is spotted at the HRR curve for the case of –15 °CA pilot injection timing, which implies a potential knocking occurrence at the crank angle around 14 °CA ATDC. The mass fraction variation of OH and CH_2O radicals with different pilot injection timing is shown in Figure 6.1 (e) and (f). The OH radial is formed in high-temperature region, indicating the total reactivity of the combustion process [154]. The production and consumption rate of CH_2O radical play a dominant role in the low-temperature reaction regime of methane [149]. As the CH_2O radical is mainly distributed in front of the flame, it can be used as the precursor of oxidation reaction in dual fuel engines [145]. In Figure 6.1 (e) and (f), with the advance of the pilot injection timing, the formation starting time of OH and CH_2O radicals is advanced with an increasing production rate. The abovementioned abnormal sharp jump for the case of –15 °CA pilot injection timing can also be found in the mass fraction of the OH and CH_2O radicals, which can be inferred that the spontaneous combustion of methane caused a knocking combustion. The detailed information (location and timing) of the knocking occurrence will be revealed by the following 3D result analysis.

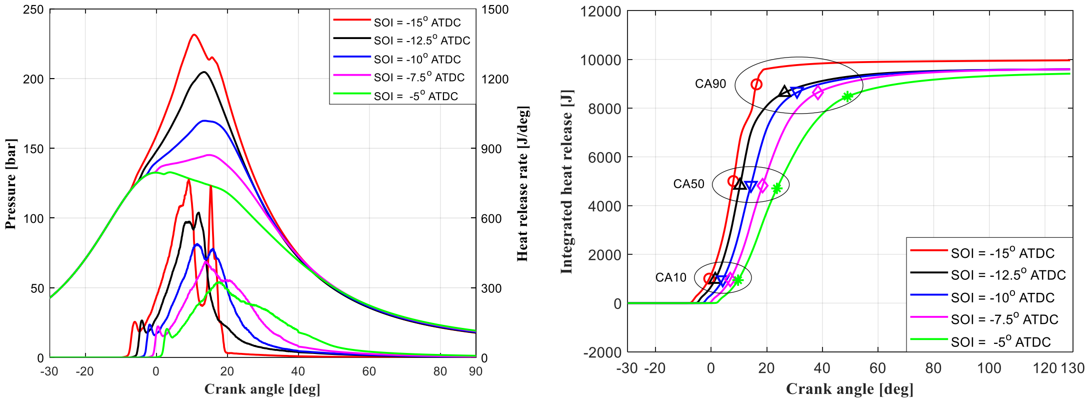

(a) In-cylinder pressure and heat release rate

(b) Integrated heat release

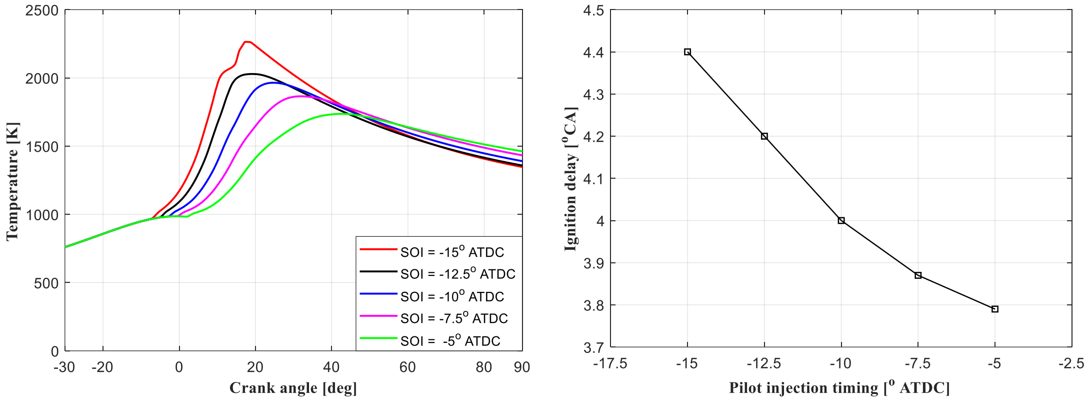

(c) In-cylinder temperature

(d) Ignigtion delay

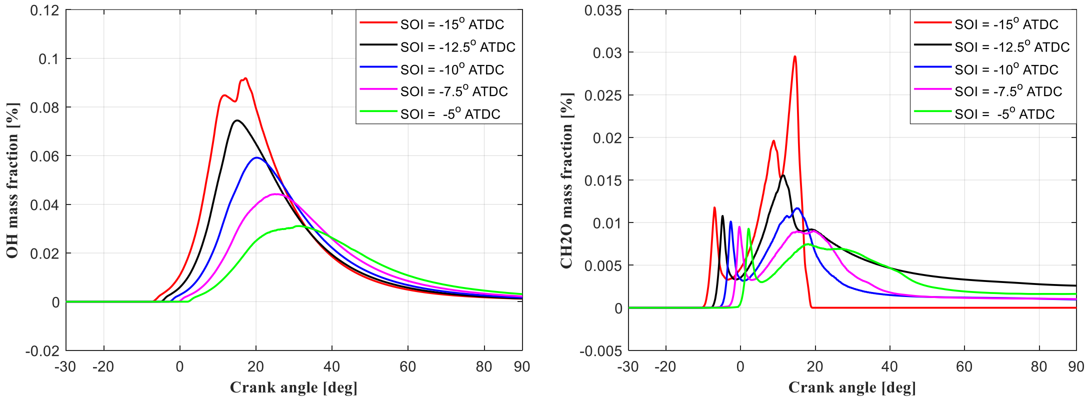

(e) OH mass fraction

(f) CH_2O mass fraction

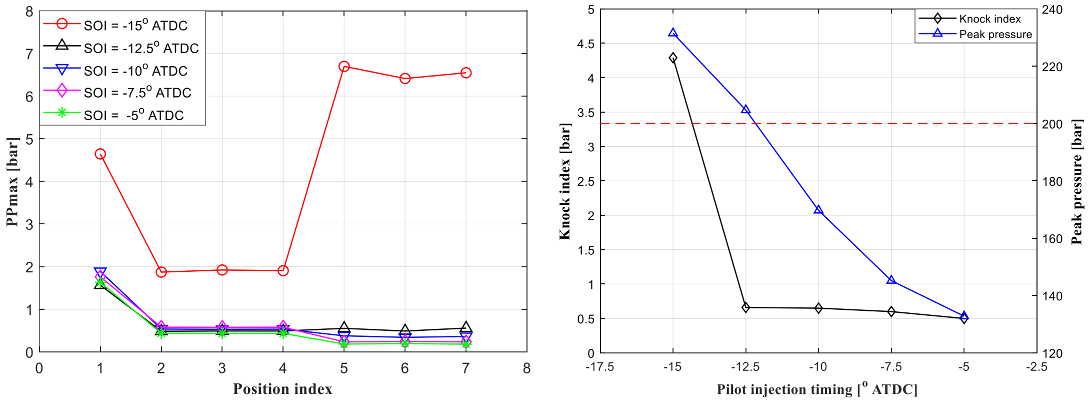

(g) PPmax (h) Knock index and peak pressure

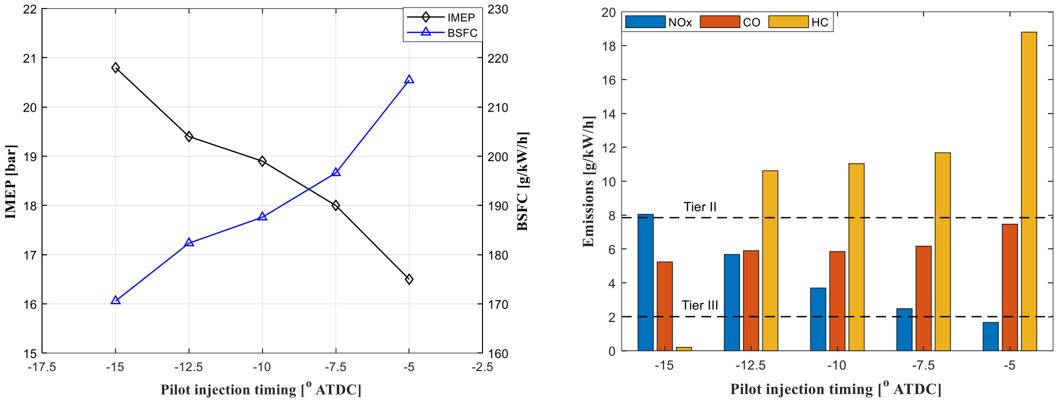

(i) IMEP and BSFC (j) Emissions

Figure 6.1 2D simulation result with different pilot injection timings

In Figure 6.1 (g) and (h), the PP_{max} and Knock Index increase slightly from –5 °CA to –12.5 °CA and show a dramatical jump at –15 °CA, implying a knocking occurrence. The peak pressure rises above the peak pressure limit (200 bar) at the pilot injection timing of –12.5 °CA and –15 °CA, which might cause severe damage to the cylinder structure and should be avoid by holding the pilot injection timing after –12.5 °CA. The Figure 6.1 (i) shows that the BSFC decreases with the pilot injection advance, while the IMEP presents a contrary trend. It can be explained that early injection of the pilot diesel increases the air-fuel mixing duration, which results in a higher concentration of the chemical reactive combustible mixture during the injection delay period. Once the combustion starts, there would be more ignition spots and higher flame propagation speed, leading to better combustion efficiency and lower BSFC. However, better combustion efficiency is associated with higher in-cylinder temperature, which results in increasing NOx emissions with the pilot injection advance. As shown in Figure 6.1 (j), the NOx emissions at all the cases except the baseline case stays higher than the Tier III limits, while the NOx emissions at –15°CA pilot injection even fails to meet the Tier II limits. The HC and CO emissions shows a decreasing trend with the advance of pilot injection timing, which can also be explained by the higher combustion efficiency.

For further understanding of the in-cylinder combustion process, the distribution of in-cylinder temperature with different starts of injection (SOI) is presented in Figure 6.2. The temperature profile provides a visual representation of the location of the high-temperature regions inside the combustion chamber, which is important for the analysis of the NOx emissions. As seen from Figure 6.2, the advanced pilot injection timing results in larger high-temperature areas, which justifies the NOx emissions increase with the advance of pilot injection timing shown in Figure 6.1 (j).

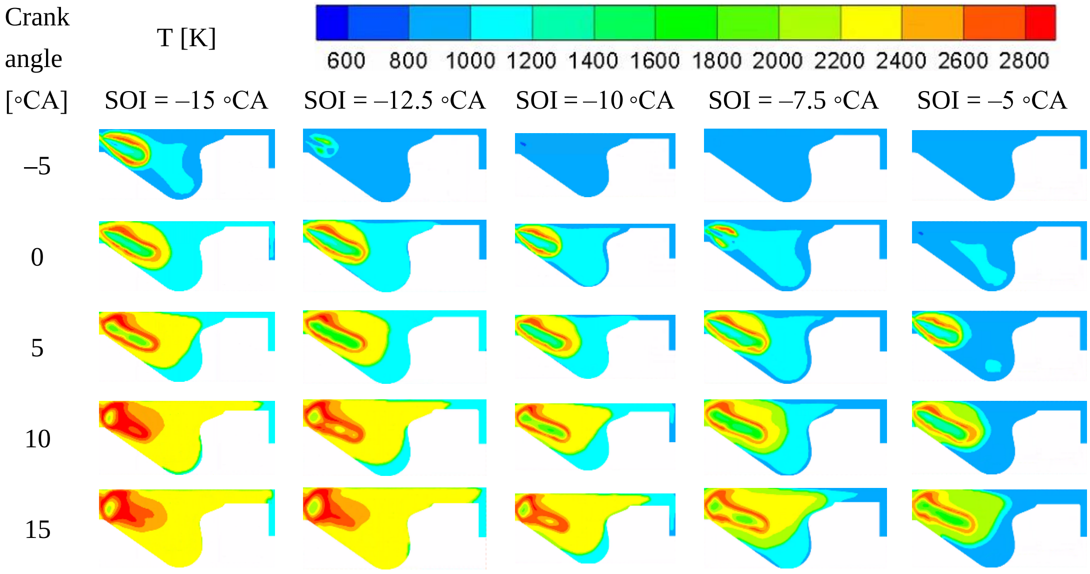

Figure 6.2 In-cylinder temperature distribution with different pilot injection timing

The distribution of CH_2O radical is shown in Figure 6.3, where the grey area denotes the 1800 K temperature contour representing the flame front. At the ignition stage, high concentration of CH_2O radical was spotted in the pilot spray zone because a portion of CH_4-air mixture was entrained into the spray zone and got involved in the low-temperature reaction of CH_4. Once the flame propagation starts, the CH_2O radical was mainly distributed in front of the flame, indicating the precursor of an oxidation reaction. With the advance of the pilot injection timing, the flame propagated further inside the combustion chamber, which resulted in advanced combustion phase and faster heat release rate. It is worth mentioning that high concentration of CH_2O radical was found in front of the flame at around 15 ◦CA for the case of –15◦CA SOI, which indicated a knocking occurrence and explained the high PP_{max} and KI shown in Figure 6.1 (g) and (h).

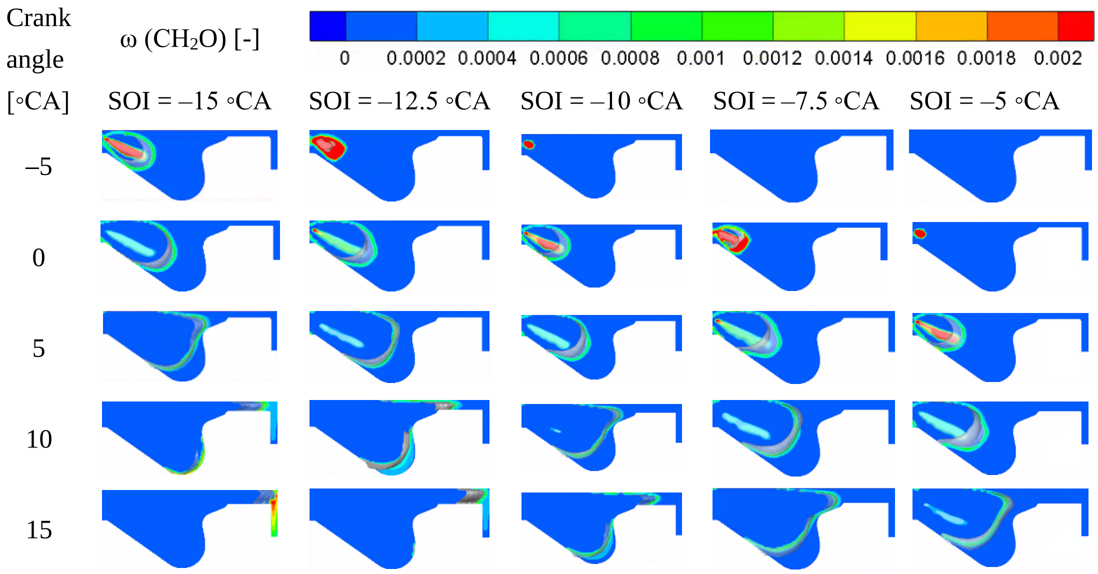

Figure 6.3 In-cylinder CH_2O distribution with different pilot injection timing

(2) Effects of equivalence ratio

Figure 6.4 shows the results of the 3D model, in specific, the presented parameters are plotted against crank angle for various values of the equivalence ratio. As seen from Figure 6.4 (a), (b) and (c), the maximum in-cylinder pressure increased for higher equivalence ratio divergence from its baseline value, which is caused by the increased initial pressure. The peak heat release rate and the maximum average temperature reduced with the equivalence ratio increase, exhibiting a contrary trend with the maximum in-cylinder pressure. The ignition was slightly advanced by around 1°CA when the air-NG equivalence ratio increased from 1.58 to 1.94 as shown in Figure 6.4 (d), which is attributed to the increase of the compression pressure and temperature. However, the HRR and the integrated HRR decreased with higher equivalence ratio values due to the slower chemical reaction rate caused by the dilution effect of more fresh air. The integrated HRR with +10% equivalence ratio difference was only 84.2% of that with –10% equivalence ratio difference, implying an incomplete combustion with +10% equivalence ratio difference. In Figure 6.4 (e), the increase of equivalence ratio caused a significant reduction of the total reaction reactivity, which was indicated by the peak value of the OH radical. The increasing end value of the CH_2O mass fraction in Figure 6.4 (f) proved that more CH_2O radicals were left unconsumed at EVO, leading to the higher HC emissions shown in Figure 6.4 (j).

In Figure 6.4 (g) and (h), the PP_{max} and Knock Index (KI) exhibited higher values with the increase of the equivalence ratio difference from –10% to +10%, indicating a stimulating effect on the knocking phenomenon. However, both the PP_{max} and KI dropped to a low level with the +10% equivalence ratio difference due to the incomplete combustion. The peak pressure shows an apparent increase from 125 bar to 147 bar, whilst all the predicted maximum pressure values are well below the peak pressure limit of 200 bar. Figure 6.4 (i) shows a significant increase in BSFC and a decrease in IMEP, which can be explained by the slower combustion rate with the increase of equivalence ratio. In Figure 6.4 (j), the NOx emissions reduced by increasing the equivalence ratio and started to meet with the Tier III regulations when the equivalence ratio exceeded its baseline value (positive equivalence ratio difference). The HC emissions exhibited a contrary trend to the NOx emissions, whilst the HC emissions achieved its lowest level at –10% equivalence ratio variation.

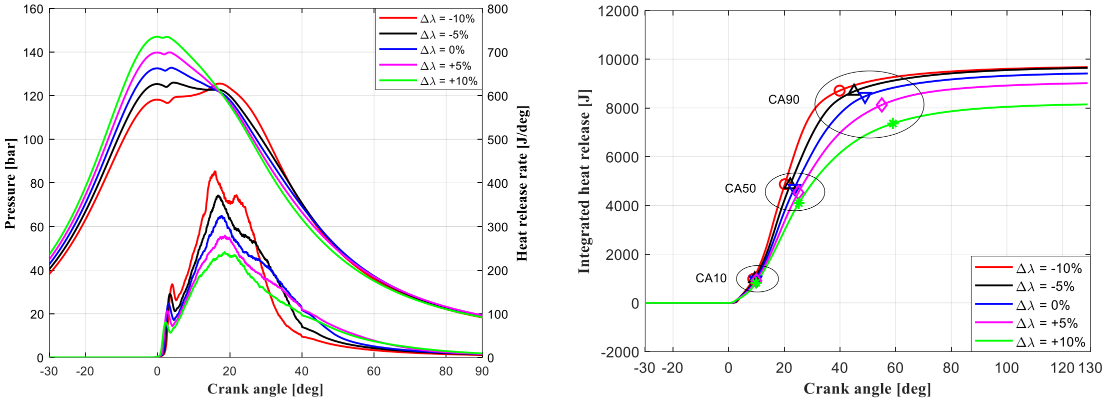

(a) In-cylinder pressure and heat release rate

(b) Integrated heat release

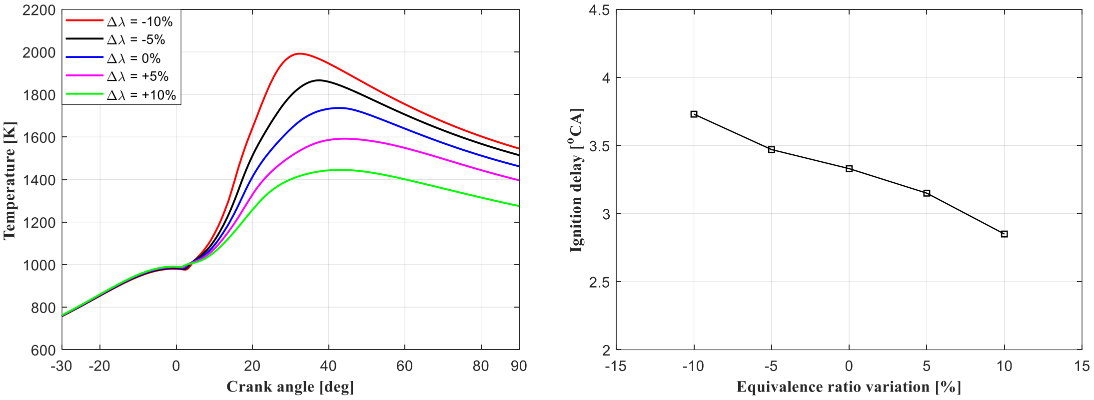

(c) In-cylinder temperature

(d) Ignition delay

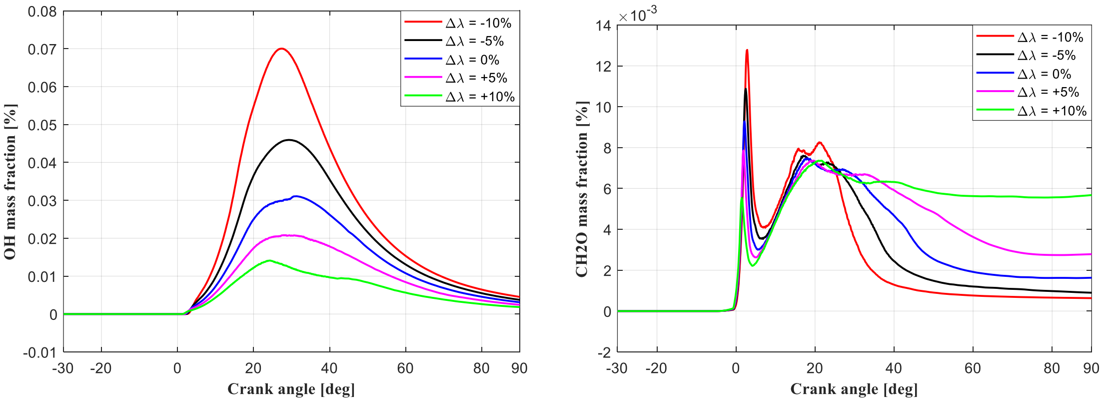

(e) OH mass fraction (f) CH$_2$O mass fraction

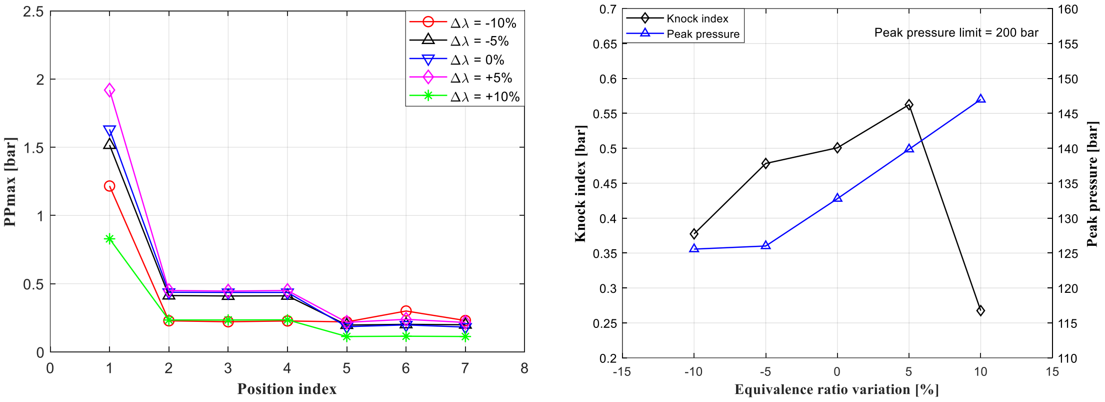

(g) PPmax (h) Knock index and peak pressure

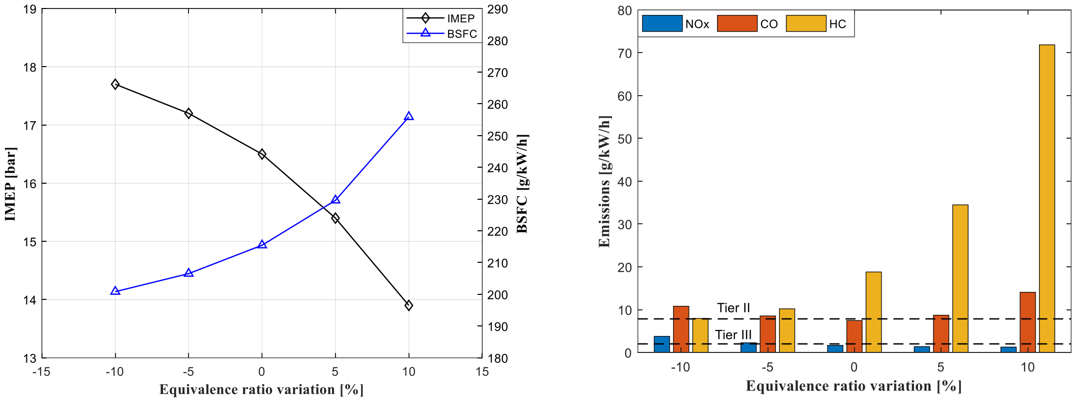

(i) IMEP and BSFC (j) Emissions

Figure 6.4 2D result with different equivalence ratio variations

Figure 6.5 presents the distribution of in-cylinder temperature with different equivalence ratio difference from its baseline value. With higher equivalence ratio values, the compression pressure at TDC (0◦CA) increases causing a larger high-temperature region (between 1000 K and 1200 K). However, larger equivalence ratio caused leaner air-fuel mixture, resulting in slower combustion speed. Thus, smaller area of high-temperature region (between 2000 K and 2800 K) was spotted after the flame starts propagating at higher equivalence ratio, which explains the NOx emissions reduction and the HC emissions increase shown in Figure 6.4 (j).

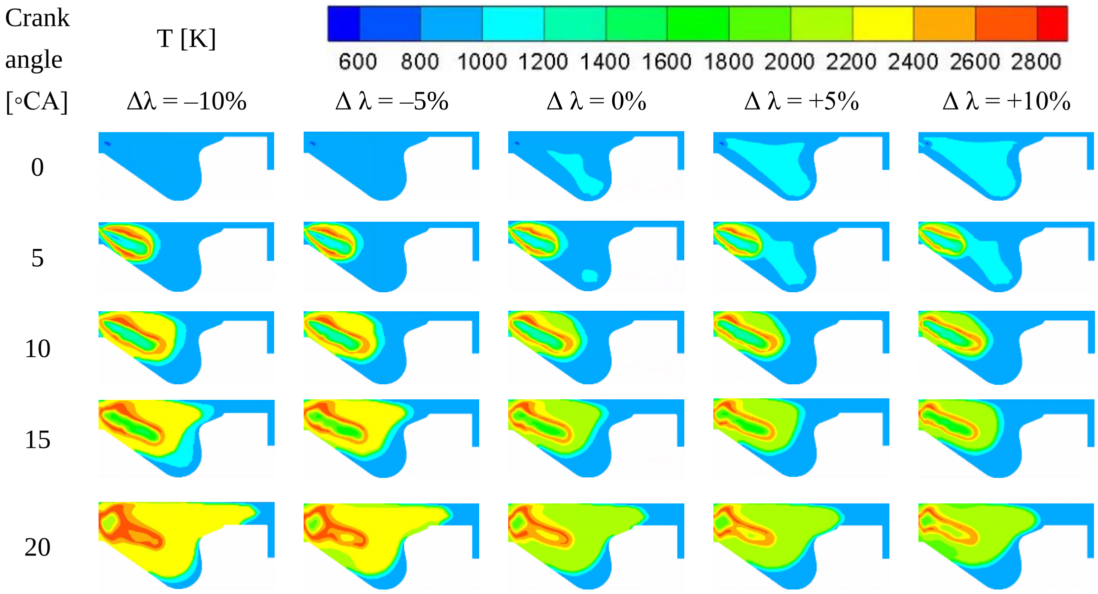

Figure 6.5 In-cylinder temperature distribution with different equivalence ratio variations

The distribution of CH_2O radical and 1800 K temperature contour are shown in Figure 6.6. As seen from the comparison at 5◦CA, the CH_2O radical concentration inside the spray zone is much higher than the remaining space, which means that low-temperature reaction plays dominant role inside the spray zone. The longer flame propagation distance indicated by the 1800 K temperature contour implies that flame propagates faster with smaller equivalence ratio.

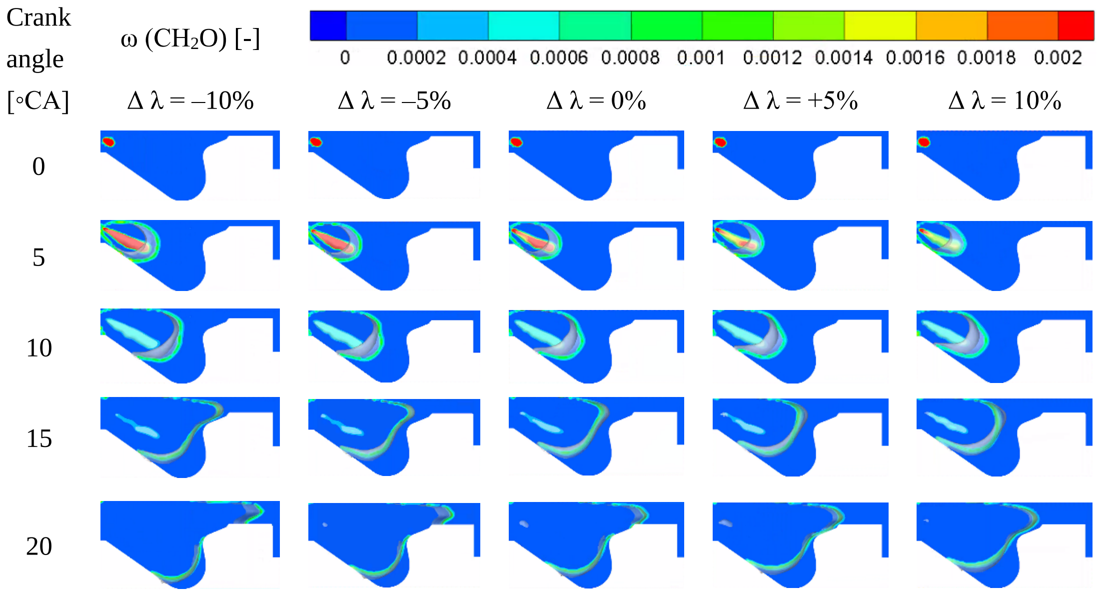

Figure 6.6 In-cylinder CH_2O distribution with different equivalence ratio variations

(3) Effects of natural gas mass

As seen from Figure 6.7 (a), (b), (c), (e) and (f), the NG mass increase did not make significant difference to the shape of the HRR, the combustion phase, the average temperature, as well as the mass fractions of OH and CH_2O radicals. The increase of the integrated HRR was attributed to the increase of the absolute NG mass. Besides, due to the increase of the compression pressure, higher peak pressure and shorter ignition delay were achieved with the NG mass increase, as shown in Figure 6.7 (a) and (d). The PP_{max}, KI, peak pressure and IMEP increased with higher NG mass variation, whilst the BSFC was reduced from 220 g/(kW·h) to 214 g/(kW·h). However, the maximum KI occurred at +5% NG mass variation. In Figure 6.7 (j), the emissions of NOx, HC and CO shared a slight downtrend with increasing the NG mass. In addition, the NOx emissions at all the investigated cases are well below the Tier III limit.

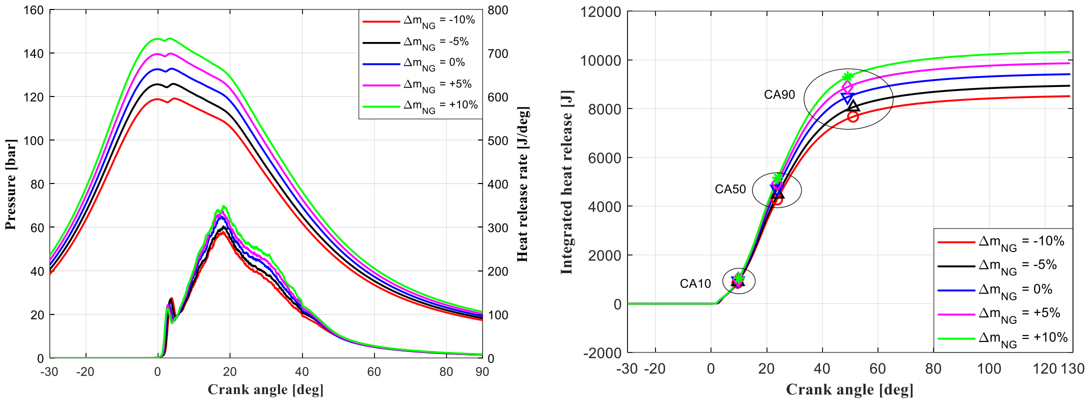

(a) In-cylinder pressure and heat release rate

(b) Integrated heat release

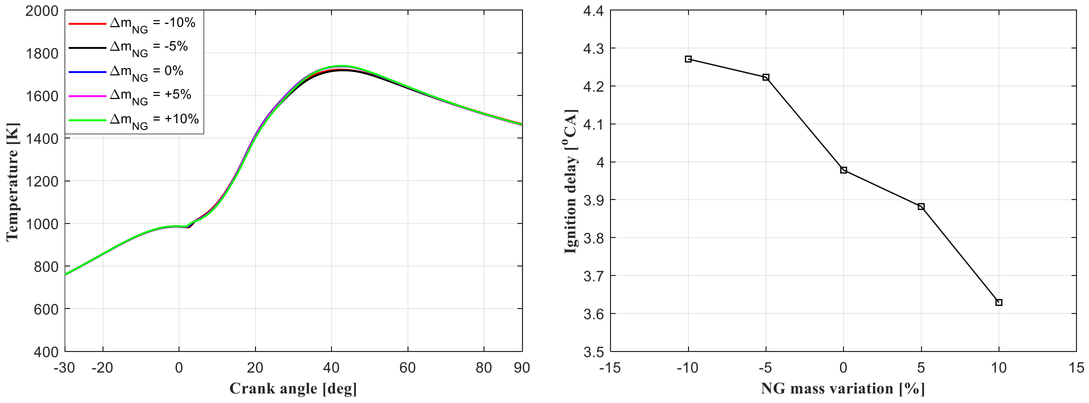

(c) In-cylinder temperature

(d) Ignition delay

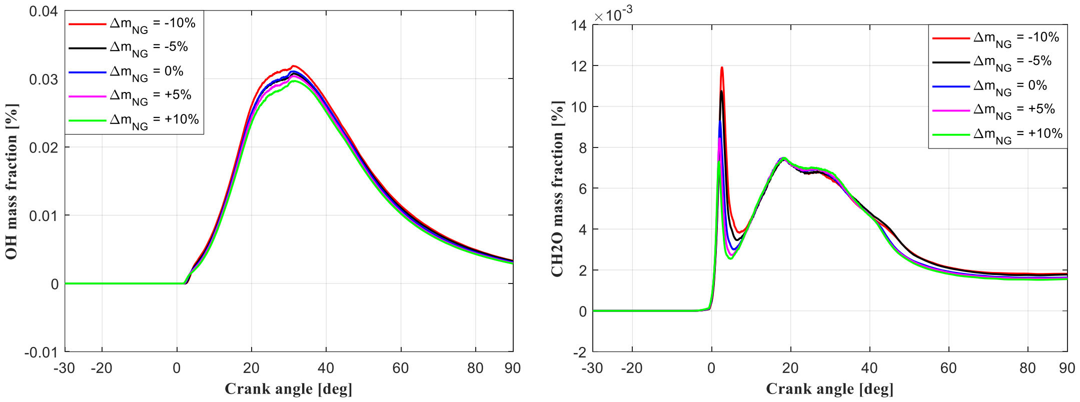

(e) OH mass fraction

(f) CH_2O mass fraction

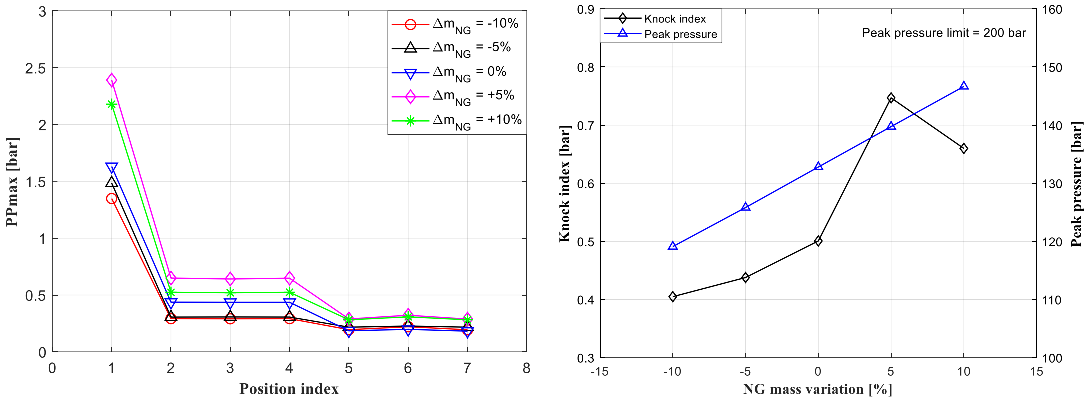

(g) PPmax

(h) Knock index and peak pressure

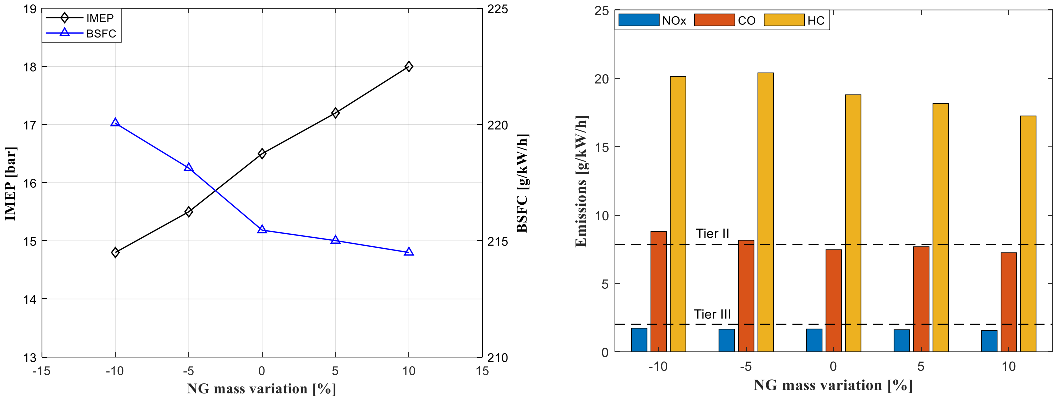

(i) IMEP and BSFC

(j) Emissions

Figure 6.7 2D result with different NG mass variations

Figure 6.8 presents the in-cylinder temperature distribution with different NG mass variations. When the NG mass increases, larger area of high-temperature zone (between 1000 K and 1200 K) was spotted at the TDC (0◦CA), which is caused by the increasing initial pressure and explains the shortening of the ignition delay in Figure 6.7 (d). However, after the flame propagation starts at around 5◦CA, the NG mass variation does not show an apparent effect on the in-cylinder temperature distribution, which is in accordance with the result indicated by the HRR and OH radical mass fraction.

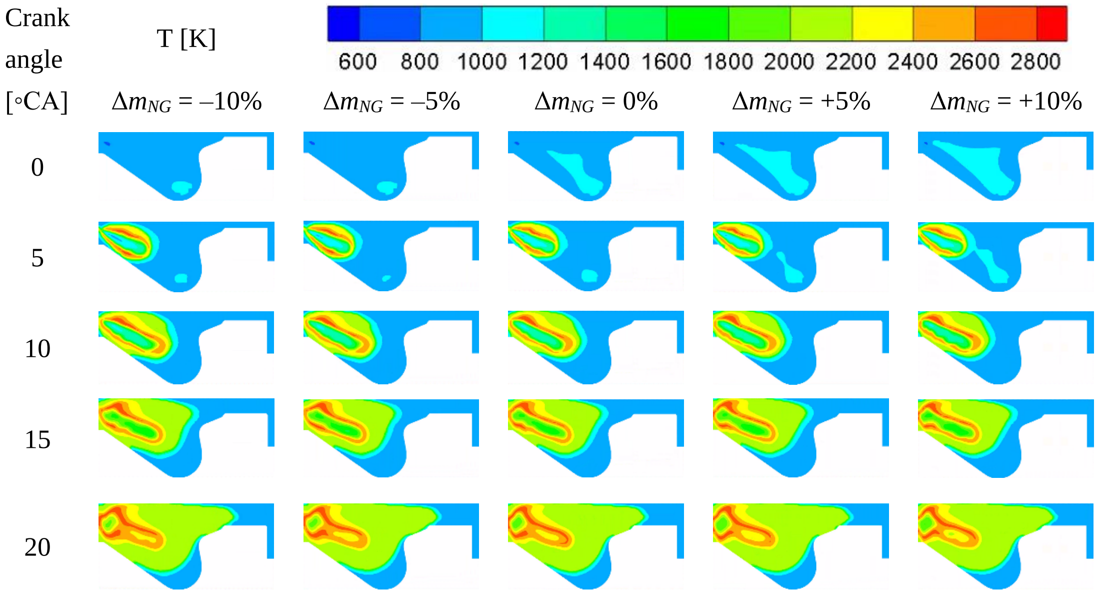

Figure 6.8 In-cylinder temperature distribution with different NG mass variations

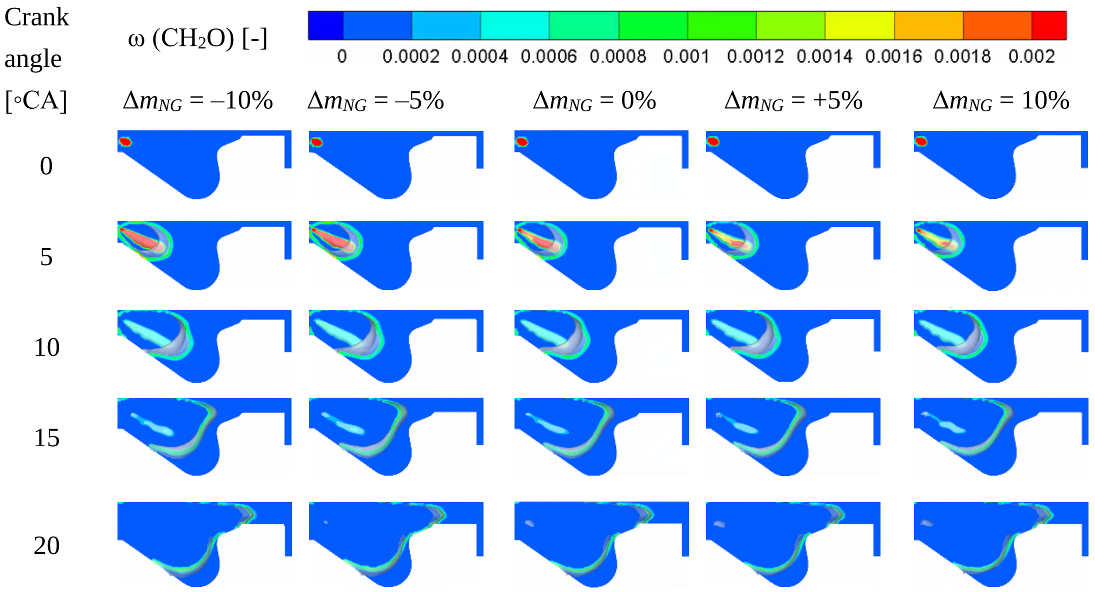

Figure 6.9 In-cylinder CH_2O distribution with different NG mass variations

The distribution of CH_2O radical with different NG mass variation is shown in Figure 6.9, where the grey area denotes the 1800 K temperature contour representing the flame front. At the initial flame propagation stage around 5◦CA ATDC, higher concentration of CH_2O radical was spotted with smaller NG mass, which indicates more CH_4 getting involved in the low-temperature reaction and justifies the higher first peak HRR in

Figure 6.7 (a). For the following flame propagation process, the NG mass variation does not make visible difference on the CH_2O distribution.

6.2.2 Parametric investigation at different operation loads

(1) Design of parametric run

Prior to performing the parametric run, the NOx-BSFC trend was analysed to determine the appropriate variation ranges of the involved operating settings which generate results located in the optimal area at three operation conditions. The NOx-BSFC optimal area is defined as the area where the derived BSFC is smaller than the baseline case while the NOx emissions meet the Tier III requirements. As mentioned in Section 4.3.1, the rotational speeds 1800 r/min, 1629 r/min and 1457 r/min will be used in the parametric run representing different operation conditions because the operation loads are no longer constant due to the involvement of NG mass variation as one of the operating settings.

Figure 6.10 presents the NOx emissions versus BSFC with different operating settings at 1800 r/min, 1629 r/min and 1457 r/min operation conditions. The NOx-BSFC trend at 1800 r/min can be obtained directly from the simulation results of the effect investigation at 100% load, as presented in previous section. As seen from Figure 6.10 (a), the NOx emissions increase with advanced pilot injection timing and reduced equivalence ratio at 1800 r/min, whilst the BSFC exhibits a contrary trend with NOx emissions. Thus, there is a trade-off between NOx emissions and BSFC when the pilot injection timing and the equivalence ratio vary at 1800 r/min. In addition, the predicted NOx emissions are higher than Tier III limit when the pilot injection timing is advanced ahead –7.5°CA or when the equivalence ratio variation is reduced smaller than –5%. On the other hand, a simultaneous reduction of NOx emissions and BSFC is achieved when the NG mass fraction increases from –10% to 10%, whilst NOx emissions under all the five variation levels are smaller than the Tier III limit. Thus, the cases of 5% and 10% NG mass fraction variation are the optimal solutions compared to the baseline case considering reducing BSFC and meeting Tier III regulation simultaneously. For the following parametric investigation, the maximum variation level of NG mass fraction could be increased to 20% because the influence of 10% NG mass fraction variation on the NOx-BSFC trend is relatively minor compared to the influence of the other two operating settings variations. As inferred from Figure 6.10 (a), the optimal area at 1800 r/min operating condition can be achieved by controlling the variation ranges of pilot injection timing, equivalence ratio variation and NG mass fraction variation within –5 to –7.5 °CA, –5% to +5% and 0% to +20%, respectively.

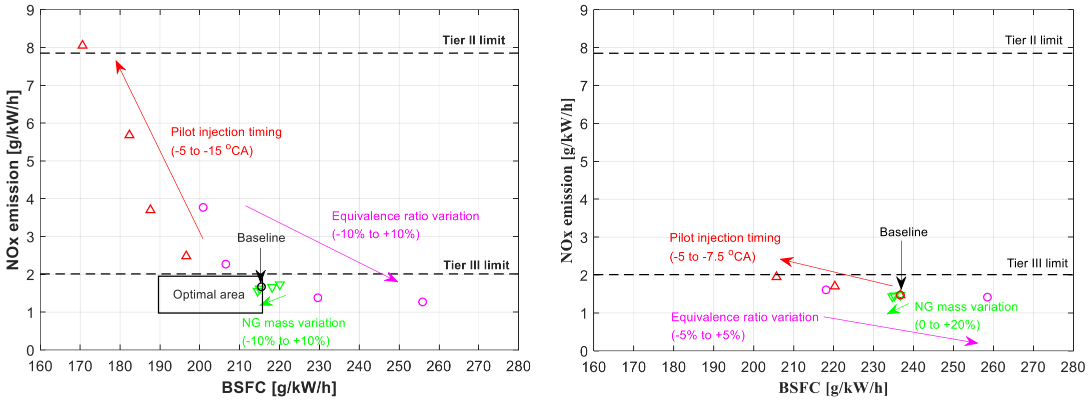

(a) 1800 r/min (b) 1629 r/min

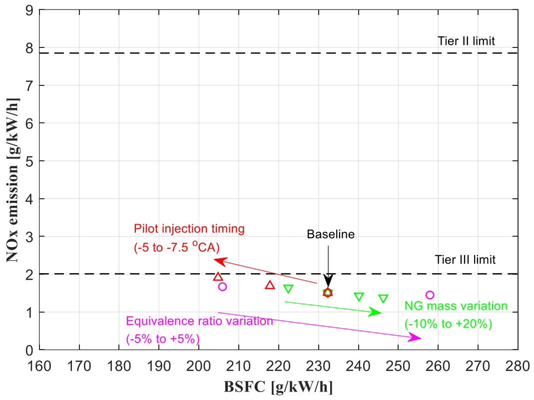

(c) 1457 r/min

Figure 6.10 NOx emissions versus BSFC with different operating settings at three operation conditions: 1800 r/min, 1629 r/min and 1457 r/min

The NOx-BSFC trends at 1629 r/min and 1457 r/min are shown in Figure 6.10 (b) and Figure 6.10 (c), respectively. In order to reduce the computational cost of CFD simulation cases, three levels rather than five levels of each operation settings are investigated first to check whether the variation ranges of optimal area at 1629 r/min and 1457 r/min operation conditions are the same with those at 1800 r/min. As seen from Figure 6.10 (b), the optimal area at 1629 r/min can be achieved by controlling operating settings variation ranges the same with those at 1800 r/min. On the other hand, Figure 6.10 (c) indicates a trade-off between NOx emissions and BSFC at 1457 r/min when NG mass fraction varies from 0% to 20%, which is apparently different from the simultaneous reduction of NOx emissions and BSFC at 1800 r/min and 1629 r/min. Thus, the –10% variation level of NG mass fraction is additionally investigated to explore the appropriate operating settings ranges achieving the optimal area at 1457 r/min. As seen from Figure 6.10 (c), the optimal area at 1457 r/min operation condition could be obtained by setting the pilot injection timing, equivalence ratio variation and NG mass fraction variation within the ranges of –5 to –7.5 °CA, –5% to +5% and –10% to +10%, respectively.

According to the preceding analysis, the level settings of the parametric run at 1800 r/min, 1629 r/min and 1457 r/min operation conditions are listed in Table 6.1. The level settings of pilot injection timing and equivalence ratio variation at 1800 r/min, 1629 r/min and 1457 r/min are the same: pilot injection timing (–7.5°CA, –6.25°CA and –5°CA), equivalence ratio variation (–5%, 0% and 5%). The levels of NG mass fraction variation at 1800 r/min and 1629 r/min are set to be 0, 10% and 20%, whilst those at 1457 r/min are –10%, 0% and 10%. The experiment design is performed by using the ‘full factorial’ method, which generates totally 27 simulation cases. Nevertheless, not all the 27 simulation cases are actually conducted because certain cases can be easily excluded from the optimal area by referring to the variation trend in Figure 6.10.

Table 6.1 Level settings of parametric run at three operation conditions

	Rotational speed (r/min)		Levels (-)	
Pilot injection timing (°CA)	1800, 1629, 1457	A1	A2	A3
		–7.5	–6.25	–5
Equivalence ratio variation (%)	1800, 1629, 1457	B1	B2	B3
		–5	0	5
NG mass fraction variation (%)		C1	C2	C3
	1800, 1629	0	10	20
	1457	–10	0	10

(2) Optimisation potential investigation

Figure 6.11 presents the trade-off between the NOx emissions and BSFC as well as the maximum average pressure at three operating conditions. As seen from Figure 6.11, the maximum pressures of all the presented points are below the peak pressure limit. By excluding points with NOx emissions higher than the Tier III limit (2.01 g/kW/h) or with maximum average pressure higher than the peak pressure limit (200 bar) as well as with knock occurrence, there are 11, 17 and 12 points that can be identified for a potential engine optimisation at 1800 r/min, 1629 r/min and 1457 r/min operation conditions, respectively. The variations of the derived NOx emissions and BSFC at three operation conditions are presented in Table 6.2, Table 6.3 and Table 6.4. As mentioned in Section 4.3.1, the involvement of NG mass variation causes an inevitable change to the operation load, thus the brake power variation is also included in Table 6.2, Table 6.3 and Table 6.4.

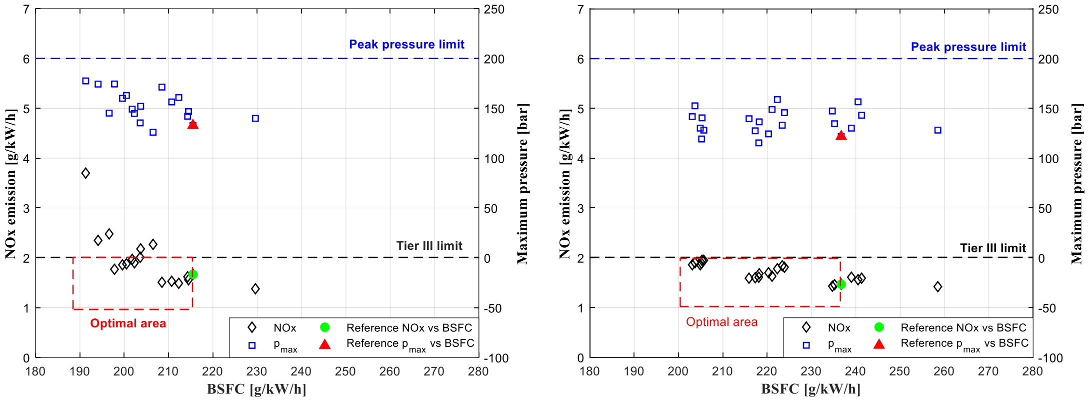

(a) 1800 r/min (b) 1629 r/min

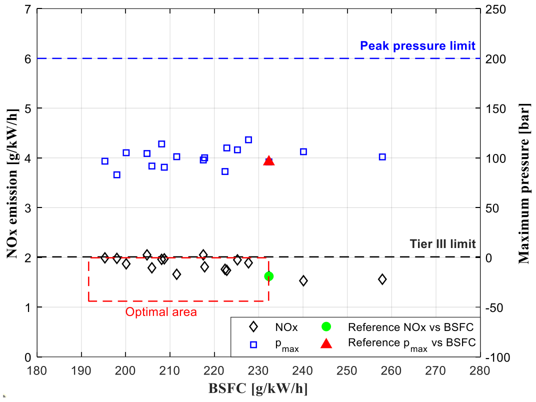

(c) 1457 r/min

Figure 6.11 Parametric study results showing potential for NOx emission and BSFC reduction at three operation conditions: 1800 r/min, 1629 r/min and 1457 r/min

Table 6.2 provides the 11 potential optimal solutions at 1800 r/min operation condition, which can be selected by the following criteria: (1) maximum simultaneous reduction of the BSFC and NOx emission; (2) maximum BSFC reduction and NOx emission equals or less than the Tier III limit; (3) maximum NOx emission reduction and BSFC equals or less than the reference value. As indicated by Table 6.2, there is no optimised point meeting the first criterion, namely achieving maximum reductions of BSFC and NOx emission at the same time. But point 7, 8, 9, 10 and 11 could provide a compromise by reducing BSFC and NOx emission simultaneously with different scales. For the second criterion, point 3 is the optimised case with –7.5 °CA pilot injection timing, +5%

equivalence ratio variation and +20% NG mass variation, resulting in the maximum reduction of 8.20% in BSFC and 5.98% increase in NOx emission. Nevertheless, the absolute NOx emission of point 3 (1.77 g/kW/h) is still below the Tier III limit (2.01 g/kW/h). The operating settings of point 11, which are –5 °CA pilot injection timing, 0% equivalence ratio variation and 20% NG mass variation, leads to the maximum reduction (10.78%) in NOx emission and minor reduction (1.48%) in BSFC. Thus, point 11 is the optimal solution for the third criterion. It’s worth mentioning that the brake powers of all the optimal points at 1800 r/min increase at a scale ranging from 0.56% to 29.00%. Point 7 provides the closest brake power (0.56% variation) to the baseline case and a simultaneous reduction of NOx emissions and BSFC.

Table 6.2 Optimal points obtained from the parametric run at 1800 r/min operation condition

No.	ID	SOI	$\Delta\lambda$	Δm_{NG}	ΔP_b	ΔNOx	ΔBSFC
-	-	°CA	%	%	%	%	%
0	Baseline	–5	0	0	-	-	-
1	A1B3C1	–7.5	+5	0	6.50	13.77	–6.13
2	A1B3C2	–7.5	+5	10	17.90	11.38	–7.38
3	A1B3C3	–7.5	+5	20	29.00	5.98	–8.20
4	A2B2C1	–6.25	0	0	5.80	20.11	–5.52
5	A2B2C2	–6.25	0	10	16.60	17.96	–6.36
6	A2B2C3	–6.25	0	20	27.26	12.57	–6.96
7	A2B3C1	–6.25	+5	0	0.56	–2.99	–0.56
8	A2B3C2	–6.25	+5	10	11.67	–8.38	–2.23
9	A2B3C3	–6.25	+5	20	22.38	–9.58	–3.25
10	A3B2C2	–5	0	10	9.69	–6.59	–0.46
11	A3B2C3	–5	0	20	20.18	–10.78	–1.48

The NOx and BSFC reductions of the 17 potential optimal solutions at 1629 r/min are presented in Table 6.3. As inferred from Table 6.3, only points 16 and 17 achieve simultaneous reductions of BSFC and NOx emissions whilst the BSFC reduction scales of these two points are very small (–0.6% and –0.9%, respectively) compared to those of other potential optimal points. The NOx emissions of the rest 15 points are higher than the reference case but still below the Tier III limit. The maximum BSFC reduction (–14.2%) is achieved at point 9, which is with +6.25°CA pilot injection timing, –5% equivalence ratio variation and +20% NG mass variation. The operating settings of point 17, which is –5 °CA pilot injection timing, 0% equivalence ratio variation and 20% NG mass variation, results in the maximum NOx reduction (–2.57%). The maximum increase of brake power (37.82%) is observed at point 9, which also provides the maximum BSFC reduction.

Table 6.3 Optimal points obtained from the parametric run at 1629 r/min operation condition

No.	ID	SOI	$\Delta\lambda$	Δm_{NG}	ΔP_b	ΔNOx	ΔBSFC
-	-	°CA	%	%	%	%	%
0	Baseline	–5	0	0	-	-	-
1	A1B2C1	–7.5	0	0	15.06	32.69	–13.09
2	A1B2C2	–7.5	0	10	25.84	32.52	–13.29
3	A1B2C3	–7.5	0	20	37.41	29.35	–13.96
4	A1B3C1	–7.5	5	0	5.98	25.23	–5.64
5	A1B3C2	–7.5	5	10	15.35	23.43	–5.41
6	A1B3C3	–7.5	5	20	25.89	21.13	–6.09
7	A2B1C1	–6.25	–5	0	15.35	28.26	–13.31
8	A2B1C2	–6.25	–5	10	26.08	26.60	–13.46
9	A2B1C3	–6.25	–5	20	37.82	26.62	–14.21
10	A2B2C1	–6.25	0	0	7.48	15.74	–6.96
11	A2B2C2	–6.25	0	10	18.38	14.44	–7.83
12	A2B2C3	–6.25	0	20	26.55	10.87	–6.58
13	A3B1C1	–5	–5	0	8.52	9.59	–7.85
14	A3B1C2	–5	–5	10	18.86	9.13	–8.20
15	A3B1C3	–5	–5	20	29.61	7.98	–8.78
16	A3B2C2	–5	0	10	9.82	–0.97	–0.64
17	A3B2C3	–5	0	20	19.25	–2.57	–0.86

Table 6.4 Optimal points obtained from the parametric run at 1457 r/min operation condition

No.	ID	SOI	$\Delta\lambda$	Δm_{NG}	ΔP_b	ΔNOx	ΔBSFC
-	-	°CA	%	%	%	%	%
0	Baseline	–5	0	0	-	-	-
1	A1B2C3	–7.5	0	10	21.57	21.11	–10.42
2	A1B3C2	–7.5	5	0	3.15	20.27	–3.06
3	A1B3C3	–7.5	5	10	11.11	16.39	–1.98
4	A2B1C2	–6.25	–5	0	18.96	23.04	–15.94
5	A2B1C3	–6.25	–5	10	26.42	15.30	–13.86
6	A2B2C1	–6.25	0	–10	1.42	21.76	–10.18
7	A2B2C2	–6.25	0	0	6.65	11.95	–6.24
8	A2B2C3	–6.25	0	10	13.55	7.49	–4.09
9	A3B1C1	–5	–5	–10	6.90	22.41	–14.78
10	A3B1C2	–5	–5	0	12.84	10.62	–11.38
11	A3B1C3	–5	–5	10	19.63	2.33	–8.97
12	A3B2C1	–5	0	–10	–4.85	8.74	–4.26

Table 6.4 provides the derived NOx and BSFC reductions of the 12 potential optimal solutions at 1457 r/min. As seen from Table 6.4, the NOx emissions of all the potential

optimal solutions are higher than that of reference case, thus there is no point meeting the first and third selection criterion. For the second criterion, point 4 is the optimised case with –6.25 °CA pilot injection timing, –5% equivalence ratio variation and 0% NG mass variation, resulting in the maximum BSFC reduction of 15.9% while the corresponding NOx emissions comply with the Tier III limit. The NOx emissions of all the optimal points are higher than the baseline case, thus there are no solution for the first and third criterion. In addition, most optimal points exhibit an increased brake power except point 12, which provides a simultaneous reduction of brake power and BSFC.

(3) Combustion characteristics analysis

Although several optimal solutions have been selected from the CFD parametric runs, the determined solutions might not be the most appropriate ones because the involved CFD simulation cases are quite limited. In order to perform the engine settings optimisation which requires hundreds of simulation runs, the time-saving and cost-effective 0D/1D simulation model need to be used. The heat release rate obtained from the CFD simulation will be employed to calibrate the 0D Wiebe combustion model.

Table 6.5 Combustion characteristic of the parametric run at 1800 r/min

No.	ID	CA10	CA50	CA90	Maximum HRR	Integrated heat release
-	-	°CA	°CA	°CA	J/deg	J
0	Baseline	9.7	23.6	49.0	349	9408
1	A1B3C1	7.3	20.0	41.1	411	9446
2	A1B3C2	7.3	19.8	39.6	424	10383
3	A1B3C3	7.5	19.9	38.8	473	11311
4	A2B2C1	8.4	21.1	43.0	387	9572
5	A2B2C2	8.4	21.0	42.1	431	10489
6	A2B2C3	8.6	21.0	41.1	472	11390
7	A2B3C1	8.6	22.4	47.4	341	9249
8	A2B3C2	8.8	22.5	46.1	373	10214
9	A2B3C3	8.8	22.2	45.1	417	11118
10	A3B2C2	10.0	24.0	49.1	367	10329
11	A3B2C3	10.1	24.0	49.1	403	11277

In Table 6.5, Table 6.6 and Table 6.7, five parameters are selected to characterise the combustion of the parametric runs at different loads. CA10, CA50 and CA90 are the crank angles corresponding to 10%, 50% and 90% of the integrated heat release, respectively. The maximum heat release rate (HRR) and integrated heat release (IHR) are key parameters indicating the combustion speed and combustion efficiency, respectively. Thus, CA10, CA50, CA90, maximum HRR and IHR are sufficient for determining the shape of a HRR curve, namely calibrating the Wiebe combustion model.

Table 6.6 Combustion characteristic of the parametric run at 1629 r/min

No.	ID	CA10	CA50	CA90	Maximum HRR	Integrated heat release
-	-	°CA	°CA	°CA	J/deg	J
0	Baseline	8.9	22.6	52.1	279	7463
1	A1B2C1	6.7	19.6	45.1	333	8210
2	A1B2C2	7.1	19.3	45.0	379	8946
3	A1B2C3	7.3	19.5	44.1	385	9744
4	A1B3C1	6.5	19.2	44.0	307	7483
5	A1B3C2	6.9	19.2	45.0	342	8136
6	A1B3C3	7.1	19.3	45.0	372	8871
7	A2B1C1	7.7	20.6	47.1	340	8424
8	A2B1C2	8.2	21.0	47.0	369	9209
9	A2B1C3	8.5	20.9	46.0	415	10032
10	A2B2C1	7.8	21.0	49.1	305	7851
11	A2B2C2	8.3	21.1	49.1	345	8630
12	A2B2C3	8.5	21.2	50.1	372	9251
13	A3B1C1	9.0	22.6	53.0	307	8185
14	A3B1C2	9.4	22.9	53.1	343	8959
15	A3B1C3	9.8	22.9	52.1	379	9752
16	A3B2C2	9.3	22.7	52.1	316	8193
17	A3B2C3	9.6	22.8	53.0	340	8901

Table 6.7 Combustion characteristic of the parametric run at 1457 r/min

No.	ID	CA10	CA50	CA90	Maximum HRR	Integrated heat release
-	-	°CA	°CA	°CA	J/deg	J
0	Baseline	7.7	21.3	51.0	203	5364
1	A1B2C3	5.2	19.0	45.1	238	6276
2	A1B3C2	4.8	18.4	43.1	196	5258
3	A1B3C3	4.9	18.8	43.0	193	5658
4	A2B1C2	6.9	20.4	52.1	223	6387
5	A2B1C3	6.9	20.8	52.1	253	6787
6	A2B2C1	6.8	19.5	49.1	213	5344
7	A2B2C2	6.4	20.0	48.0	209	5604
8	A2B2C3	6.3	20.3	48.1	215	5957
9	A3B1C1	8.9	21.2	55.1	234	5862
10	A3B1C2	8.3	21.8	55.0	221	6169
11	A3B1C3	8.0	22.3	54.1	228	6540
12	A3B2C1	8.1	20.9	51.1	213	5123

Figure 6.12 presents the variations of the CA50 and combustion duration with different pilot injection timings at three operation points. The combustion duration is the crank angle difference between CA90 and CA10. As seen from Figure 6.12, the retarded pilot injection timing results in a later CA50 crank angle and longer combustion duration, indicating a postponed combustion phase. The later CA50 position can be explained by the delayed combustion start caused by the retarded pilot injection timing. When the pilot injection timing is advanced, more air-fuel mixing time is allowed before the combustion start, resulting in faster combustion speed and thus shorter combustion duration.

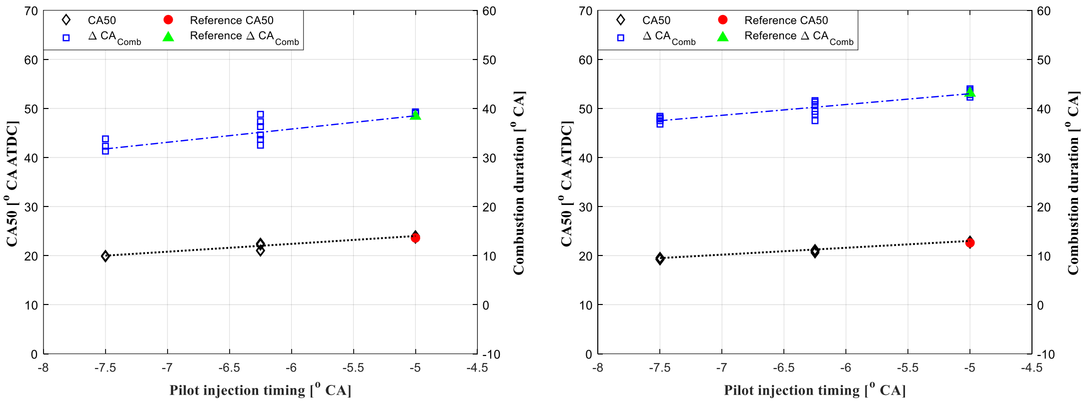

(a) 1800 r/min (b) 1629 r/min

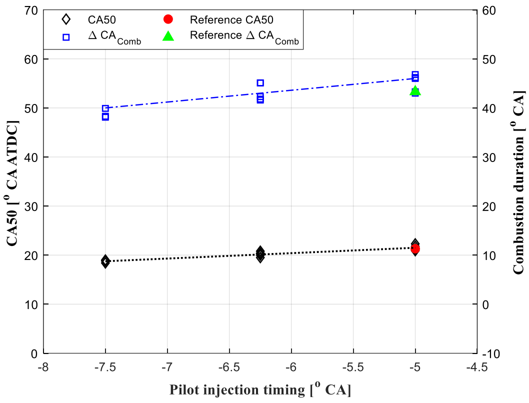

(c) 1457 r/min

Figure 6.12 CA50 and combustion duration with different pilot injection timings

The variation trends of the CA50 and combustion duration with the equivalence ratio variation are illustrated in Figure 6.13. As indicated by Figure 6.13, there is no optimal solution achieved at –5% equivalence ratio variation at 100% load. When the equivalence ratio increases, the overall reactivity would be reduced due to the leaner air-NG mixture. Nevertheless, advanced CA50 and shortened combustion duration are spotted at larger equivalence ratio divergence, indicating an improved combustion. It is inferred that the positive effect of the increased compression pressure on the combustion reactivity surpasses the negative effect of the leaner air-NG mixture.

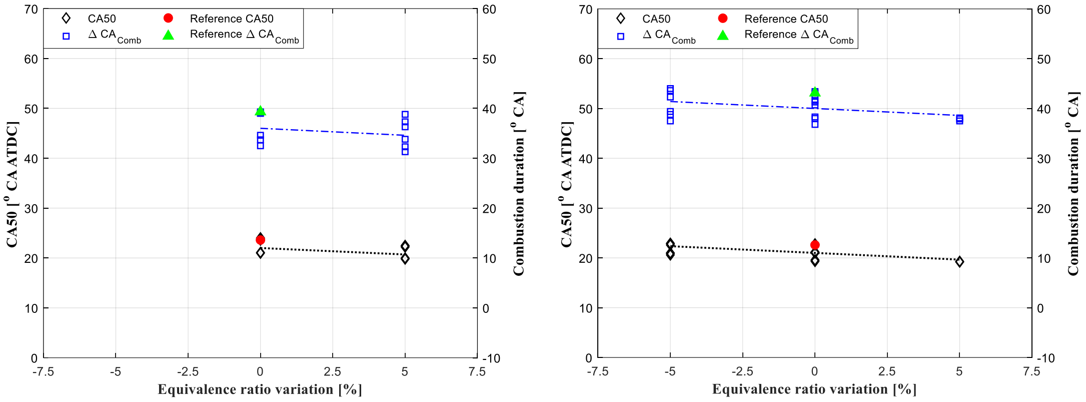

(a) 1800 r/min

(b) 1629 r/min

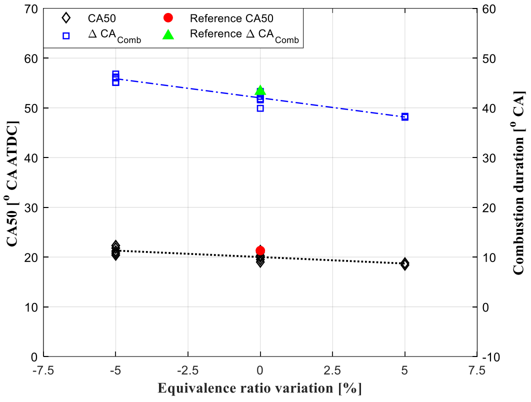

(c) 1457 r/min

Figure 6.13 CA50 and combustion duration with different equivalence ratio variations

Figure 6.14 shows the variations of CA50 and combustion duration with the natural gas mass variation. It is worth mentioning that the level settings of the NG mass variation at 1800 r/min and 1629 r/min are 0, 10% and 20%, whilst the level setting at 1457 r/min is –10%, 0 and 10%. As seen from Figure 6.14, the increase of NG mass variation leads to shorter combustion duration whilst the influence on CA50 is not significant. In the initial conditions setting of the 3D simulation model, the in-cylinder pressure at IVC is manually increased with the NG mass increase in order to keep a constant air-NG mass ratio, excluding the influence of equivalence ratio variation. Thus, the shorter combustion duration at larger NG mass can actually be justified by the higher reactivity caused by the increased compression pressure.

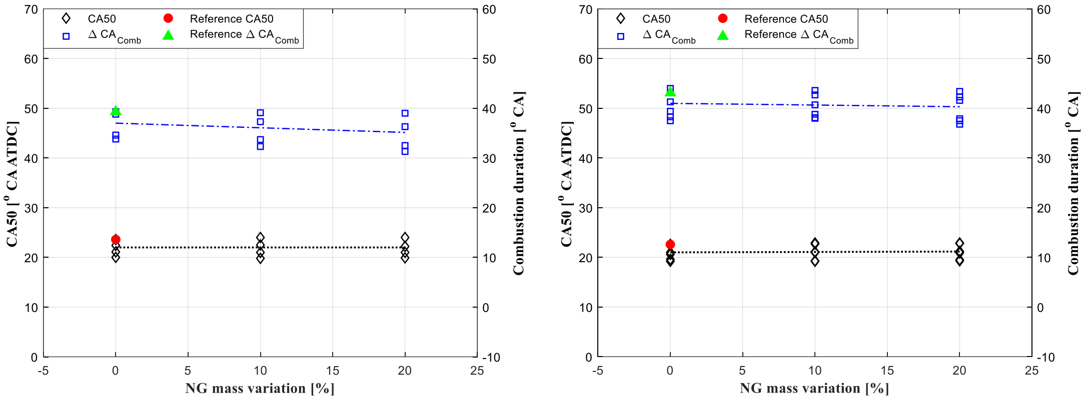

(a) 1800 r/min (b) 1629 r/min

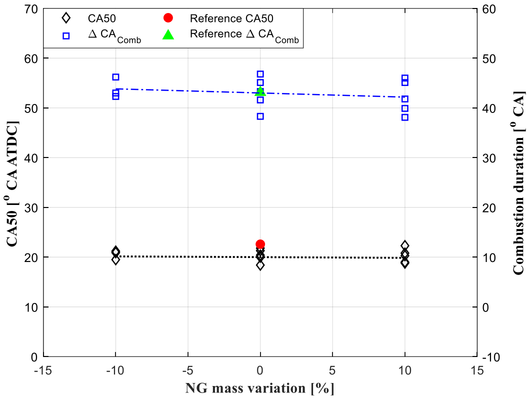

(c) 1457 r/min

Figure 6.14 CA50 and combustion duration with different NG mass variations

6.3 Wiebe combustion model calibration

6.3.1 Wiebe combustion parameters determining

Table 6.8 presents the fitted Wiebe combustion parameters by using double Wiebe functions and triple Wiebe functions. As seen from Table 6.8, the fitted SOC, b_1 and $\varDelta\varphi_1$ of Double Wiebe functions and Triple Wiebe functions are quite close to each other. The main combustion stage duration of Double Wiebe functions ($\varDelta\varphi_2$) is almost the same with that of Triple Wiebe functions ($\varDelta\varphi_3$). In addition, the fitting R-squares of Double Wiebe functions remain larger than 0.97 but slightly smaller than that of Triple Wiebe functions at all the three operation conditions.

The fitted Wiebe combustion parameters in Table 6.8 are then applied to simulate the HRR of the proposed 0D/1D model for comparing the predicted and measured in-cylinder pressure, as shown in Figure 6.15. As seen from Figure 6.15 (a), (c) and (e), the simulated HRR by using Triple Wiebe functions perform better in coinciding with the experimentally obtained HRR at all three operation conditions. On the other hand,

Figure 6.15 (b), (d) and (f) indicate similar conclusion that the simulation model employing Triple Wiebe function works better in predicting in-cylinder pressure. Nevertheless, the difference between the predicted pressure using the Double Wiebe function and the measured pressure is not significant.

Table 6.8 Wiebe parameters fitted by using double Wiebe and triple Wiebe functions

				1st			2nd			3rd		
Rotational speed	Wiebe function	SOC	b_1	m_1	$\Delta\varphi_1$	b_2	m_2	$\Delta\varphi_2$	b_3	m_3	$\Delta\varphi_3$	R^2
r/min	-	°CA	-	-	°CA	-	-	°CA	-	-	°CA	-
1800	Double	1.8	0.02	3.39	5.3	0.98	0.82	78.4	-	-	-	0.97
	Triple	1.8	0.03	2.29	6.2	0.79	1.11	57.9	0.18	3.43	78.4	0.99
1629	Double	1.9	0.04	3.23	6.0	0.96	0.80	78.2	-	-	-	0.98
	Triple	1.9	0.05	2.62	6.6	0.83	1.07	60.9	0.12	4.18	78.4	0.99
1457	Double	2.0	0.07	4.00	6.7	0.93	0.75	74.1	-	-	-	0.98
	Triple	2.1	0.09	3.40	7.1	0.79	1.03	57.1	0.12	3.82	77.4	0.99

Considering the final engine settings optimisation will be evaluated by engine performance rather than HRR, a quantitative comparison of the predicted and measured p_{max}/IMEP is presented in Table 6.9. As deduced from Table 6.9, the maximum relative errors of p_{max} and IMEP are 1.38% and 2.92% when Double Wiebe functions are used, whilst those are 0.73% and 2.25% when Triple Wiebe functions are employed. Although the prediction accuracy of Double Wiebe functions is slightly lower than that of Triple Wiebe functions, Double Wiebe functions are considered to be sufficient for characterizing the 0D combustion model of DF engines.

Table 6.9 Relative errors between the predicted and measured p_{max} and IMEP

	Combustion model	Indicator	Rotational speed [r/min]		
			1800	1629	1457
Relative error [%]	Double Wiebe functions	p_{max}	0.21	0.53	1.38
		IMEP	2.92	2.27	2.45
	Triple Wiebe functions	p_{max}	0.15	0.23	0.73
		IMEP	2.25	1.40	1.45

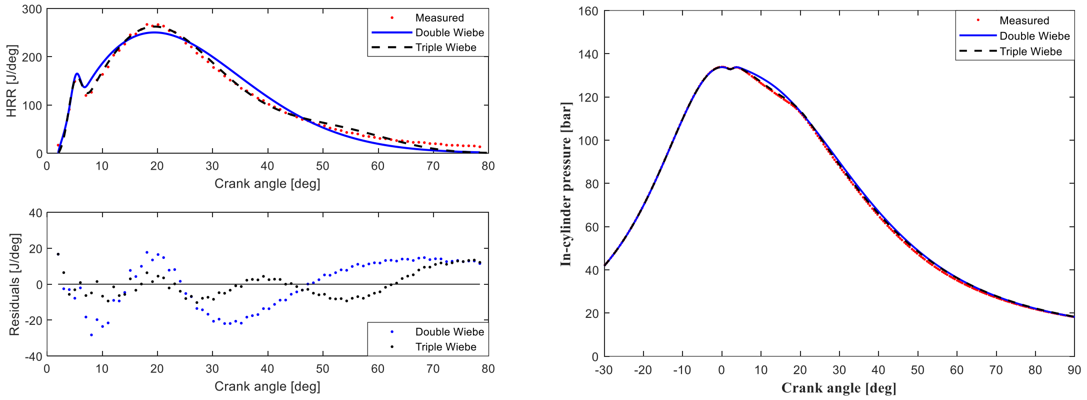

(a) HRR at 1800 r/min (b) In-cylinder pressure at 1800 r/min

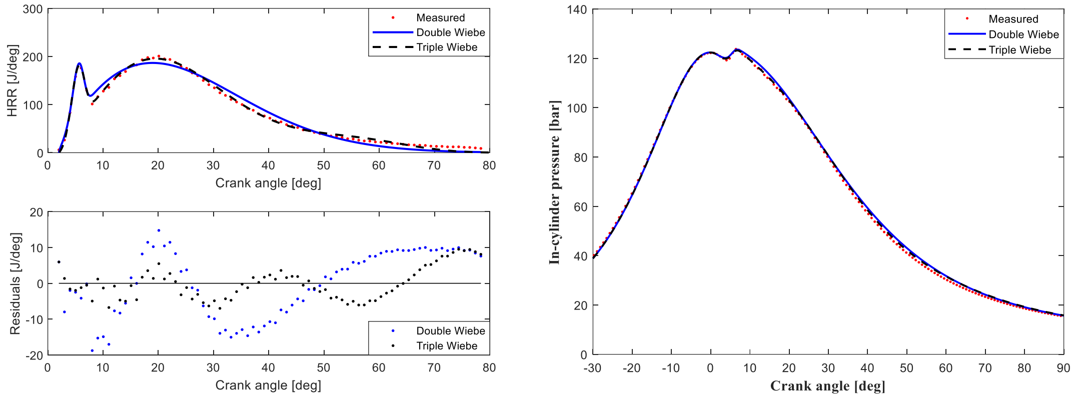

(c) HRR at 1629 r/min (d) In-cylinder pressure at 1629 r/min

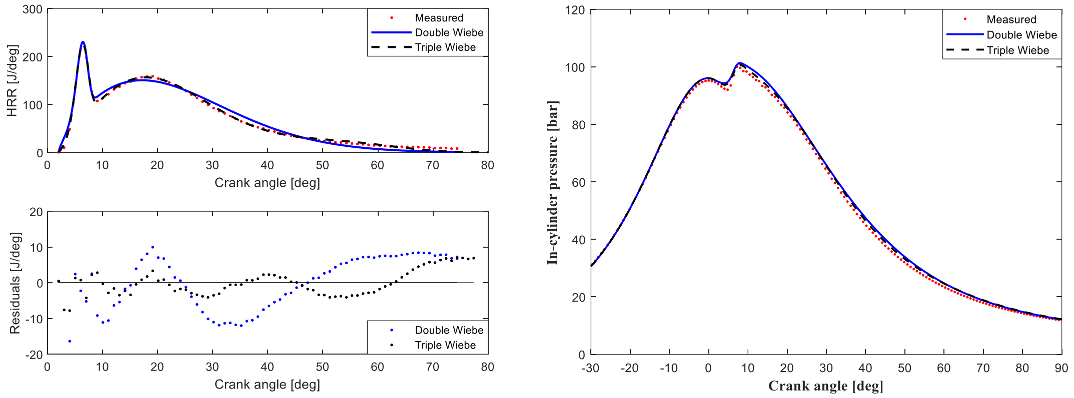

(e) HRR at 1457 r/min (f) In-cylinder pressure at 1457 r/min

Figure 6.15 HRR and pressure comparison by using Double Wiebe functions and Triple Wiebe functions at three operation conditions: 1800 r/min, 1629 r/min and 1457 r/min

6.3.2 Wiebe combustion parameters fitting

The fitting results of the linear and quadratic response models for the Wiebe combustion parameters at 1800 r/min are presented in Table 6.10 and Table 6.11, respectively. The good of fitness is evaluated by Root Mean Square Error (RMSE), the correlation coefficient (R^2) and adjusted correlation coefficient (R^2-adjust). In this study, the R^2

and R^2-adjust are considered within acceptable range when the values are larger than 0.9. As seen from Table 6.10, R^2 and R^2-adjust for almost all the Wiebe combustion parameters are close to 1 and within the acceptable range except for m_1 and $\Delta\varphi_1$. Table 6.11 indicates that R^2 and R^2-adjust of the quadratic response model are averagely closer to 1 compared to the linear response model, whilst the R^2-adjust for b_2 and m_1 are not within acceptable range.

Table 6.10 Linear response model for Wiebe combustion parameters at 1800 r/min

		SOC	b_2	m_1	m_2	$\Delta\varphi_1$	$\Delta\varphi_2$
		°CA	-	-	-	°CA	°CA
Fitted coefficients	*C*	6.22	1.00	1.59	0.22	0.78	121.28
	a	0.89	0.00	0.10	–0.13	–0.52	9.04
	b	–6.01	0.11	0.18	–2.43	–16.68	201.93
	c	–2.89	0.03	–1.87	0.58	–1.29	–15.78
Good of fitness	RMSE	0.10	0.00	0.06	0.02	0.15	0.97
	R^2	0.99	0.96	0.92	0.98	0.89	0.98
	R^2-adjust	0.99	0.94	0.89	0.97	0.85	0.98

Table 6.11 Quadratic response model for Wiebe combustion parameters at 1800 r/min

		SOC	b_2	m_1	m_2	$\Delta\varphi_1$	$\Delta\varphi_2$
		°CA	-	-	-	°CA	°CA
Fitted coefficients	*C*	8.00	0.99	1.47	0.27	4.29	127.97
	a	1.50	0.00	0.06	–0.12	0.48	11.07
	b	0.00	0.00	0.00	0.00	0.00	0.00
	c	–2.34	0.04	–3.09	–0.38	–13.25	15.50
	d	1.13	–0.02	–0.14	0.36	2.09	–33.22
	e	0.11	0.00	–0.04	–0.16	–2.17	4.72
	f	10.42	–0.01	–6.92	–1.73	–36.20	–57.00
	g	0.05	–0.00	–0.00	0.00	0.07	0.13
	h	0.00	0.00	0.00	0.00	0.00	0.00
	i	–0.74	–0.01	5.70	0.03	–3.61	–1.75
Good of fitness	RMSE	0.13	0.00	0.07	0.01	0.04	0.40
	R^2	0.99	0.96	0.95	0.99	1.00	0.99
	R^2-adjust	0.98	0.88	0.86	0.98	0.99	0.99

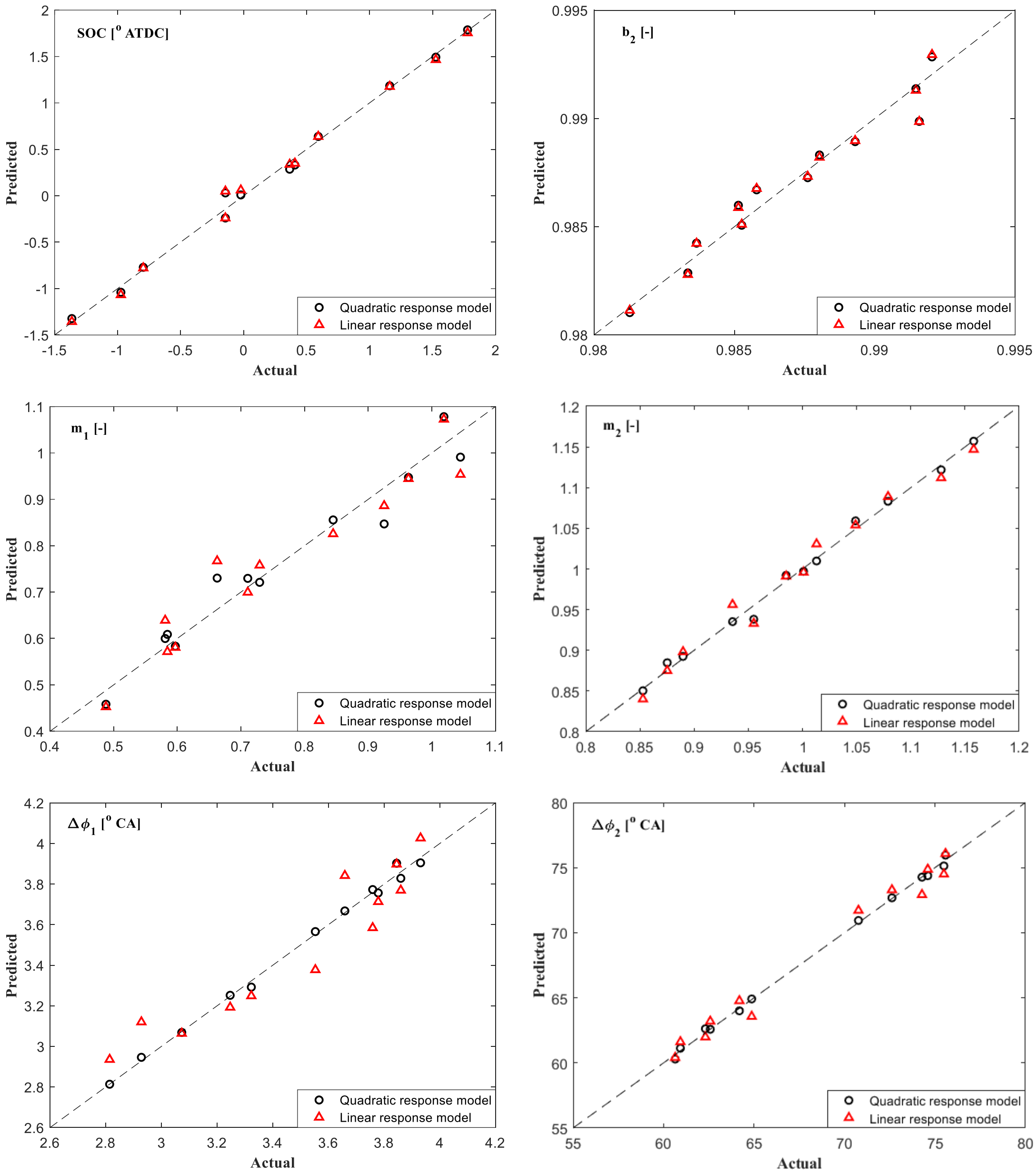

Figure 6.16 Predicted vs. actual Wiebe parameters at 1800 r/min operation condition

Figure 6.16 shows the correlation between the predicted and actual Wiebe parameters at 1800 r/min operation condition. As seem from Figure 6.16, the prediction accuracy of quadratic response model is higher than that of the linear response model as the predicted versus actual values of the quadratic response model distribute closer to the 45° line, especially for cases of m_1 and $\varDelta\varphi_1$. However, most of the data are located around the 45° line, indicating an excellent correlation between the predicted and actual values for both the linear response model and quadratic response model at 1800 r/min.

Table 6.12 Wiebe combustion parameters fitted by using linear response model at three operation conditions: 1800 r/min, 1629 r/min and 1457 r/min

Rotational speed			SOC	b_2	m_1	m_2	$\Delta\varphi_1$	$\Delta\varphi_2$
r/min			°CA	-	-	-	°CA	°CA
1800	Fitted coefficients	C	6.22	1.00	1.59	0.22	0.78	121.28
		a	0.89	0.00	0.10	–0.13	–0.52	9.04
		b	–6.01	0.11	0.18	–2.43	–16.68	201.93
		c	–2.89	0.03	–1.87	0.58	–1.29	–15.78
	Good of fitness	RMSE	0.010	0.00	0.06	0.03	0.15	0.97
		R^2	0.99	0.96	0.92	0.98	0.89	0.98
		R^2-adjust	0.99	0.94	0.90	0.97	0.85	0.98
	F-value	x_1	409.75	60.83	12.96	287.24	56.38	406.77
		x_2	14.85	60.93	0.03	86.55	46.53	162.28
		x_3	73.15	98.23	73.28	106.36	5.90	21.13
1629	Fitted coefficients	C	7.47	0.98	2.53	0.48	3.92	94.60
		a	0.98	0.00	0.10	–0.05	–0.02	3.59
		b	–3.61	–0.01	–5.31	0.43	–2.36	–15.20
		c	–1.95	0.03	–5.02	0.50	–3.21	–19.33
	Good of fitness	RMSE	0.04	0.00	0.51	0.02	0.12	1.06
		R^2	1.00	0.78	0.93	0.96	0.87	0.96
		R^2-adjust	0.99	0.73	0.91	0.96	0.84	0.95
	F-value	x_1	9217.00	2.91	4.64	108.76	0.23	138.44
		x_2	142.45	0.59	16.48	10.83	5.44	2.82
		x_3	361.88	41.57	128.70	127.45	87.80	39.75
1457	Fitted coefficients	C	7.48	0.96	4.93	0.52	6.55	86.72
		a	1.00	0.00	0.12	–0.02	0.16	1.93
		b	–4.00	–0.13	–10.52	0.67	–5.94	–43.27
		c	–1.06	0.02	–6.50	–0.04	–9.51	31.29
	Good of fitness	RMSE	0.05	0.00	0.24	0.02	0.41	1.49
		R^2	1.00	0.91	0.93	0.86	0.87	0.88
		R^2-adjust	0.99	0.88	0.90	0.82	0.82	0.83
	F-value	x_1	2373.20	2.55	1.28	7.13	0.77	8.59
		x_2	61.56	49.90	15.38	9.51	1.72	6.90
		x_3	30.04	9.99	40.50	0.24	30.43	24.94

The Wiebe combustion parameters fitted by using linear response model at 1800 r/min, 1629 r/min and 1457 r/min are presented in Table 6.12. The F-value is employed to represent the analysis of variance (ANOVA); the variables with larger F-value exhibit more significant effect on the corresponding responses. A glance at Table 6.12 reveals that the pilot injection timing has a significant effect on *SOC*, m_2, $\Delta\varphi_1$ and $\Delta\varphi_2$ while the rest two Wiebe combustion parameters b_2 and m_1 are primarily affected by the NG mass at 1800 r/min. At 1629 r/min operation condition, the pilot injection timing still depends on *SOC* and $\Delta\varphi_2$, whilst the rest Wiebe parameters are significantly influenced by the NG mass. At 1457 r/min operation condition, b_2 and m_2 are mainly determined by equivalence ratio while m_1, $\Delta\varphi_1$ and $\Delta\varphi_2$ are dominated by the NG mass. The determining factor of the SOC at 1457 r/min is the same with that at the other two loads, namely the pilot injection timing. As to the prediction accuracy, the R^2 and R^2-adjust for most of the Wiebe combustion parameters at different operating points are larger than 0.9 and within the acceptable range, whilst there are still a number of Wiebe parameters with R^2-adjust between 0.7 and 0.9. Thus, the prediction accuracy of the linear response model needs to be further verified by using the predicted in-cylinder pressure and engine performance.

Table 6.13 Relative errors between the predicted and measured values by using linear response model

	Rotational speed	r/min	1800		1629		1457	
			Case 1	Case 2	Case 3	Case 4	Case 5	Case 6
Relative errors	HRR_{max}	%	10.86	10.65	10.56	10.46	6.32	1.77
	IHR	%	0.10	0.10	0.11	0.10	0.12	0.10
	p_{max}	%	0.23	0.18	0.03	0.42	1.53	1.24
	IMEP	%	2.39	2.06	2.86	2.72	2.31	2.62

The calculated HRR by using linear response model is applied to the proposed 0D/1D model for simulating the in-cylinder pressure at 1800 r/min, 1629 r/min and 1457 r/min operation conditions. For each operating point, 2 cases are randomly selected from Table 6.2, Table 6.3 and Table 6.4 for verifying the prediction accuracy of the linear response model. The predicted HRR and in-cylinder pressure are compared to the CFD simulation results, as shown in Figure 6.17. The corresponding relative errors of maximum HRR, integrated heat release (IHR), maximum pressure and IMEP are presented in Table 6.13. As deduced from Figure 6.17 and Table 6.13, the relative errors between the predicted HRR_{max} and CFD simulated HRR_{max} are as large as 10.86%, whilst the relative errors of other indicators (IHR, p_{max} and IMEP) are smaller than 3%. Considering the engine settings optimisation will be evaluated by engine performance, a linear response model is with sufficient accuracy for calibrating the Wiebe combustion model of the investigated DF engine.

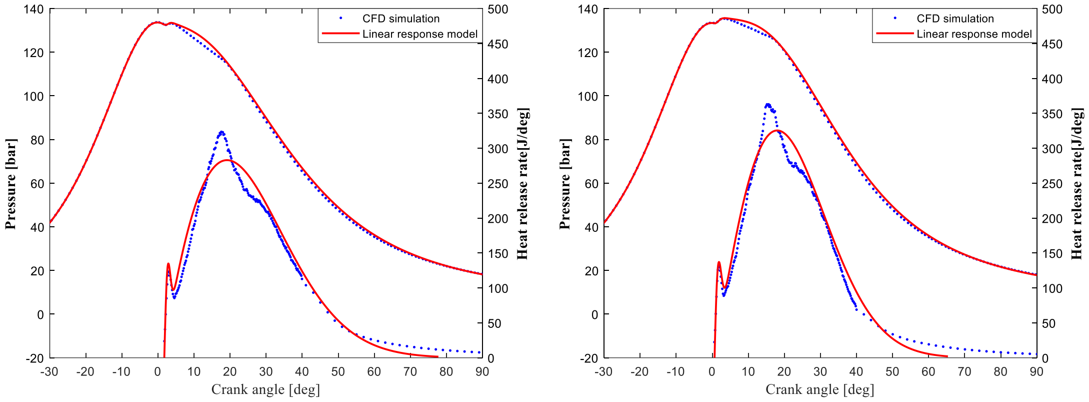

(a) Case 1 at 1800 r/min

(b) Case 2 at 1800 r/min

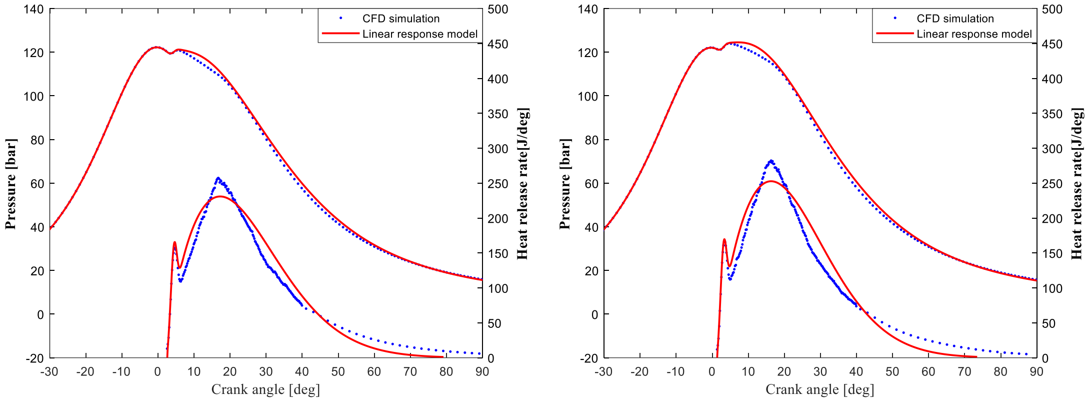

(c) Case 3 at 1629 r/min

(d) Case 4 at 1629 r/min

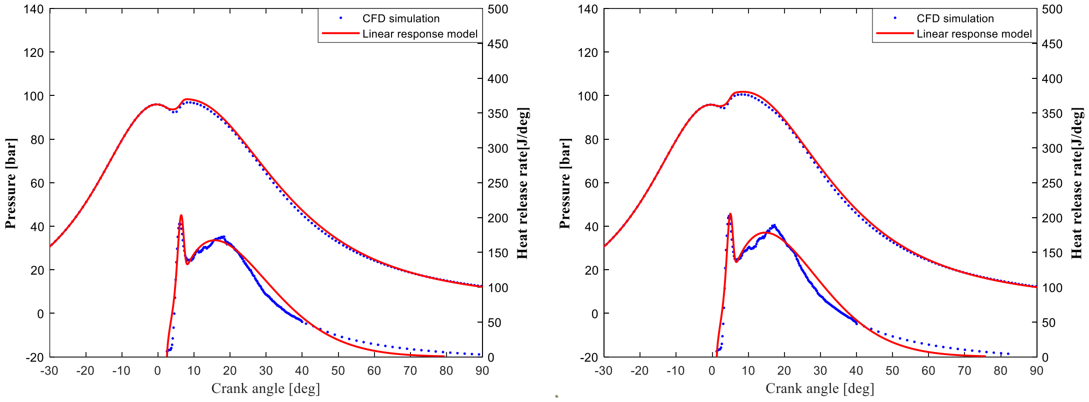

(e) Case 5 at 1457 r/min

(f) Case 6 at 1457 r/min

Figure 6.17 HRR and pressure comparison by using the Linear response model and CFD simulation at three operation conditions: 1800 r/min, 1629 r/min and 1457 r/min

6.4 Engine operating settings optimisation

6.4.1 Case studies analysis

Figure 6.18 presents the derived results (BSFC versus NOx emissions) from the MOGA optimisation for the engine operation at 1800 r/min, 1629 r/min and 1457 r/min. All the failed designs, which correspond to the simulation cases that do not converge, have been excluded from this plot. The points with the blue circle symbols represent the Pareto front, whilst the red square symbols denote the initial points. The simultaneous reduction of the BSFC and NOx emissions can be achieved by identifying Pareto points which are located within the bottom left area surrounded by the baseline BSFC and NOx lines. In this study, the optimal solution (represented by triangular symbol), which is defined as the point that achieves the minimum BSFC value whilst complying with Tier III regulation, can be selected by employing the Pareto front and Tier III NOx emissions limit.

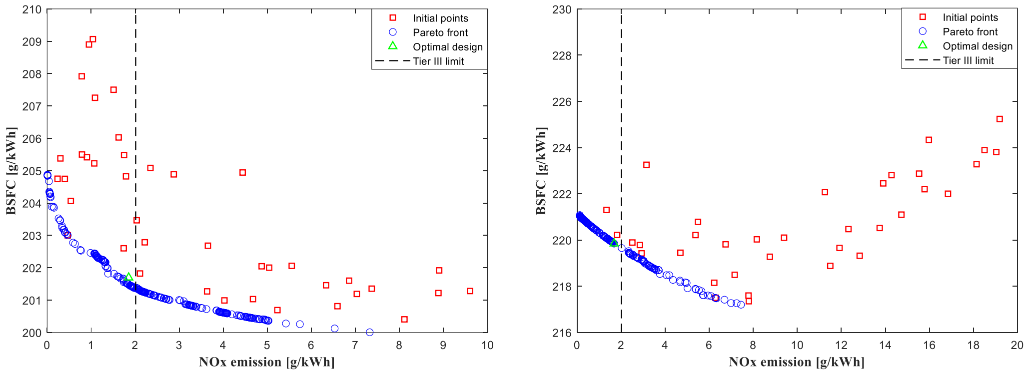

(a) 1800 r/min

(b) 1629 r/min

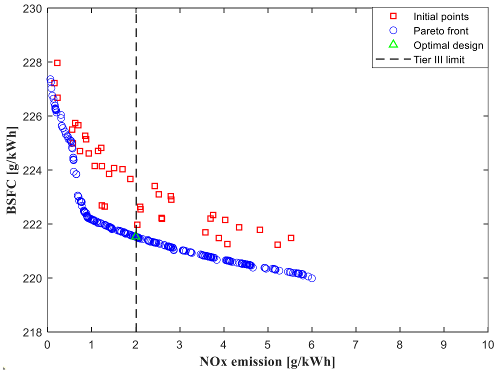

(c) 1457 r/min

Figure 6.18 Optimisation result at three operation conditions: 1800 r/min, 1629 r/min and 1457 r/min

The derived optimal settings of the pilot injection timing, waste gate valve opening and natural gas mass variation at the investigated three operating points are presented in . As deduced from Table 6.14, the pilot injection timing that results in optimal engine performance at all the three operation conditions is –7.0°CA. The waste gate opening demonstrates a low value (8%; where 100% represents a fully open WG valve) at 1629 r/min, which is attributed to the increased natural gas mass. The air mass flow must be increased by reducing the waste gate opening to maintain an appropriate equivalence ratio for efficient combustion. On the other hand, the minimum natural gas mass variation (–5%) is spotted at 1457 r/min, which requires less fresh air for combustion and thus is accompanied by a medium waste gate opening (25%). Figure 6.19 shows the BSFC and NOx emissions comparison between the optimal solution and baseline cases at the three investigated operating points. The BSFC of the optimal solutions at 1457 r/min, 1629 r/min and 1800 r/min are reduced by 4.6%, 7.1% and 6.4% compared to the baseline cases, respectively, whilst the corresponding NOx emissions increased by 23.5%, 14.3% and 16.2 %, respectively. However, the absolute NOx emissions derived from the optimal settings at these three operating points comply with the Tier III NOx emissions limits (2.01 g/(kW·h)).

Table 6.14 Optimisation results summary (case studies 1-3)

Optimisation phase	Case study ID	-	1	2	3
	Rotational speed	r/min	1457	1629	1800
Variable settings	Pilot injection timing	°CA	–7.0	–7.0	–7.0
	Waste gate valve opening	%	25.0	8.0	31.0
	Natural gas mass variation	%	–5.0	5.0	2.0
Output parameters	BSFC	g/(kW·h)	221.5	219.9	201.7
	ΔBSFC	%	–4.6	–7.1	–6.4
	NOx emission	g/(kW·h)	2.00	1.68	1.94
	ΔNOx	%	23.5	14.3	16.2

It’s worth mentioning that the knocking occurrence is not considered in the engine setting optimisation in spite that knocking phenomenon plays an import role in limiting DF engine operation and is investigated in the 3D parametric run. The main reason is that the commonly-used 0D knocking prediction models (like Worret’s knocking criterion [155] or Douaud-Eyzat’s correlation [156]) must be calibrated by using a set of reference parameters for a known cycle at the knocking boundary. It’s not suggested to conduct pertinent testing that might cause severe damage to the engine structure. Thus, as presented in one of the author’s published papers [99], the knocking prediction model of the investigated DF engine was calibrated by virtually running the engine model at knocking boundary which was assumed at 5°CA ahead from the baseline pilot injection timing. On the other hand, the NOx emission prediction model in this thesis can be calibrated by using the measured data, which grants the NOx emission prediction model sufficient accuracy in the optimisation study. That is why the BSFC/NOx emissions trade-off is investigated whilst the virtually running knocking prediction is not included in the optimisation. Nevertheless, as the knocking cases have been excluded when determining the engine settings variation ranges of 3D parametric run, the engine operates with the derived optimal settings is not likely to knock. In the future study, the knocking occurrence could be included as optimisation constrain if experiment data is available for calibrating the 0D knocking prediction model.

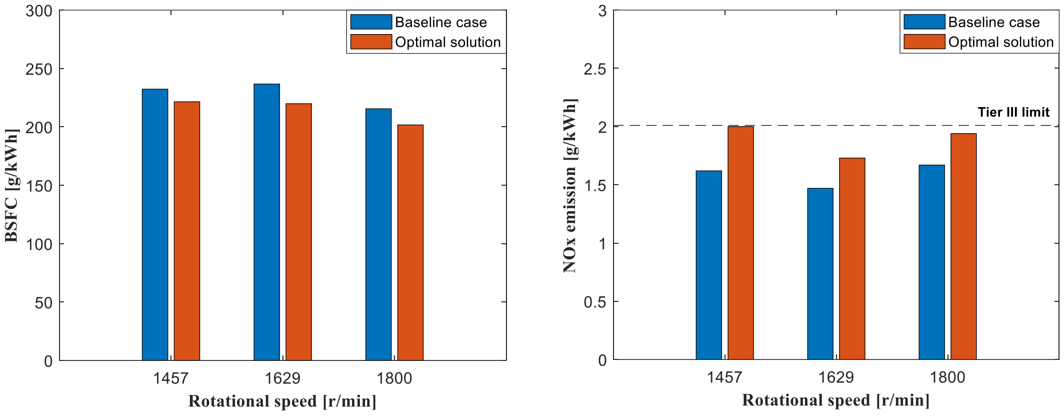

(a) BSFC (b) NOx emissions

Figure 6.19 BSFC and NOx emissions comparison between the optimal solution and baseline cases

6.4.2 Sensitivity study

Apart from identifying the optimal solutions of the engine operating settings, it is also significant to study on the relationship between the input variables (pilot injection timing, waste gate opening and natural gas mass) and the output parameters (BSFC and NOx emissions). A sensitivity analysis (SA), which is defined as a method to measure the impact of input variables uncertainties on the output parameters, is employed to reveal the interactions between the considered engine settings and quantifying their impact on the engine performance parameters. The sensitivity analysis results were obtained by using the GT-ISE tool and represented by the main effect value, which is defined as the difference between the maximum and the minimum response over the full range of the corresponding parameter, whilst keeping other parameters at their baseline value. A negative main effect value means that the response decreases with the increasing parameter values.

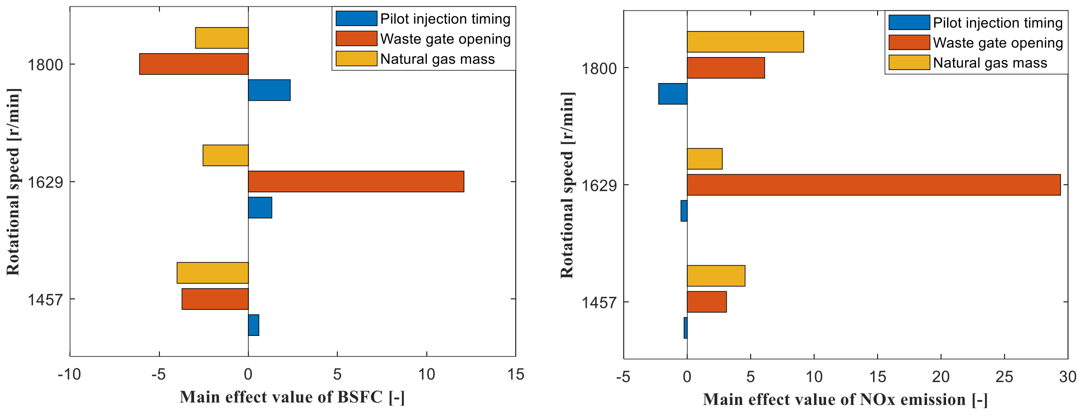

(a) Main effect value of BSFC

(b) Main effect value of NOx emission

Figure 6.20 Sensitivity analysis at three operation conditions: 1800 r/min, 1629 r/min and 1457 r/min

Figure 6.20 shows the sensitivity analysis results (represented by main effect value) at 1800 r/min, 1629 r/min and 1457 r/min operation conditions. As inferred from Figure 6.20(a), the BSFC at high loads (1800 r/min and 1629 r/min) is mainly affected by the waste gate opening, whereas for the medium load (1457 r/min) the effect of waste gate opening is not dominant but almost equivalent to the effect of the natural gas mass, which is the most significant factor. The former is attributed to the direct impact of the waste gate opening on the equivalence ratio, which determines the combustion phase and the heat release rate, thus significantly affecting the BSFC. For 1457 r/min operation condition, the intake fresh air is sufficient due to the reduction of the injected fuel, thus the waste gate opening does not play a primary role. Figure 6.20(b) indicates that the most influencing input for the NOx emissions at 1800 r/min and 1457 r/min is the natural gas mass, whilst the waste gate opening plays the most important role in predicted NOx emissions at 1629 r/min. Nevertheless, the waste gate opening still contributes as the second most important factor for the NOx emissions prediction at 1800 r/min and 1457 r/min.

The individual effect of pilot injection timing or natural gas mass on the BSFC/NOx emissions is similar at the three investigated loads: the BSFC decreases with advanced pilot injection timing or increased natural gas mass, whilst the NOx emissions exhibit a contrary trend with the BSFC. It is inferred that advancing the pilot injection timing or increasing the natural gas mass improves the combustion efficiency, thus reducing the BSFC. On the contrary, larger waste gate opening results in lower BSFC and higher NOx emissions at 1800 r/min and 1457 r/min, whilst for the 1629 r/min, both BSFC and NOx increase with the larger waste gate opening.

6.5 Chapter summary

In this chapter, results of three proposed case studies are presented and discussed. Heat release rates obtained from the 3D parametric runs are used for the Wiebe combustion model calibration, which is subsequently applied to the 0D/1D simulation model for conducting engine settings optimisation. The derived optimal solutions prove to be effective in reducing BSFC whilst complying with Tier III NOx emissions limits.

Chapter 7. Conclusions and recommendations

7.1 Chapter outline

In this chapter, the main findings and conclusions are presented firstly, which are followed by innovation and contributions. Subsequently, the limitations of the developed framework and future research recommendations are discussed. Finally, the aim and objectives of this study are reviewed.

7.2 Main findings and conclusions

The main findings and conclusions of the present study can be summarised with respect to the model development and validation, parametric investigation using 3D simulation model, Wiebe combustion model calibration and engine settings optimisation.

With respect to the model development and validation:

- With the calibrated combustion model by using the HRR calculated from in-cylinder pressure, the developed 0D/1D simulation model can provide an accurate prediction of the engine performance and NOx emission.
- The developed 3D simulation model is capable of predicting the heat release rate, engine performance and emissions (NOx, CO and HC) with adequate accuracy.

With respect to the parametric investigation using the 3D model:

- As inferred from individual effects investigation at 100% load, retarding the pilot injection timing or increasing equivalence ratio leads to increased BSFC and reduced NOx emissions, whereas increasing the injected natural gas mass could result in simultaneous reduction of BSFC and NOx emissions.
- As inferred from individual effects investigation at 100% load, the knock index and the maximum peak pressure decrease simultaneously with retarding the pilot injection timing, reducing the equivalence ratio or reducing the natural gas mass. The advance of the pilot injection timing turns out to be a key factor for stimulating the knocking phenomenon.

- As inferred from the individual effects investigation at 100% load, retarding the pilot injection timing, increasing the equivalence ratio and the natural gas mass result in shorter ignition delay. Once combustion starts, faster flame propagation speed is caused with advanced pilot injection timing and smaller equivalence ratio, whereas natural gas mass variation does not make visible difference on the combustion rate.

- As inferred from the parametric runs, the optimal solution at 1800 r/min and 1629 r/min operation conditions can be achieved by controlling the pilot injection timing, equivalence ratio variation and NG mass variation within –5 to –7.5 °CA, –5% to +5% and 0% to +20%, respectively. For the 1457 r/min operation condition, the appropriate ranges of pilot injection timing and the equivalence ratio variation are the same with those at 1800 r/min and 1629 r/min, whilst the NG mass variation range should be between –10% and +10%.

- As inferred from the parametric runs, the retarded pilot injection timing, smaller equivalence ratio result in later CA50 crank angle and longer combustion duration, indicating a postponed combustion phase. The effect of natural gas mass on combustion phase is negligible.

- The parametric runs by using 3D simulation model provides the HRR data for Wiebe combustion calibration and shows the potential for BSFC and NOx emissions reduction.

With respect to the Wiebe combustion model calibration:

- Considering the prediction of in-cylinder pressure and IMEP, Double Wiebe functions are sufficient for characterising the heat release rate of the investigated DF engine.

- By comparing the predicted HRR and in-cylinder pressure to CFD simulation results, the linear response model was proved to be with adequate accuracy in calibrating the Wiebe combustion model of the investigated DF engine.

- Pilot injection timing has a significant effect on SOC, m_2, $\Delta\varphi_1$ and $\Delta\varphi_2$ while the rest two Wiebe combustion parameters b_2 and m_1 are primarily affected by the NG mass at 1800 r/min. At 1629 r/min, the pilot injection timing is still effective on SOC and $\Delta\varphi_2$ whilst the rest Wiebe parameters are significantly influenced by the NG mass. At 1457 r/min operation condition, b_2 and m_2 are mainly determined by equivalence ratio while m_1, $\Delta\varphi_1$ and $\Delta\varphi_2$ are dominated by NG mass. The determining factor of the SOC at 1457 r/min is the same with that at the other two operation loads, namely the pilot injection timing.

With respect to the engine settings optimisation:

- Compared to the baseline cases, the optimal solutions at 1457 r/min, 1629 r/min and 1800 r/min reduce the BSFC by 4.6%, 7.1% and 6.4%, respectively. The corresponding NOx emissions increase by 23.5%, 14.3% and 16.2%, respectively, whereas the absolute NOx emissions comply with the Tier III NOx emission requirement (2.01 g/(kW·h)) at all three operation loads.
- The BSFC prediction at high loads (1800 r/min and 1629 r/min) is mainly affected by waste gate opening, whereas for operation at medium load (1457 r/min) the effect of waste gate opening is not dominant but almost equal to the effect of natural gas mass, which is the most significant factor.
- The most influencing input of NOx emissions at 1800 r/min and 1457 r/min is natural gas mass, whilst the waste gate opening plays the most important role in predicted NOx emissions at 1629 r/min.

7.3 Innovation

The innovation of the present study is provided as follows.

- A critical review of dual fuel engines combustion modelling based on Wiebe combustion model and the calibration methods of Wiebe combustion parameters. (Section 2.3)
- A novel combustion characterisation method for dual fuel engines – employing experiment-calibrated 3D model to produce ‘virtual’ experimental HRR for calibrating 0D Wiebe combustion model under an extended operation range. (Section 3.2)
- A systematic method for Wiebe combustion model calibration, including heat release calculation from in-cylinder pressure, Wiebe parameters determining and response model development. (Section 3.5)

- A comprehensive study on both in-cylinder combustion (flame propagation, emission generation, knocking detection) and engine performance (pressure, BSFC) of dual fuel engines. (Section 4.3.1 and Section 6.2)
- Wiebe combustion parameters correlations of engine operating settings (pilot injection timing, equivalence ratio and natural gas mass) for four-stroke dual fuel engines; (Section 4.3.2 and Section 6.3)

7.4 Contribution

The academic contribution of the present research is discussed as follows.

- A novel combustion characterisation method which primarily employs a 3D simulation model for calibrating 0D Wiebe combustion model thus relies less on experiment data. It provides a time-saving and cost-effective method for engines modelling and optimization, especially when experiment data is not sufficient.
- The 3D parametric investigation provides a deep and comprehensive understanding of combustion process, emission generation and knocking occurrence inside DF engine cylinders. It can be used as verification of DF engine performance and emissions.
- This work fills the gap of Wiebe combustion parameter correlations of DF engines, whose characteristics differ greatly from conventional diesel and gasoline engines due to the coupling combustion of pilot diesel and natural gas. It offers ideas on how to calibrate Wiebe combustion model of DF engines from measured in-cylinder pressure or 3D simulation HRR.
- This work presents a combined use of engine experiment, 3D simulation model and 0D/1D simulation model. It may inspire even more flexible and effective use of experiment and simulation tools.

The implications to industry are illustrated as follows.

- The proposed research framework can be used by engine manufacturers for shortening design period and reducing experiment cost of DF engine development, thus improving the ship industry sustainability.

- The engine settings optimisation results presented in this work provide guidelines of DF engine management for reducing operating cost and environmental footprint.

7.5 Limitations and future research recommendations

The research limitations are explained as follows.

- When developing the 3D simulation model, methane (CH_4) is used in replacement of detailed natural gas components (CH_4, C_2H_6, C_3H_8, etc.) in order to reduce the computation complexity. Considering the volumetric fraction of methane is 86.37%, this limitation may cause inherent error to the prediction accuracy of engine performance and emissions.
- A double-Wiebe function and a linear response model were selected for calibrating Wiebe combustion model because of the high accuracy in predicting in-cylinder pressure and IMEP (relative errors less than 3%). Nevertheless, the prediction accuracy of the calibrated Wiebe combustion model is not acceptable if HRR is the research objective considering the maximum relative error of peak HRR is as high as 10%.
- The knocking occurrence is not included as constrain in the engine setting optimisation in spite that knocking phenomenon plays an import role in limiting the DF engine operation. The main reason is that a two-zone 0D combustion model is not capable of predicting knocking occurrence with sufficient accuracy.
- Another influencing emission HC is considered in the 3D simulation model but not included in the final engine setting optimisation. This is because that an accurate prediction of HC emission relies on detailed chemical kinetics and sophisticated geometry modelling of the combustion chamber (especially the crevice volume), which cannot be implemented in a 0D/1D simulation model.

The future research recommendations are listed as follows.

- A multi-zone 0D simulation model coupling with detailed chemical kinetic mechanism which may provide an accurate prediction of HC emission with low computation cost.

- A cost-effective method for predicting the DF engines operation window, i.e. the knocking and misfiring limit.
- Engine settings optimisation aiming at reducing both NOx and HC emissions, while taking account the knocking and misfiring occurrence as optimisation constrains.
- Extend the proposed combustion characterisation method for modelling and optimising multi-fuel engines, such as DF engines operating with hydrogen addition.

7.6 Review of research objectives

As stated in Chapter 1, the aim of this thesis is to investigate the in-cylinder combustion details and to optimise the performance-emissions trade-off of marine dual fuel engines by employing a novel combustion characterising method. The research aim is accomplished by achieving a series of research objectives. In this section, it is discussed how these objectives were covered in this thesis.

Objective 1: To investigate the existing challenges faced by DF engines and determine the research gaps by carrying out critical review, as well as propose a novel research framework for solving the research gaps.

This objective was covered in Chapter 1 and Chapter 2. A brief review was given in Chapter 1 to introduce the DF engine challenges, namely performance-emissions trade-off and combustion instability. The research gaps were determined by critically reviewing the engine optimisation, engine modelling and combustion characterisation methods in Chapter 2. In addition, a novel research framework was proposed for addressing the identified research gaps.

Objective 2: To propose the research approach and introduce modelling methodologies of the employed simulation models.

This objective was addressed in Chapter 3. The research approach includes the development and validation of the simulation models, 3D parametric investigation, Wiebe combustion model calibration and engine settings optimisation with MOGA. Detailed modelling methodologies of the 3D and 0D/1D simulation models, combustion model calibration method and multi-objective optimisation were introduced after the research approach in Chapter 3.

Objective 3: To set up engine experiment for model validation and design the case studies.

This objective was addressed in Chapter 4. Dimensions and characteristics of the selected reference engine were introduced in Chapter 4. An experiment was designed to measure the in-cylinder pressure, performance parameters and emissions under the operation conditions of propeller characteristics curve. Subsequently, the simulation case studies of this thesis were illustrated including the parametric investigation using 3D simulation model, Wiebe combustion model calibration and engine settings optimisation.

Objective 4: To develop the proposed 3D and 0D/1D simulation models and validate the accuracy by using experimental data measured from the investigated DF engine. This objective was addressed in Chapter 5. The proposed 3D and 0D/1D simulation models were developed based on the modelling methodologies and the engine characteristics. Then, the prediction accuracy of the proposed 0D/1D model was validated by a quantitative comparison between the simulated and measured in-cylinder pressures as well as performance parameters. On the other hand, the accuracy of the proposed 3D simulation model was verified by using the in-cylinder pressure, heat release rate and emissions obtained from the experiment.

Objective 5: To explore the detailed combustion and emissions characteristics of DF engines under different operating loads by using the developed 3D simulation model. This objective was addressed in Chapter 6. Results of the 3D parametric investigation were discussed in Section 6.2. The validated 3D simulation model was used to investigate the individual effect of the selected operating settings on the engine performance, emissions and knocking occurrence at 100% operation load. Furthermore, a parametric run was performed to obtain the heat release rate and explore the potential engine settings that could provide a simultaneous reduction of the specific fuel consumption and NOx emissions at different operation conditions (1800 r/min, 1629 r/min and 1457 r/min).

Objective 6: To propose a novel combustion characterisation method for DF engines

This objective was addressed in Chapter 6. The results of the Wiebe parameters determining and fitting were discussed in Section 6.3. A comparison between the double and triple Wiebe functions was conducted considering the prediction accuracy of heat release rate and in-cylinder pressure. The double Wiebe function was then selected and employed to obtain the Wiebe parameters of all the simulation cases at 1800 r/min, 1629 r/min and 1457 r/min operation conditions. Subsequently, the Response Surface Methodology (RSM) was used to correlate the selected engine operating settings to the Wiebe combustion parameters. In addition, the in-cylinder pressure simulated by using linear response model and quadratic response model will be compared aiming at a compromise between the model complexity and prediction accuracy.

Objective 7: To optimise the performance-emissions trade-off of DF engines by using multi-objective genetic algorithm.

This objective was addressed in Chapter 6. Results of the engine settings optimisation were discussed in Section 6.4. The calibrated 0D/1D simulation model was jointly used with NSGA II algorithm to perform the engine settings optimisation. The optimal solutions prove to be capable of improving engine performance whilst complying with Tier III NOx limits at three engine loads. In addition, the sensitivity of variables on the responses were analysed.

Objective 8: To summary the main findings, conclusions and contribution of this study and to propose the future research directions.

This objective was addressed in Chapter 7. The main findings and conclusions derived from the results and discussions were summarised. The contribution was discussed in terms of the academic and industrial aspects. Finally, the future research directions were proposed based on the reflections of the thesis limitations.

7.7 Chapter summary

In this chapter, the main findings and conclusions are summarised with regard to model development and validation, 3D parametric investigation, Wiebe combustion model calibration and engine settings optimisation. The innovation is analysed in terms of the critical review, developed framework and proposed methods, which are followed by the academic contribution and industry implications. The research limitations are discussed, providing directions for future research. A review is conducted to check how effectively the proposed research objective have been covered in this work.

References

1. Gössling, S., C. Meyer-Habighorst, and A. Humpe, *A global review of marine air pollution policies, their scope and effectiveness.* Ocean & Coastal Management, 2021. **212**: p. 105824.
2. Čampara, L., N. Hasanspahić, and S. Vujičić. *Overview of MARPOL ANNEX VI regulations for prevention of air pollution from marine diesel engines*. in *SHS web of conferences*. 2018. EDP Sciences.
3. IMO. *Prevention of Air Pollution from Ships*. 2019; Available from: https://www.imo.org/en/OurWork/Environment/Pages/Air-Pollution.aspx.
4. Polakis, M., P. Zachariadis, and J.O. de Kat, *The energy efficiency design index (EEDI)*, in *Sustainable Shipping*. 2019, Springer. p. 93-135.
5. Joung, T.-H., et al., *The IMO initial strategy for reducing Greenhouse Gas (GHG) emissions, and its follow-up actions towards 2050.* Journal of International Maritime Safety, Environmental Affairs, and Shipping, 2020. **4**(1): p. 1-7.
6. Kumar, N.R., C. Sekhar, and S. Adinarayana, *Effects of compression ratio and EGR on performance, combustion and emissions of DI injection diesel engine.* International Journal of Applied Science and Engineering, 2013. **11**(1): p. 41-49.
7. Asad, U., et al., *Fuel injection strategies to improve emissions and efficiency of high compression ratio diesel engines.* SAE International Journal of Engines, 2009. **1**(1): p. 1220-1233.
8. De Ojeda, W., *Effect of variable valve timing on diesel combustion characteristics*. 2010, SAE Technical Paper.
9. Jain, A., A.P. Singh, and A.K. Agarwal, *Effect of split fuel injection and EGR on NOx and PM emission reduction in a low temperature combustion (LTC) mode diesel engine.* Energy, 2017. **122**: p. 249-264.
10. Kang, W., et al., *PM and NOx reduction characteristics of LNT/DPF+ SCR/DPF hybrid system.* Energy, 2018. **143**: p. 439-447.
11. Maiboom, A. and X. Tauzia, *NOx and PM emissions reduction on an automotive HSDI Diesel engine with water-in-diesel emulsion and EGR: An experimental study.* Fuel, 2011. **90**(11): p. 3179-3192.
12. Deng, J., et al., *A review of NOx and SOx emission reduction technologies for marine diesel engines and the potential evaluation of liquefied natural gas fuelled vessels.* Science of The Total Environment, 2020: p. 144319.
13. Vasilescu, M.-V., et al. *Research on Exhaust Gas Cleaning System (EGCS) used in shipping industry for reducing SOx emissions*. in *E3S Web of Conferences*. 2021. EDP Sciences.
14. Jang, H., et al., *Development of Parametric Trend Life Cycle Assessment for marine SOx reduction scrubber systems.* Journal of Cleaner Production, 2020. **272**: p. 122821.
15. Lepitzki, J. and J. Axsen, *The role of a low carbon fuel standard in achieving long-term GHG reduction targets.* Energy Policy, 2018. **119**: p. 423-440.
16. Baldissone, G., M. Demichela, and D. Fissore, *Lean VOC-air mixtures catalytic treatment: Cost-benefit analysis of competing technologies.* Environments, 2017. **4**(3): p. 46.
17. TOKUŞLU, A., *Analyzing the Energy Efficiency Design Index (EEDI) performance of a container ship.* International Journal of Environment and Geoinformatics, 2020. **7**(2): p. 114-119.
18. Thomson, H., J.J. Corbett, and J.J. Winebrake, *Natural gas as a marine fuel.* Energy Policy, 2015.

87(December): p. 153-167.

19. Zhen, X., et al., *The engine knock analysis–an overview.* Applied Energy, 2012. **92**: p. 628-636.
20. Chen, H., J. He, and X. Zhong, *Engine combustion and emission fuelled with natural gas: a review.* Journal of the Energy Institute, 2019. **92**(4): p. 1123-1136.
21. Doug, W., *Gas-diesel and dual-fuel engines*, in *Pounder's Marine Diesel Engines (Eighth Edition)*, D. Woodyard, Editor. 2004, Butterworth-Heinemann: Oxford. p. 48-63.
22. Shamekhi, A., N. Khatibzadeh, and A.H. Shamekhi. *Performance and emissions characteristics investigation of a bi-fuel SI engine fuelled by CNG and gasoline*. in *ASME 2006 Internal Combustion Engine Division Spring Technical Conference*. 2006. American Society of Mechanical Engineers.
23. Yang, L.-P., et al., *Analysis of the dynamic characteristics of combustion instabilities in a pre-mixed lean-burn natural gas engine.* Applied Energy, 2016. **183**: p. 746-759.
24. Cordiner, S., et al., *Numerical and Experimental Analysis of Combustion and Exhaust Emissions in a Dual-Fuel Diesel/Natural Gas Engine.* Energy & Fuels, 2008. **22**(3): p. 1418-1424.
25. Korakianitis, T., A.M. Namasivayam, and R.J. Crookes, *Natural-gas fueled spark-ignition (SI) and compression-ignition (CI) engine performance and emissions.* Progress in energy and combustion science, 2011. **37**(1): p. 89-112.
26. Huang, J. and R.J. Crookes, *Assessment of simulated biogas as a fuel for the spark ignition engine.* Fuel, 1998. **77**(15): p. 1793-1801.
27. Cho, H.M. and B.-Q. He, *Spark ignition natural gas engines—A review.* Energy conversion and management, 2007. **48**(2): p. 608-618.
28. Evans, R.L. and J. Blaszczyk, *A comparative study of the performance and exhaust emissions of a spark ignition engine fuelled by natural gas and gasoline.* Proceedings of the Institution of Mechanical Engineers Part D Journal of Automobile Engineering, 2005. **211**(211): p. 39-47.
29. Chen, G.T., *Research on Supercharging Performance of 190 Series 6-Cylinder Gas Engine.* Applied Mechanics & Materials, 2014. **543-547**: p. 282-285.
30. Kesgin, U., *Effect of turbocharging system on the performance of a natural gas engine.* Energy Conversion & Management, 2005. **46**(1): p. 11-32.
31. Zeng, K., et al., *Combustion characteristics of a direct-injection natural gas engine under various fuel injection timings.* Applied thermal engineering, 2006. **26**(8-9): p. 806-813.
32. Kahraman, N., et al., *Investigation of combustion characteristics and emissions in a spark-ignition engine fuelled with natural gas–hydrogen blends.* International Journal of Hydrogen Energy, 2009. **34**(2): p. 1026-1034.
33. Bhandari, K., et al., *Performance and emissions of natural gas fueled internal combustion engine: A review.* 2005.
34. Crookes, R.J., T. Korakianitis, and A.M. Namasivayam. *A systematic experimental assessment of the use of rapeseed methyl ester (RME) as a compression ignition engine fuel during conventional and dual-fuel operation*. in *TAE 7th International Colloquium on Fuels. Stuttgart*. 2009.
35. Papagiannakis, R., et al., *Theoretical study of the effects of engine parameters on performance and emissions of a pilot ignited natural gas diesel engine.* Energy, 2010. **35**(2): p. 1129-1138.
36. Li, W., Z. Liu, and Z. Wang, *Experimental and theoretical analysis of the combustion process at low loads of a diesel natural gas dual-fuel engine.* Energy, 2016. **94**: p. 728-741.
37. Zhang, D., *8 - Direct injection natural gas engines*, in *Advanced Direct Injection Combustion Engine Technologies and Development*, H. Zhao, Editor. 2010, Woodhead Publishing. p. 199-228.

38. Park, S. and S. Song, *Model-based multi-objective Pareto optimization of the BSFC and NOx emission of a dual-fuel engine using a variable valve strategy.* Journal of Natural Gas Science and Engineering, 2017. **39**: p. 161-172.
39. Mustafi, N.N., R.R. Raine, and S. Verhelst, *Combustion and emissions characteristics of a dual fuel engine operated on alternative gaseous fuels.* Fuel, 2013. **109**: p. 669-678.
40. Lounici, M.S., et al., *Towards improvement of natural gas-diesel dual fuel mode: An experimental investigation on performance and exhaust emissions.* Energy, 2014. **64**: p. 200-211.
41. Liu, J., et al., *Effects of pilot fuel quantity on the emissions characteristics of a CNG/diesel dual fuel engine with optimized pilot injection timing.* Applied Energy, 2013. **110**: p. 201-206.
42. Weaver, C.S. and S.H. Turner, *Dual fuel natural gas/diesel engines: technology, performance, and emissions*. 1994, SAE Technical Paper.
43. Sahoo, B., N. Sahoo, and U. Saha, *Effect of engine parameters and type of gaseous fuel on the performance of dual-fuel gas diesel engines—A critical review.* Renewable and Sustainable Energy Reviews, 2009. **13**(6-7): p. 1151-1184.
44. Gharehghani, A., et al., *A computational study of operating range extension in a natural gas SI engine with the use of hydrogen.* International Journal of Hydrogen Energy, 2015. **40**(17): p. 5966-5975.
45. Das, A. and H.C. Watson, *Development of a natural gas spark ignition engine for optimum performance.* Proceedings of the Institution of Mechanical Engineers Part D Journal of Automobile Engineering, 1997. **211**(211): p. 361-378.
46. Chen, S.K. and N.J. Beck. *Gas Engine Combustion Principles and Applications*. *Future Transportation Technology Conference & Exposition*. 2001.
47. Heywood, J.B., *Internal combustion engine fundamentals*. Vol. 9. 1988: Mcgraw-hill New York. 457.
48. Yao, C., A. Yao, and H. Xu, *Mechanism of internal combustion engine detonation and its damage to combustion chamber components*. 2015: Science Press.
49. Wang, Z., H. Liu, and R.D. Reitz, *Knocking combustion in spark-ignition engines.* 2017. **61**: p. 78-112.
50. Ibrahim, A. and S. Bari, *Optimization of a natural gas SI engine employing EGR strategy using a two-zone combustion model.* Fuel, 2008. **87**(10-11): p. 1824-1834.
51. Taghavifar, H., S. Khalilarya, and S. Jafarmadar, *Engine structure modifications effect on the flow behavior, combustion, and performance characteristics of DI diesel engine.* Energy conversion and management, 2014. **85**: p. 20-32.
52. Tanner, F.X. and S. Srinivasan, *Optimization of fuel injection configurations for the reduction of emissions and fuel consumption in a diesel engine using a conjugate gradient method*. 2005, SAE Technical Paper.
53. Tanner, F.X. and S. Srinivasan, *CFD-based optimization of fuel injection strategies in a diesel engine using an adaptive gradient method.* Applied Mathematical Modelling, 2009. **33**(3): p. 1366-1385.
54. Wang, J., et al., *Power recovery of a variable nozzle turbocharged diesel engine at high altitude by response surface methodology and sequential quadratic programming.* Proceedings of the Institution of Mechanical Engineers, Part D: Journal of Automobile Engineering, 2019. **233**(4): p. 810-823.
55. Hiroyasu, T. *Diesel engine design using multi-objective genetic algorithm*. in *Japan/US Workshop*

on Design Environment 2004. 2004. Citeseer.

56. Lotfan, S., et al., *ANN-based modeling and reducing dual-fuel engine's challenging emissions by multi-objective evolutionary algorithm NSGA-II.* Applied energy, 2016. **175**: p. 91-99.
57. Jeong, S., S. Obayashi, and Y. Minemura, *Application of hybrid evolutionary algorithms to low exhaust emission diesel engine design.* Engineering Optimization, 2008. **40**(1): p. 1-16.
58. Zhang, Q., R.M. Ogren, and S.-C. Kong, *A comparative study of biodiesel engine performance optimization using enhanced hybrid PSO–GA and basic GA.* Applied energy, 2016. **165**: p. 676-684.
59. Mohammadhassani, J., et al., *Prediction and reduction of diesel engine emissions using a combined ANN–ACO method.* Applied Soft Computing, 2015. **34**: p. 139-150.
60. Bertram, A.M., Q. Zhang, and S.-C. Kong, *A novel particle swarm and genetic algorithm hybrid method for diesel engine performance optimization.* International Journal of Engine Research, 2016. **17**(7): p. 732-747.
61. Gao, Y., et al., *Part III: Optimization, Intelligent Optimization Algorithms*, in *Computer modeling for injection molding: Simulation, Optimization, and Control*, H. Zhou, Editor. 2013, Wiley. p. 283-292.
62. Tao, F., Y. Laili, and L. Zhang, *Brief history and overview of intelligent optimization algorithms*, in *Configurable Intelligent Optimization Algorithm*. 2015, Springer. p. 3-33.
63. Sampson, J.R., *Adaptation in natural and artificial systems (John H. Holland)*. 1976, Society for Industrial and Applied Mathematics.
64. Millo, F., P. Arya, and F. Mallamo, *Optimization of automotive diesel engine calibration using genetic algorithm techniques.* Energy, 2018. **158**: p. 807-819.
65. Kim, M., M.P. Liechty, and R.D. Reitz, *Application of micro-genetic algorithms for the optimization of injection strategies in a heavy-duty diesel engine*. 2005, SAE Technical Paper.
66. Jaliliantabar, F., et al., *Multi-objective NSGA-II optimization of a compression ignition engine parameters using biodiesel fuel and exhaust gas recirculation.* Energy, 2019. **187**: p. 115970.
67. Stoumpos, S. and G. Theotokatos, *Multiobjective optimisation of a marine dual fuel engine equipped with exhaust gas recirculation and air bypass systems.* Energies, 2020. **13**(19): p. 5021.
68. Mendoza, F., J.L. Bernal-Agustin, and J.A. Domínguez-Navarro, *NSGA and SPEA applied to multiobjective design of power distribution systems.* IEEE Transactions on power systems, 2006. **21**(4): p. 1938-1945.
69. Deb, K., et al., *A fast and elitist multiobjective genetic algorithm: NSGA-II.* IEEE transactions on evolutionary computation, 2002. **6**(2): p. 182-197.
70. Vesikar, Y., K. Deb, and J. Blank. *Reference point-based NSGA-III for preferred solutions*. in *2018 IEEE symposium series on computational intelligence (SSCI)*. 2018. IEEE.
71. Ishibuchi, H., et al. *Performance comparison of NSGA-II and NSGA-III on various many-objective test problems*. in *2016 IEEE Congress on Evolutionary Computation (CEC)*. 2016. IEEE.
72. Myers, R.H., D.C. Montgomery, and C.M. Anderson-Cook, *Response surface methodology: process and product optimization using designed experiments*. 2016: John Wiley & Sons.
73. Bertram, A.M. and S.-C. Kong, *Computational optimization of a diesel engine calibration using a novel SVM-PSO method.* 2019, SAE Technical Paper.
74. d'Ambrosio, S. and A. Ferrari, *Potential of double pilot injection strategies optimized with the design of experiments procedure to improve diesel engine emissions and performance.* Applied energy, 2015. **155**: p. 918-932.

75. Ge, H.-W., et al., *Engine development using multi-dimensional CFD and computer optimization*. 2010, SAE Technical Paper.
76. Baldi, F., G. Theotokatos, and K. Andersson, *Development of a combined mean value–zero dimensional model and application for a large marine four-stroke Diesel engine simulation.* Applied Energy, 2015. **154**: p. 402-415.
77. Ding, Y., D. Stapersma, and H. Grimmelius, *Using parametrized finite combustion stage models to characterize combustion in diesel engines.* Energy & Fuels, 2012. **26**(12): p. 7099-7106.
78. Demir, U., et al., *Evaluation of zero dimensional codes in simulating IC engines using primary reference fuel.* Applied Thermal Engineering, 2015. **76**: p. 18-24.
79. Rothe, M., et al., *Knock behavior of SI-engines: Thermodynamic analysis of knock onset locations and knock intensities*. 2006, SAE Technical Paper.
80. Kawahara, N. and E. Tomita, *Visualization of auto-ignition and pressure wave during knocking in a hydrogen spark-ignition engine.* International Journal of Hydrogen Energy, 2009. **34**(7): p. 3156-3163.
81. Xiang, L., E. Song, and Y. Ding, *A Two-Zone Combustion Model for Knocking Prediction of Marine Natural Gas SI Engines.* Energies, 2018. **11**(3): p. 561.
82. Liu, J. and C.E. Dumitrescu, *Lean-Burn Characteristics of a Heavy-Duty Diesel Engine Retrofitted to Natural-Gas Spark Ignition.* Journal of Engineering for Gas Turbines and Power-Transactions of the Asme, 2019. **141**(7).
83. Kaprielian, L., et al., *Multi-zone quasi-dimensional combustion models for Spark-Ignition engines*. 2013, SAE Technical Paper.
84. Xu, S., et al., *A phenomenological combustion analysis of a dual-fuel natural-gas diesel engine.* Proceedings of the Institution of Mechanical Engineers, Part D: Journal of Automobile Engineering, 2017. **231**(1): p. 66-83.
85. Javaheri, A., et al., *Investigation of Natural Gas Composition Effects on Knock Phenomenon in SI Gas Engines Using Detailed Chemistry.* Applied Mechanics and Materials, 2014. **493**: p. 239-244.
86. Priesching, P., et al., *About Describing the Knocking Combustion in Gasoline and Gas Engines by CFD Methods*. 2015, SAE Technical Paper.
87. Maghbouli, A., et al., *A multi-dimensional CFD-chemical kinetics approach in detection and reduction of knocking combustion in diesel-natural gas dual-fuel engines using local heat release analysis.* SAE International Journal of Engines, 2013. **6**(2013-01-0865): p. 777-787.
88. Abagnale, C., et al., *Combined numerical-experimental study of dual fuel diesel engine.* Energy procedia, 2014. **45**: p. 721-730.
89. Maurya, R.K. and P. Mishra, *Parametric investigation on combustion and emissions characteristics of a dual fuel (natural gas port injection and diesel pilot injection) engine using 0-D SRM and 3D CFD approach.* Fuel, 2017. **210**: p.900-913.
90. Montoya, J.P.G., G.J.A. Diaz, and A.A.A.J.I.J.o.H.E. Arrieta, *Effect of equivalence ratio on knocking tendency in spark ignition engines fueled with fuel blends of biogas, natural gas, propane and hydrogen.* 2018. **43**(51): p. 23041-23049.
91. Noda, T., et al., *Development of transient knock prediction technique by using a zero-dimensional knocking simulation with chemical kinetics*. 2004, SAE Technical Paper.
92. Merker, G.P., et al., *Simulating Combustion: Simulation of combustion and pollutant formation for engine-development*. Vol. 7. 2005: Springer Science & Business Media.

93. Mikulski, M., S. Wierzbicki, and A.J.E.i.N. Piętak, *Zero-dimensional 2-phase combustion model in a dual-fuel compression ignition engine fed with gaseous fuel and a divided diesel fuel charge.* 2015. **17**.

94. Aklouche, F., et al., *Predictive model of the diesel engine operating in dual-fuel mode fuelled with different gaseous fuels.* Fuel, 2018. **220**: p. 599-606.

95. Alla, G.A., et al., *Combustion quasi-two zone predictive model for dual fuel engines.* 2001. **42**(12): p. 1477-1498.

96. Pirouzpanah, V., et al., *Comparison of thermal and radical effects of EGR gases on combustion process in dual fuel engines at part loads.* 2007. **48**(7): p. 1909-1918.

97. Bilcan, A., et al., *Characterization of the LPG-diesel dual fuel combustion*. 2001, SAE Technical Paper.

98. Liu, Z., G.J.P.o.t.I.o.M.E. Karim, Part A: Journal of Power, and Energy, *Simulation of combustion processes in gas-fuelled diesel engines.* 1997. **211**(2): p. 159-169.

99. Xiang, L., et al., *Parametric knocking performance investigation of spark ignition natural gas engines and dual fuel engines.* Journal of Marine Science and Engineering, 2020. **8**(6): p. 459.

100. Miyamoto, N., et al., *Description and analysis of diesel engine rate of combustion and performance using Wiebe's functions.* SAE transactions, 1985: p. 622-633.

101. Witt, H., M. Hassenforder, and G. Gissinger, *Modelling and identification of a diesel combustion process with the downhill gradient search method.* SAE transactions, 1995: p. 1526-1533.

102. Tolou, S., et al., *Combustion model for a homogeneous turbocharged gasoline direct-injection engine.* Journal of engineering for gas turbines and power, 2018. **140**(10).

103. Sun, Y., et al., *Development and validation of a marine sequential turbocharging diesel engine combustion model based on double Wiebe function and partial least squares method.* Energy Conversion and Management, 2017. **151**: p. 481-495.

104. Torregrosa, A.J., et al., *Numerical Estimation of Wiebe Function Parameters Using Artificial Neural Networks in SI Engine*. 2021, SAE Technical Paper.

105. Katrašnik, T., F. Trenc, and S.R. Oprešnik, *A new criterion to determine the start of combustion in diesel engines.* 2006.

106. Liu, Z. and G. Karim, *Simulation of combustion processes in gas-fuelled diesel engines.* Proceedings of the Institution of Mechanical Engineers, Part A: Journal of Power and Energy, 1997. **211**(2): p. 159-169.

107. Stoumpos, S., et al., *Towards Marine Dual Fuel Engines Digital Twins—Integrated Modelling of Thermodynamic Processes and Control System Functions.* Journal of Marine Science and Engineering, 2020. **8**(3): p. 200.

108. Karim, G.A., W. Jones, and R.R. Raine, *An examination of the ignition delay period in dual fuel engines*. 1989, SAE Technical Paper.

109. Ferguson, C.R. and A.T. Kirkpatrick, *Internal combustion engines: applied thermo sciences*. 2015: John Wiley & Sons.

110. Mustafi, N.N., R.R. Raine, and S. Verhelst, *Combustion and emissions characteristics of a dual fuel engine operated on alternative gaseous fuels. Fuel.* 2013. **109**: p. 669-678.

111. Raine, R.R., *A performance model of the dual fuel (diesel/natural gas) engine*. 1990, SAE Technical Paper.

112. Liu, Z. and G.A. Karim, *The ignition delay period in dual fuel engines.* SAE transactions, 1995: p. 354-362.

113. Piętak, A. and M. Mikulski, *On the modeling of pilot dose ignition delay in a dual-fuel, self ignition engine.* Silniki Spalinowe, 2011. **50**.

114. Assanis, D.N., et al., *A predictive ignition delay correlation under steady-state and transient operation of a direct injection diesel engine.* 2003. **125**(2): p. 450-457.

115. Prakash, G., A. Ramesh, and A.B. Shaik, *An approach for estimation of ignition delay in a dual fuel engine.* SAE transactions, 1999: p. 399-405.

116. Hardenberg, H.O. and F.W. Hase, *An empirical formula for computing the pressure rise delay of a fuel from its cetane number and from the relevant parameters of direct-injection diesel engines. SAE Transactions.* 1979: p. 1823-1834.

117. Ghojel, J.I., *Review of the development and applications of the Wiebe function: a tribute to the contribution of Ivan Wiebe to engine research.* International Journal of Engine Research, 2010. **11**(4): p. 297-312.

118. Woschni, G., *A universally applicable equation for the instantaneous heat transfer coefficient in the internal combustion engine*. 1967, SAE Technical paper.

119. Yaws, C.L., *Handbook of Thermodynamic Diagrams, Volume 3*. Vol. 4. 1986, USA: Gulf Publication Company.

120. Borman, G.L. and K.W. Ragland, *Combustion engineering*. 1998: McGraw-Hill Science/Engineering/Math.

121. Chen, S.K. and P.F. Flynn, *Development of a single cylinder compression ignition research engine*. 1965, SAE Technical Paper.

122. Reitz, R.D. and R. Diwakar, *Structure of high-pressure fuel sprays.* SAE transactions, 1987: p. 492-509.

123. Beale, J.C. and R.D. Reitz, *Modeling spray atomization with the Kelvin-Helmholtz/Rayleigh-Taylor hybrid model.* Atomization and sprays, 1999. **9**(6).

124. Amsden, A., *A computer program for chemically reactive flows with sprays.* Report of Los Alamos National Laboratory, 1989.

125. Senecal, P., et al., *Multi-dimensional modeling of direct-injection diesel spray liquid length and flame lift-off length using CFD and parallel detailed chemistry.* SAE transactions, 2003: p. 1331-1351.

126. Rahimi, A., E. Fatehifar, and R.K. Saray, *Development of an optimized chemical kinetic mechanism for homogeneous charge compression ignition combustion of a fuel blend of n-heptane and natural gas using a genetic algorithm.* Proceedings of the Institution of Mechanical Engineers, Part D: Journal of Automobile Engineering, 2010. **224**(9): p. 1141-1159.

127. Han, Z. and R.D. Reitz, *Turbulence modeling of internal combustion engines using RNG κ-ε models.* Combustion science and technology, 1995. **106**(4-6): p. 267-295.

128. CONVERGE. *CONVERGE user conference introduction*. 2021; Available from: https://convergecfd.com/.

129. Reitz, R.D., *Mechanism of breakup of round liquid jets.* Encyclopedia of fluid mechanics, 1986. **10**.

130. Senecal, P., et al., *A new parallel cut-cell Cartesian CFD code for rapid grid generation applied to in-cylinder diesel engine simulations*. 2007, SAE Technical Paper.

131. Senecal, P.K., *Development of a methodology for internal combustion engine design using multi-dimensional modeling with validation through experiments.* 2001.

132. Turns, S.R., *Introduction to combustion*. Vol. 287. 1996: McGraw-Hill Companies.

133. Ding, Y., *Characterising combustion in diesel engines*, in *TU Delft*. 2011.

134. Watson, N., A. Pilley, and M. Marzouk, *A combustion correlation for diesel engine simulation*. 1980, SAE Technical Paper.

135. Deb, M., et al., *Multi objective optimization of performance parameters of a single cylinder diesel engine with hydrogen as a dual fuel using pareto-based genetic algorithm.* International journal of hydrogen energy, 2014. **39**(15): p. 8063-8077.

136. AVL, *Pressure sensor for combustion analysis - GU22CK*. 2016.

137. KISTLER, *Measurement and evaluation system for combustion analysis on test benches and in vegicles - KiBox To Go 2893B*. 2019: Switzerland.

138. AVL. *AVL Fuel Mass Flow Meter and Fuel Temperature Control*. 2019; Available from: https://www.avl.com/-/avl-fuel-mass-flow-meter-and-fuel-temperature-control.

139. Endress+Hauser. *Proline Promass 83F Coriolis flowmeter*. 2019; Available from: https://www.uk.endress.com/en/field-instruments-overview/flow-measurement-product-overview/Product-Coriolis-flowmeter-Proline-Promass-83F.

140. ABB. *Thermal mass flowmeter: Sensyflow FMT700-P and FMT700-P Compact*. 2019; Available from: https://new.abb.com/products/measurement-products/flow/thermal-mass-flowmeters/sensyflow-fmt700-p.

141. AVL, *Pressure sensor for combustion analysis - LP11DA*. 2016.

142. AVL. *AMA i60 exhaust measurement system*. 2013; Available from: https://www.avl.com/-/avl-fuel-mass-flow-meter-and-fuel-temperature-control.

143. Bonalivi, *GS5969 E Natural gas chromatographic analyzer.* 2020

144. PetroChina. 2020; Available from: http://www.petrochina.com.cn/ptr/.

145. Zhu, L., et al., *Effects of fuel reforming on large-bore low-speed two-stroke dual fuel marine engine combined with EGR and injection strategy.* International Journal of Hydrogen Energy, 2020. **45**(53): p. 29505-29517.

146. Ryu, K., *Effects of pilot injection timing on the combustion and emissions characteristics in a diesel engine using biodiesel–CNG dual fuel.* Applied Energy, 2013. **111**: p. 721-730.

147. Zheng, J., et al., *Effect of equivalence ratio on combustion and emissions of a dual-fuel natural gas engine ignited with diesel.* Applied Thermal Engineering, 2019. **146**: p. 738-751.

148. Papagiannakis, R. and D. Hountalas, *Experimental investigation concerning the effect of natural gas percentage on performance and emissions of a DI dual fuel diesel engine.* Applied Thermal Engineering, 2003. **23**(3): p. 353-365.

149. Wang, H., H. Gan, and G. Theotokatos, *Parametric investigation of pre-injection on the combustion, knocking and emissions behaviour of a large marine four-stroke dual-fuel engine.* Fuel, 2020. **281**: p. 118744.

150. Zhou, D., et al., *Application of CFD-chemical kinetics approach in detecting RCCI engine knocking fuelled with biodiesel/methanol.* Applied Energy, 2015. **145**: p. 255-264.

151. Li, A., Z. Zheng, and T. Peng, *Effect of water injection on the knock, combustion, and emissions of a direct injection gasoline engine.* Fuel, 2020. **268**: p. 117376.

152. Liang, L., et al., *Modeling knock in spark-ignition engines using a G-equation combustion model incorporating detailed chemical kinetics*. 2007, SAE Technical Paper.

153. Ding, Y., et al., *A new method to smooth the in-cylinder pressure signal for combustion analysis in diesel engines.* Proceedings of the Institution of MechanicalEngineers-A, 2011. **225**(3): p. 309.

154. Zhang, K., et al., *An updated experimental and kinetic modeling study of n-heptane oxidation.*

Combustion and Flame, 2016. **172**: p. 116-135.

155. Worret, R., et al., *Application of different cylinder pressure based knock detection methods in spark ignition engines.* SAE Transactions, 2002: p. 2244-2257.
156. Douaud, A. and P. Eyzat, *Four-octane-number method for predicting the anti-knock behavior of fuels and engines.* SAE Transactions, 1978: p. 294-308.

APPENDIX

APPENDIX A – Bilcan's schematic algorithm

In order to obtain the three sets of Wiebe parameters (φ_i, $\varDelta\varphi_i$, b_i and m_i), the schematic algorithm proposed by Bilcan [97] is used jointly with the curve fitting method. Specifically, the entire combustion process of dual fuel engines was divided into 3 stages: the premixed combustion of diesel fuel and a small part of the gaseous fuel entrained by the pilot spray; the premixed combustion of primary fuel; the diffusion combustion of the gaseous fuel and the left-over pilot fuel. The key characteristics of each stage are described as follows.

(1) Stage 1

Stage 1 is considered to start at the same crank angle as the entire combustion process. Thus, φ_1 can be determined by the pilot injection timing and estimated ignition delay. In Bilcan's study [97], the end of the first combustion stage is obtained by extrapolating the straight line that links point 2 and point 3 on the HRR curve, as shown in Figure A.1(a). Watson et al. [134] proposed a function of the ignition delay and the equivalence ratio to estimate the premixed fraction b_1 of a direct injection diesel engine, which can be modified for dual-fuel engine according to the experiment data.

$$b_1 = 1 - \frac{a_w \cdot \phi^{b_w}}{\tau^{c_w}} \tag{1}$$

where a_w, b_w and c_w are empirically determined coefficients, which are within the ranges $0.8 < a_w < 0.95$, $0.8 < a_w < 0.95$, $0.8 < a_w < 0.95$ according to Watson et al. [134]; ϕ is the equivalence ratio; τ is the ignition delay.

(2) Stage 2

The premixed combustion of the gaseous fuel is considered to start before the end of the premixed combustion phase of the pilot fuel, as the conditions inside the cylinder are suitable enough to initiate the gaseous fuel ignition. The value of φ_2 could be evaluated between (φ_1, $\varphi_1 + \varDelta\varphi_1$), whilst $\varDelta\varphi_2$ has to be adjusted for each investigated engine. Weigh factor b_2 can be calculated by Equation (2) once b_3 is known.

$$b_1 + b_2 + b_3 = 1 \tag{2}$$

(3) Stage 3

Stage 3 is considered to commence some degrees after the start of the entire combustion process. The value of φ_3 needs to be adjusted to match specific engine. The end of stage 3 is identical with the end of the entire combustion process.

The optimal combination of the uncertain parameters is found by using the least square criterion applied corresponding to the schematic algorithm presented in Figure A.1. Table A.1 presents the significance of the 5 determining points in a HRR curve. The detailed calibration process employs the following steps. The first step determines the b_3 and m_3 for the diffusion phase of the combustion process, as shown in Figure A.1 (a). Then, the rest two HRR phases of stage 1 and stage 2 are obtained by subtracting the simulated HRR of stage 3. m_1 can be found corresponding to the premixed combustion phase in Figure A.1 (b). Finally, after another subtraction (shown in Figure A.1 (c)), $\Delta\varphi_2$ and m_2 are determined for the premixed combustion of gaseous fuel. The optimal parameters set can be obtained by minimising the difference between the simulated HRR and HRR obtained from the measured in-cylinder pressure as presented in Figure A.1 (d).

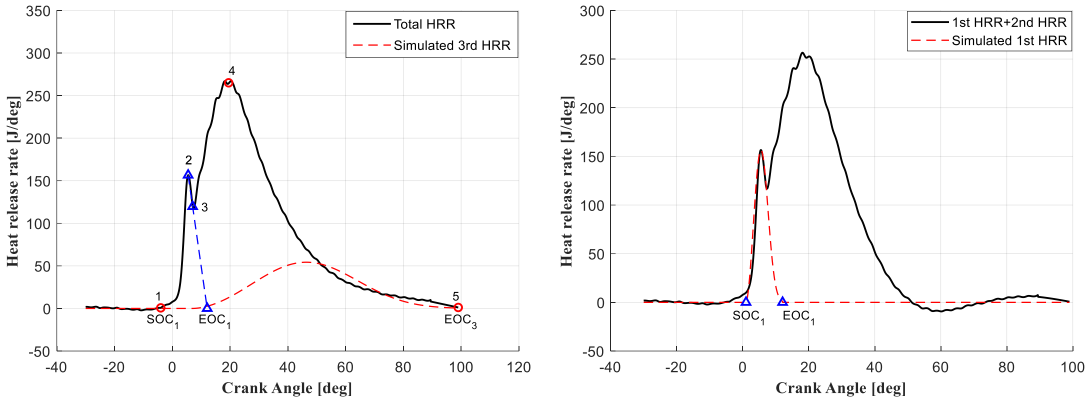

(a) 3th HRR fitting (b) 1st HRR fitting

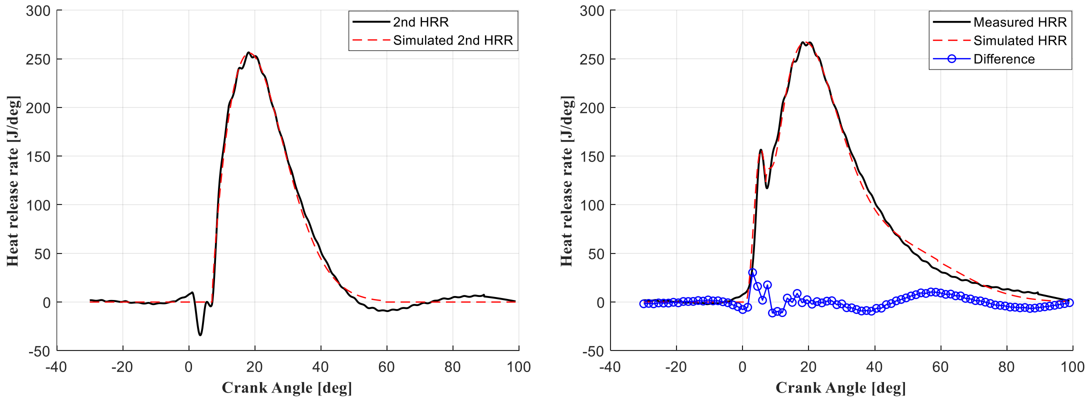

(c) 2nd HRR fitting (d) Minimum the difference

Figure A.1 Schematic algorithm for determining the Wiebe parameters

Table A.1 Five determining points in a HRR curve

1	Start of the combustion process
2	Maximum value of HRR during the first combustion stage
3	Minimal value of HRR between the first and second combustion stage
4	Maximum value of HRR during the second combustion stage
5	End of the combustion process